



universität
wien

MASTERARBEIT / MASTER'S THESIS

Titel der Masterarbeit / Title of the Master's Thesis

„Inclusive Top Quark Pair Production Cross Section at Future Linear Colliders: Matching Threshold and Continuum“

verfasst von / submitted by

Angelika Widl, BSc

angestrebter akademischer Grad / in partial fulfilment of the requirements for the degree of

Master of Science (MSc)

Wien, 2018 / Vienna, 2018

Studienkennzahl lt. Studienblatt /
degree programme code as it appears on
the student record sheet:

A 066 876

Studienrichtung lt. Studienblatt /
degree programme as it appears on
the student record sheet:

Masterstudium Physik UG2002

Betreut von / Supervisor:

Univ.-Prof. Dr. André H. Hoang

Abstract

Future linear colliders will be able to measure the top quark mass with unprecedented accuracy using a threshold scan of the top quark pair production cross section. At threshold, the inclusive production cross section is known from non-relativistic QCD (NRQCD), while in the continuum it is calculated with usual fixed-order QCD. In the region between threshold and continuum the exact form of the inclusive cross section has been unknown up to now.

The aim of this thesis is to fill this gap by matching the velocity-NRQCD (vNRQCD) next-to-next-to-leading-logarithm (NNLL) threshold cross section to the next-to-next-to-next-to-leading-order (N^3 LO) QCD continuum cross section. We perform the matching for two cases: with the resummation of large logarithms of the velocity at threshold and without it. Apart from QCD effects, we include leading-order electroweak effects at threshold by shifting the center-of-mass energy into the complex plane. This gives the bulk of all contributions to the top quark pair production cross section at threshold. Furthermore, we use the MSR mass with an adjustable scale R in order to have a consistent mass scheme in the matching. This avoids the renormalon problem of the pole mass as well as the power counting breaking effects of the $\overline{\text{MS}}$ mass at threshold. In the continuum, we employ a switch-off function to turn off the non-relativistic contributions. By varying the switch-off function, we estimate the error in our matching.

Our results show that the matched cross section differs from both the vNRQCD and the QCD cross section in a region starting directly above the threshold peak to about 20 GeV above the threshold. In this region the matched cross section should be used instead of the QCD and vNRQCD cross section. On the other hand, the matched cross section is practically identical with the vNRQCD at threshold and with the QCD cross section for energies more than 20 GeV above the threshold, and they replace the matched cross section in these regions. Furthermore, the dependence of the matched cross section on the switch-off function decreases when going to higher orders, showing the consistency of the matching.

Abstract

Zukünftige Linearbeschleuniger versprechen hochpräzise Messungen der Top Quark Masse mittels eines Scans des Wirkungsquerschnittes an der Schwelle für Top Quark Paarerzeugung. Der inklusive Wirkungsquerschnitt direkt an der Schwelle wird mit nicht-relativistischer QCD (NRQCD) berechnet. Bei höheren Energien im Kontinuum kommt hingegen die Schleifenentwicklung der relativistischen QCD zur Anwendung. In dem Gebiet zwischen der Schwelle und dem Kontinuum war die genaue Form des inklusiven Wirkungsquerschnittes bis jetzt unbekannt.

Das Ziel dieser Arbeit ist es, den velocity-NRQCD (vNRQCD) Wirkungsquerschnitt auf der Ordnung NNLL mit dem QCD Wirkungsquerschnitt auf der Ordnung $N^3\text{LO}$ zusammenzufügen. Der resultierende Wirkungsquerschnitt wird untersucht sowohl mit als auch ohne Resummation von großen Logarithmen der Geschwindigkeit an der Schwelle. Neben QCD Effekten berücksichtigen wir auch elektroschwache Beiträge an der Schwelle auf führender Ordnung, welche zusammen mit den QCD Beiträgen den Großteil des gesamten Wirkungsquerschnitts zur Paarerzeugung von Top Quarks an der Schwelle geben. Außerdem verwenden wir die MSR Masse mit einer veränderbaren Skala R um ein konsistentes Massenschema an der Schwelle, im Kontinuum, und in der intermediären Region zu erhalten. Damit vermeiden wir sowohl das Renormalon-Problem der Polmasse, als auch Verletzungen des Power Countings durch die $\overline{\text{MS}}$ Masse an der Schwelle. Um keine nicht-relativistische Beiträge im Kontinuum zu haben, multiplizieren wir die nicht-relativistischen Beiträge mit einer sogenannten Switchoff-Funktion, die von 1 an der Schwelle kontinuierlich auf 0 im Kontinuum übergeht. Variationen dieser Funktion ermöglichen uns eine Abschätzung des Fehlers des Wirkungsquerschnitts in der intermediären Region.

Unsere Resultate zeigen, dass der zusammengefügte Wirkungsquerschnitt vom reinen vNRQCD Resultat schon direkt nach der Peak-Region der Schwelle abweicht. Der reine QCD-Wirkungsquerschnitt zeigt Abweichungen für Energien bis ca. 20 GeV oberhalb der Schwelle. Die Auswirkungen der Variation der Switchoff-Funktion nehmen von Ordnung zu Ordnung ab. Dies zeigt die Konsistenz unserer Methode.

Contents

1	Introduction	1
2	Continuum Contributions	3
2.1	Cross Section and Vacuum Polarization	3
2.2	Vacuum Polarization up to N^3LO	5
3	Threshold Contributions	8
3.1	Method of Regions at Threshold	9
3.1.1	Leading Order Contributions to the Threshold Cross Section	12
3.2	Introduction to Effective Field Theories	15
3.2.1	Example: b-Quark Decay	16
3.3	Introduction to vNRQCD	21
3.3.1	NRQCD, pNRQCD, and vNRQCD	21
3.3.2	vNRQCD Lagrangian	22
3.3.3	Power counting	34
3.3.4	Renormalization and Resummation of Logarithms	35
3.4	Top Quark Pair Production in vNRQCD	39
3.4.1	Production Current	39
3.4.2	LO, NLO, and NNLO Contributions	42
3.4.3	Resummation of the Coulomb Singularity	44
3.4.4	Electroweak and Non-Perturbative Effects	49
3.5	Analysis of the Threshold Contributions	52
4	Mass Schemes	57
4.1	Pole Mass	57
4.2	\overline{MS} Mass	60
4.3	1S Mass	61
4.4	MSR Mass	62
4.5	QCD Cross Section in the MSR Mass Scheme	64
5	Matching Threshold and Continuum Contributions	66
5.1	Matching Formula	66
5.2	Expanded Cross Section at Leading Order	68
5.3	Expanded Cross Section at Higher Orders	69
5.4	Mass Scheme	73
6	Results and Discussion	77
7	Conclusions	81
A	Optical Theorem	82
B	Method of regions	84
C	Derivation of the Schrödinger Green's Function	87

D	Multiloop Integrals	90
E	Running of the Strong Coupling α_s	94
F	Expansions of the QCD and the vNRQCD Cross Section	96
G	Coefficients of the Expanded Cross Section	101

Chapter 1

Introduction

The Standard Model (SM) of particle physics describes all known particles and interactions except gravity and its predictions have been in remarkable agreement with experimental measurements [1]. However, the Standard Model is known to be incomplete. For example, it describes neutrinos as massless particles, although experiments on neutrino oscillations prove that neutrinos have a small mass [2]. Also, there could be particles not included in the SM that are responsible for dark matter and many extensions of the Standard Model with new particles exist.

To find more inconsistencies with the SM that can point us in the right direction for extensions of the SM, two large linear colliders are currently in planning, the International Linear Collider (ILC) in Japan [3] and the Compact Linear Collider (CLIC) at CERN [4]. Instead of protons, they collide electrons with positrons, which reduces the QCD background in the measurements and makes it possible to measure the top quark and Higgs boson properties with unprecedented precision. Apart from finding new physics by looking for deviations of the SM parameters from theory, a future linear collider could also directly find new particles, which went undetected at the Large Hadron Collider (LHC) [5].

One of the corner stones of the future linear colliders is a high precision measurement of the top quark mass from a scan of the top quark pair production cross section at threshold. As the heaviest of all SM particles, the top quark is an important input parameter for global electroweak fits [6]. It also has a large effect on the stability of the electroweak vacuum [7] and a more precise measurement of its mass would finally clarify, if the electroweak vacuum is stable or metastable (in a model assuming no new particles up to the Planck scale).

On the theory side, top quark pair production can be treated very well in perturbation theory and non-perturbative effects are tiny. This is in contrast to all other quarks and is related to its large mass $m_t \sim 173 \text{ GeV}$ and width $\Gamma_t \sim 1.5 \text{ GeV}$. The large width originates from the top quark decay into a W boson and a bottom quark, and the top quark is the only quark with a mass large enough to make this decay possible.

At the moment, the most precise measurements of the top quark mass come from the direct reconstruction of the top decay products in $p\bar{p}$ collisions using Monte Carlo event generators and give $m_t^{\text{MC}} = 173.1(6) \text{ GeV}$ [1]. However, they determine the Monte Carlo mass m_t^{MC} , which is not a well-defined field theoretical mass. It is not clear at the moment, how to generally relate the Monte Carlo mass to a well defined field-theoretical mass. However, studies have been done to calibrate the Monte Carlo mass for specific observables [8].

Future linear colliders promise a large improvement on the uncertainty of the top quark mass measurement to about 50 MeV [9, 10], which is about a factor of 10 smaller than the current value. For this measurement, they perform a scan of the top quark pair production cross section at threshold. From the cross section, the top quark mass can be extracted in a well-defined field-theoretical mass scheme.

Calculations of the cross section of top quark pair production at threshold have advanced greatly in recent years. Since the perturbative series in α_s does not converge at threshold, the effective field theory non-relativistic QCD (NRQCD), or one of its derivatives vNRQCD or pNRQCD, is used instead of QCD. For the inclusive cross section, the calculations have reached next-to-next-to-leading-logarithmic (NNLL) order in vNRQCD [11] and next-to-next-to-next-to-leading-order N³LO accuracy in pNRQCD [12]. However, the NRQCD calculations are only valid directly at threshold and break down when going to higher center-of-mass (CM) energies. QCD, on the other hand, correctly predicts the cross section in the continuum, i.e. at high energies away from the threshold, but breaks down at threshold.

Not many studies so far have focused on the intermediate region between threshold and continuum. This region is important for a number of reasons. First, the luminosity spectrum smears out the CM energy and the intermediate region could therefore also contribute to measurements of the threshold cross section. Secondly, CLIC plans to have a run also above the threshold at 380 GeV, i.e. in the intermediate region, where a mass measurement of the top quark mass from radiative events could supplement the one from the threshold. For this a continuous cross section from the threshold to the continuum is needed.

A matching between threshold and continuum has been implemented in the event generator Whizard for the differential cross section by including NLL threshold resummations as a form factor in the fixed-order NLO QCD cross section [13].

However, a matching for higher orders (up to NNLL in vNRQCD and N³LO in QCD) for the inclusive cross section has not been investigated so far. We present first studies to fill this gap.

This thesis presents the threshold-continuum matching of the inclusive cross section of double-resonant top quark pair production up to NNLL in vNRQCD and N³LO in QCD. For a first study, we restrict ourselves to the photon induced production cross section with leading-order electroweak effects at threshold. We will first describe the calculations of the contributions in the continuum and at threshold separately, and then present our approach to combine them to a matched cross section.

The structure of this thesis is as follows. In Chapter 2 we describe the form of the QCD cross section in the continuum with the optical theorem. Chapter 3 is dedicated to the threshold region. It gives an introduction to effective field theories in general and to vNRQCD specifically. Using the vNRQCD formalism, the form of the cross section at threshold is derived. In Chapter 4 we describe mass schemes for the threshold, continuum, and intermediate region. The mass schemes typically used at threshold are inadequate in the continuum and vice versa. For a mass scheme valid in all regions, we discuss the MSR mass. The matching of the threshold and continuum contributions is presented in Chapter 5 and the results are discussed in Chapter 6. Finally, Chapter 7 concludes and gives an outlook for future studies of the matched cross section.

Chapter 2

Continuum Contributions

For the matching we will consider the inclusive top quark pair production cross section with photon exchange

$$\sigma = \sigma(e^+e^- \rightarrow \gamma^* \rightarrow t\bar{t} + X) \quad (2.1)$$

and include QCD corrections as well as leading order electroweak effects at threshold. The cross section is related to the top quark vector current induced vacuum polarization via the optical theorem (Section 2.1) and for center-of-mass (CM) energies above 400 GeV (continuum), QCD can be used to calculate an expansion in the strong coupling constant α_s . We call this cross section σ_{QCD} . It is known up to 3 loops (Section 2.2).

For CM energies around $\sqrt{s} \sim 2m_t \sim 345$ GeV (threshold) the velocity v of the top and anti-top quark is small and the expansion has to be done in both v and α_s simultaneously. We describe the calculation of the cross section in this expansion with the effective field theory (EFT) vNRQCD in Chapter 3 and call it σ_{vNRQCD} .

We will now use the optical theorem to relate σ_{QCD} to the vacuum polarization $\Pi^{\mu\nu}$ and present the results for the vacuum polarization up to N³LO.

2.1 Cross Section and Vacuum Polarization

Inclusive cross sections can be calculated from the forward scattering amplitude with the optical theorem (see Appendix A). For the unpolarized cross section, the optical theorem takes the form

$$\begin{aligned} \sigma_{\text{tot}}(e^+e^- \rightarrow \gamma^* \rightarrow t\bar{t}) &= \sum_f \int d\Pi_f \left| \text{Diagram} \right|^2 \\ &= \frac{1}{s} \text{Im} \left[(-i) \text{Diagram} \right], \end{aligned} \quad (2.2)$$

The first diagram shows an incoming electron-positron pair (e^+ and e^-) interacting via a photon (wavy line) with a shaded blob representing the vacuum polarization. From this blob, a top quark (t) and an anti-top quark (\bar{t}) emerge. The second diagram is similar but includes an additional photon exchange between the electron-positron pair and the top quark-anti-top quark pair, also represented by shaded blobs.

where \sqrt{s} is the total energy in the CM frame. The sum in the first line goes over all possible final states $t\bar{t} + X$ and $d\Pi_f$ denotes the phase space of the final state particles. The gray blobs stand for all possible QCD corrections to the vertex and the heavy quark vacuum polarization, respectively. Furthermore, we assume the electron and positron to be massless, because the CM energy for top quark pair production at threshold is $2m_t \sim 345$ GeV and therefore much larger than the electron mass $m_e \sim 0.5$ MeV. We deliberately denoted the cross section here as σ_{tot} instead of σ_{QCD} , because the following calculation applies to both the vNRQCD and the QCD cross section.

The factor $(-i)$ in front of the diagram in the last line of Equation (2.2) is needed, because in QFT one usually calculates the amplitude $i\mathcal{M}$ (i.e. the Feynman diagram in Equation (2.2)) and then only uses \mathcal{M} for the optical theorem, cross section, and decay rates. The $(-i)$ removes the unwanted factor of i .

The diagram in the second line of Equation (2.2) can be related to the heavy quark vacuum polarization $\Pi^{\mu\nu}$, which is defined as the correlator of two electromagnetic currents of the form $j^\mu(x) = \bar{\psi}(x) \gamma^\mu \psi(x)$:

$$\text{Diagram: a circle with diagonal lines, two wavy lines attached to it, one labeled } q \text{ and the other } q, \text{ with } t \text{ and } \bar{t} \text{ labels above and below the circle} = i\Pi^{\mu\nu}(q) = \int d^4x e^{iqx} \langle 0 | T j^\mu(x) j^\nu(0) | 0 \rangle . \quad (2.3)$$

Using Lorentz invariance and the Ward identity $q_\mu \Pi^{\mu\nu}(q) = 0$, the Lorentz structure of $\Pi^{\mu\nu}$ can be extracted:

$$\Pi^{\mu\nu}(q) = (g^{\mu\nu} q^2 - q^\mu q^\nu) \Pi(q^2) . \quad (2.4)$$

With $s = (p_1 + p_2)^2 = q^2$ the diagram in Equation (2.2) then takes the form

$$\begin{aligned} \text{Diagram: a circle with diagonal lines, two wavy lines attached to it, one labeled } q \text{ and the other } q, \text{ with } p_1, p_2 \text{ labels on the left and } p_1, p_2 \text{ labels on the right} = \\ = \frac{1}{4} \sum_{r,s} Q_t^2 (-ie)^4 [\bar{v}^r(p_1) \gamma_\mu u^s(p_2)] \frac{-i}{q^2 + i\varepsilon} i\Pi^{\mu\nu}(q) \frac{-i}{q^2 + i\varepsilon} [\bar{u}^s(p_2) \gamma_\nu v^r(p_1)] \\ = -i Q_t^2 \frac{e^4}{s^2} L_{\mu\nu} \Pi^{\mu\nu}(q) \\ = -i Q_t^2 \frac{e^4}{s^2} L_{\mu\nu} \Pi(q^2) q^2 g^{\mu\nu} , \end{aligned} \quad (2.5)$$

where $Q_t = 2/3$ is the charge of the top quark. $L_{\mu\nu} = \frac{1}{4} \sum_{r,s} [\bar{v}^r(p_1) \gamma_\mu u^s(p_2)] [\bar{u}^s(p_2) \gamma_\nu v^r(p_1)]$ is the leptonic tensor, and the sum over r, s averages the spins of the incoming particles. In the last line we used Equation (2.4), where the second part of (2.4) vanishes because of the Dirac equation:

$$\bar{v}(p_1) \not{q} u(p_2) = \bar{v}(p_1) (\not{p}_1 + \not{p}_2) u(p_2) = 0 .$$

Rewriting $L_{\mu\nu}$ as a trace and using the spin sums $\sum_s u^s(p) \bar{u}^s(p) = \sum_s v^s(p) \bar{v}^s(p) = \not{p}$, where $m_e = 0$, the leptonic part of Equation (2.5) takes the simple form

$$\begin{aligned} L_{\mu\nu} g^{\mu\nu} &= g^{\mu\nu} \frac{1}{4} \sum_{r,s} \text{Tr} [\bar{v}^r(p_1) \gamma_\mu u^s(p_2) \bar{u}^s(p_2) \gamma_\nu v^r(p_1)] \\ &= \frac{1}{4} \text{Tr} [\not{p}_1 \gamma_\mu \not{p}_2 \gamma^\mu] \\ &= -\frac{1}{2} \text{Tr} [\gamma^\alpha \gamma^\beta] (p_2)_\alpha (p_1)_\beta \\ &= -2 (p_1 \cdot p_2) \\ &= -s . \end{aligned} \quad (2.6)$$

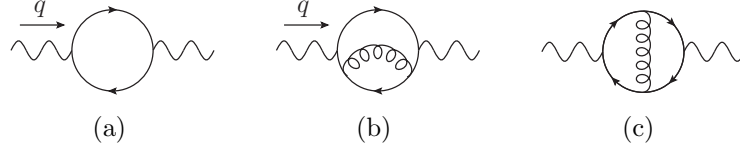


Figure 2.1: Contributions to Π_0 and Π_1

Finally, we combine Equations (2.2), (2.5) and (2.6) and obtain

$$\sigma_{\text{tot}} = 12\pi Q_t^2 \sigma_{\text{pt}} \text{Im} \Pi(s + i\varepsilon) , \quad (2.7)$$

where $\sigma_{\text{pt}} = e^4/(12\pi s) = 4\pi\alpha^2/(3s)$ and α is the electromagnetic coupling constant. The infinitesimal term $(+i\varepsilon)$ ensures that the correct branches are chosen for the imaginary part.

Equation (2.7) can also be written with $\Pi^{\mu\nu}$, which we will need in Chapter 3. For this we note that from Equation (2.4) follows

$$\Pi_\mu^\mu(q^2) = 3q^2 \Pi(q^2) , \quad (2.8)$$

where we have changed the notation of $\Pi_\mu^\mu(q)$ to $\Pi_\mu^\mu(q^2)$ to express that the vacuum polarization with contracted indices only depends on the square of q . Using Π_μ^μ Equation (2.7) can be rewritten in the form

$$\sigma_{\text{tot}} = F(s) \text{Im} [\Pi_\mu^\mu(s + i\varepsilon)] , \quad F(s) = \frac{4\pi}{s} Q_t^2 \sigma_{\text{pt}} . \quad (2.9)$$

2.2 Vacuum Polarization up to N³LO

The top quark vacuum polarization is known up to order N³LO, i.e. up to α_s^3 . It can be written as

$$\Pi(z) = \Pi_0(z) + C_F \left(\frac{\alpha_s^{(n_f)}(\mu)}{\pi} \right) \Pi_1(z) + \left(\frac{\alpha_s^{(n_f)}(\mu)}{\pi} \right)^2 \Pi_2(z, \mu) + \left(\frac{\alpha_s^{(n_f)}(\mu)}{\pi} \right)^3 \Pi_3(z, \mu) + \mathcal{O}(\alpha_s^4) , \quad (2.10)$$

where α_s is renormalized in the $\overline{\text{MS}}$ scheme with n_f active flavors and $z = q^2/4m_t^2$ with the top quark pole mass m_t . Π_0, \dots, Π_3 are the vacuum polarization contributions up to four loops.

Π_0 consists of the one loop diagram shown in Figure 2.1a and its calculation can be found in many textbooks (e.g. [14, 15]). Its result reads (with the notation from [16]):

$$\Pi_0(z) = -(-i) \frac{N_c}{3q^2} \int \frac{d^4k}{(2\pi)^4} \frac{\text{Tr} [\gamma^\mu i(\not{k} - \not{q} + m) \gamma_\mu i(\not{k} + m)]}{[(k-q)^2 - m^2 + i\varepsilon] [k^2 - m^2 + i\varepsilon]} \quad (2.11)$$

$$= \frac{N_c}{16\pi^2} \left(\frac{20}{9} + \frac{4}{3z} - \frac{4(1-z)(1+2z)}{3z} G(z) \right) , \quad (2.12)$$

where

$$G(z) = \frac{2u \ln u}{u^2 - 1} \quad \text{and} \quad u = \frac{\sqrt{1 - 1/z} - 1}{\sqrt{1 - 1/z} + 1} \quad (2.13)$$

and $N_c = 3$ is the number of colors.

Π_1 includes the two-loop diagrams shown in Figure 2.1. An analytic result for Π_1 was first derived in [17] and recalculated e.g. with a dispersive approach in [18] and with integration by parts in [16]. It reads [16]:

$$\Pi_1(z) = \frac{N_c}{16\pi^2} \left[\frac{5}{6} + \frac{13}{6z} - \frac{(1-z)(1-16z)}{6z} G^2(z) - \frac{(1+2z)}{6z} \left(1 + 2z(1-z) \frac{d}{dz} \right) \frac{I(z)}{z} \right], \quad (2.14)$$

where

$$I(z) = 6 [\zeta_3 + 4 \operatorname{Li}_3(-u) + 2 \operatorname{Li}_3(u)] - 8 [2 \operatorname{Li}_2(-u) + \operatorname{Li}_2(u)] \log u - 2 [2 \log(1+u) + \log(1-u)] \log^2 u \quad (2.15)$$

and $C_F = 4/3$.

For Π_2 and Π_3 no fully analytic result exists. However, expansions in the limits $q^2 \rightarrow \infty$, $q^2 \rightarrow 4m^2$, and $q^2 \rightarrow 0$ are known and allow an approximation of the full amplitude with Padé approximants [19]. Recently, also a numerical result for Π_2 has been obtained in [20]. For the matching we will use the implementation of [19] for Π_2 and Π_3 . In [19] the vacuum polarization was calculated with $n_f = 6$ running flavors. Since the scales at threshold are much smaller than the top mass, the coupling at threshold only runs with $n_f = 5$ flavors and accordingly we change $\alpha_s^{(n_f=6)}$ to $\alpha_s^{(n_f=5)}$ for the matching, see Equation (D.4).

Figure 2.2a shows the total cross section σ_{tot} from Equation (2.7) at different orders in α_s with the analytical expressions from Equation (2.11) and Equation (2.14) for Π_0 and Π_1 , respectively, and with Padé approximations for Π_2 and Π_3 as described in [19]. The error bands are generated by varying the renormalization scale μ between $m_t/2 < \mu < 2m_t$ and the middle line corresponds to the default value $\mu = m_t$. The plot already shows the breakdown of the QCD calculation for energies near threshold ($\sqrt{s} = 2m_t$). While in the continuum above 400 GeV the error bands of the curves overlap, at threshold we can see a large gap between the NLO and NNLO curve. Additionally, the contributions from Π_2 and Π_3 diverge and make an accurate prediction from the QCD cross section impossible.

At threshold, leading order electroweak effects become important, as we will see in Section 3.4.4. They can be included at threshold in σ_{vnrQCD} using the replacement

$$\sqrt{s} + i\varepsilon \rightarrow \sqrt{s} + i\Gamma, \quad (2.16)$$

where $\Gamma \sim 1.5 \text{ GeV}$ is the decay width of the top quark. To be consistent in the matching, we make the same replacement in the vacuum polarization Π appearing in Equation (2.7). Figure 2.2b shows σ_{QCD} with the replacement of (2.16). The sharp drop of the cross section is then smeared out, leaving a smooth lineshape. The unphysical behavior at threshold is however still clearly visible.

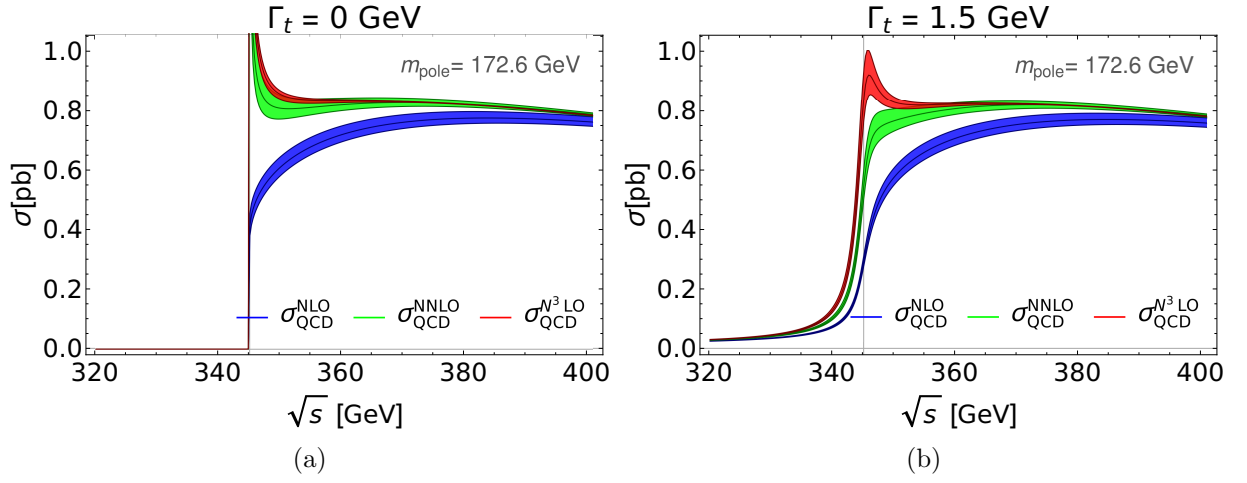


Figure 2.2: Top quark pair production cross section in QCD up to N³LO with (b) and without (a) a shift of the CM energy \sqrt{s} into the complex plane.

Chapter 3

Threshold Contributions

At threshold, the top quark pair is produced with a small relative velocity and forms a Coulomb-like system, similar to the Hydrogen atom. For Coulombic systems the virial theorem relates the kinetic and potential energy and gives the relation

$$v \sim \alpha_s \sim 0.1 . \quad (3.1)$$

Three scales govern the physics of the top quark pair at small velocities: the mass of the top quarks m_t , their momentum $\mathbf{p} \sim mv$, and their energy $E \sim mv^2$. Here v denotes the velocity of one of the quarks in the center-of-mass frame. The three scales have a large separation among each other and are all much larger than Λ_{QCD} :

$$m \gg mv \gg mv^2 \gg \Lambda_{\text{QCD}} . \quad (3.2)$$

Together with its large width $\Gamma_t \gg \Lambda_{\text{QCD}}$, this makes the $t\bar{t}$ system the only quarkonium system that can be treated fully in perturbation theory. However, as we have seen in the last chapter, one can not simply take the perturbative QCD result at threshold. Two kinds of large contributions arise for small v and spoil the perturbation series in the expansion in the number of loops: terms from the Coulomb singularity and large logarithms of v .

The Coulomb singularity is generated by a potential, which is at first order the same as the Coulomb potential known from non-relativistic quantum mechanics. With this potential one obtains the contributions

$$v, \alpha_s, \alpha_s^2/v, \alpha_s^3/v^2, \dots . \quad (3.3)$$

Because $\alpha_s \sim v$ they are all equally large and need to be summed to all orders. They can be calculated either with the method of regions from the QCD amplitudes or in the framework of the effective field theory NRQCD (non-relativistic QCD), or one of its derivatives vNRQCD (velocity NRQCD) [21] or pNRQCD (potential NRQCD) [22]. To sum the Coulomb terms, a Bethe-Salpeter type integral equation can be used, which is for top quark pair production just the well-known Schrödinger equation from quantum mechanics.

Large logarithms in v arise because of the widely separated scales from Equation (3.2). The problem of large logarithms is quite general and usually appears in perturbative QFT calculations containing widely separated scales. There, logarithms of the scales will appear in the cross section and degrade the perturbative expansion. For top quark pair production at threshold the logarithms appear in the form

$$\begin{aligned}\log(p/m) &\sim \log(v) \\ \log(E/m) &\sim \log(v^2) .\end{aligned}\tag{3.4}$$

They become sizeable at threshold, where $\alpha_s \log v \sim 0.25$ and $\alpha_s \log v^2 \sim 0.5$. The contributions

$$\alpha_s \log v, \alpha_s^2 \log^2 v, \alpha_s^3 \log^3 v, \dots\tag{3.5}$$

therefore converge very slowly and can be considered parametrically of $\mathcal{O}(1)$.

Effective field theories (EFTs) provide a framework to sum these logarithmic contributions to all orders with the renormalization group (RG) running of so-called Wilson coefficients. At threshold, vNRQCD provides a consistent resummation of the large logarithms.

While the Coulomb resummation is mandatory, different approaches with and without the logarithm resummation exist at threshold. We will call calculations with the resummation of the logarithms renormalization group improved (RGI) and results without it fixed-order (FO).

The highest precision up to now has been achieved with vNRQCD and pNRQCD. In vNRQCD the renormalization group improved (RGI) calculation is complete up to next-to-next-to-leading-logarithm (NNLL) for all practical purposes [11]. In pNRQCD the fixed-order (FO) perturbation theory result has reached next-to-next-to-next-to leading order (N³LO) precision [12].

For the matching we will use vNRQCD in an RGI and FO setting.

In this chapter we first present the method of regions for the threshold region and use it to calculate the leading order contributions for small v (Section 3.1). Higher order contributions are more easily calculated in vNRQCD, which we also need for resumming logarithms of v .

After giving an introduction to effective field theories in Section 3.2, we will derive the vNRQCD Lagrangian in Section 3.3 and explain the resummation of logarithms.

Section 3.4 then applies vNRQCD to top quark pair production at threshold and explains how the Coulomb singularity is resummed with the Schrödinger equation. Furthermore, it shows how leading order electroweak effects are implemented with the replacement from Equation (2.16) and discusses higher order electroweak effects. Lastly, Section 3.5 presents an analysis of the top quark pair production cross section at threshold for both the FO and the RGI set up.

3.1 Method of Regions at Threshold

The method of regions is a powerful tool to calculate asymptotic expansions of Feynman integrals. It is basically an expansion under the integral sign *in the integration variable*. The details are described in appendix B. The application of the method of regions at threshold was developed in [23] and is also known as "threshold expansion".

To calculate integrals in the threshold expansion, we first have to identify all regions where physical scales contribute to loop integrals. Since we have the three scales m , $\mathbf{p} \sim mv$, and $E \sim mv^2$, we might guess that there are the following three regions for a loop integral with the momentum $k^\mu = (k^0, \mathbf{k})$:

$$\begin{aligned}\text{hard region:} \quad & (k^0, \mathbf{k}) \sim (m, m) \\ \text{soft region:} \quad & (k^0, \mathbf{k}) \sim (mv, mv) \\ \text{ultrasoft region:} \quad & (k^0, \mathbf{k}) \sim (mv^2, mv^2) .\end{aligned}\tag{3.6}$$

These regions indeed contribute, but there is one more region. Since the heavy quark propagator becomes on-shell for $E \sim \mathbf{p}^2/2m$, the so-called "potential" region has to be considered, too:

$$\text{potential region: } (k^0, \mathbf{k}) \sim (mv^2, mv) . \quad (3.7)$$

Using these four regions, we can calculate Feynman amplitudes at threshold as an expansion in v . To illustrate how the threshold expansion works, let us consider the LO QCD vacuum polarization from Equation (2.12) at threshold. We will work in the center-of-mass frame, where the momentum q from Equation (2.3) takes the form

$$q^\mu = (q_0, \mathbf{0}) = (E_{\text{rel}}, \mathbf{0}) . \quad (3.8)$$

E_{rel} is the relativistic center-of-mass energy and related to the non-relativistic energy $E_{\text{nr}} = mv^2$ by

$$q_0 = E_{\text{rel}} = \frac{2m}{\sqrt{1-v^2}} = 2m + mv^2 + \mathcal{O}(v^4) = 2m + E_{\text{nr}} + \mathcal{O}(v^4) . \quad (3.9)$$

To first order in v^2 we therefore have:

$$q_0^2/4 - m^2 \simeq m E_{\text{nr}} . \quad (3.10)$$

In the CM frame only the spatial part Π^{ij} of the vacuum polarization is non-zero, as can be seen by plugging Equation (3.8) into Equation (2.4):

$$\begin{aligned} \Pi^{00} &= 0 \\ \Pi^{0i} &= 0 \\ \Pi^{ij} &= g^{ij} q_0^2 \Pi \quad \text{for } i, j = 1, 2, 3 . \end{aligned} \quad (3.11)$$

For the threshold expansion it turns out that a "canonical" routing of q in the loop makes the counting most transparent. For this, q is split up such that $q/2$ flows through the upper and $q/2$ through the lower part of the loop, respectively.

Using Equations (3.8) and (3.10) together with the canonical routing of q , the integral from Equation (2.11) in dimensional regularization becomes

$$\begin{aligned} \Pi_0^{\mu\nu} &= -(-i) \tilde{\mu}^{2\varepsilon} N_c \int \frac{d^d k}{(2\pi)^d} \frac{\text{Tr} [\gamma^\mu i(\not{k} - \not{q}/2 + m) \gamma^\nu i(\not{k} + \not{q}/2 + m)]}{[(k - q/2)^2 - m^2]_+ [(k + q/2)^2 - m^2]_+} \\ &= -4i \tilde{\mu}^{2\varepsilon} N_c \int \frac{d^d k}{(2\pi)^d} \frac{2k^\mu k^\nu - q^\mu q^\nu/2 + g^{\mu\nu}(mE - k^2 + 2m^2)}{[k^2 + k^0 q^0 + mE]_+ [k^2 - k^0 q^0 + mE]_+} , \end{aligned} \quad (3.12)$$

where a factor of $(-i)$ was included, because we write Π here instead of $i\Pi$. The subscript signifies the sign of the infinitesimal imaginary part: $[\dots]_\pm = (\dots \pm i\varepsilon)$. Using (3.6) and (3.7) to expand in the different regions and taking only the spatial part of $\Pi^{\mu\nu}$, the integral splits into four parts:

$$\Pi_0^{ij} = (\Pi_0^{ij})_{\text{hard}} + (\Pi_0^{ij})_{\text{potential}} + (\Pi_0^{ij})_{\text{soft}} + (\Pi_0^{ij})_{\text{ultrasoft}} \quad (3.13)$$

with

$$\begin{aligned}
(\Pi_0^{ij})_{\text{hard}} &= -4i \tilde{\mu}^{2\varepsilon} N_c \int \frac{d^d k}{(2\pi)^d} \frac{2k^i k^j + g^{ij}(-k^2 + 2m^2)}{[k^2 + k^0 q^0]_+ [k^2 - k^0 q^0]_+} \\
(\Pi_0^{ij})_{\text{potential}} &= -4i \tilde{\mu}^{2\varepsilon} N_c \int \frac{d^d k}{(2\pi)^d} \frac{g^{ij} 2m^2}{[mE - \mathbf{k}^2 + k_0 q_0]_+ [mE - \mathbf{k}^2 - k_0 q_0]_+} \\
(\Pi_0^{ij})_{\text{soft}} &= -4i \tilde{\mu}^{2\varepsilon} N_c \int \frac{d^d k}{(2\pi)^d} \frac{g^{ij} 2m^2}{[k_0 q_0]_+ [-k_0 q_0]_+} \\
(\Pi_0^{ij})_{\text{ultrasoft}} &= -4i \tilde{\mu}^{2\varepsilon} N_c \int \frac{d^d k}{(2\pi)^d} \frac{g^{ij} 2m^2}{[k_0 q_0 + mE]_+ [-k_0 q_0 + mE]_+} .
\end{aligned} \tag{3.14}$$

Π_{hard} can be calculated using partial fractions and Feynman parameters. Expanding in $d = 4 - 2\varepsilon$, its result reads:

$$(\Pi_0^{ij})_{\text{hard}} = \frac{3m^2}{2\pi} g^{ij} \left[\frac{2}{3\varepsilon} \frac{1}{\pi} + \frac{2}{3\pi} \log \left(\frac{\mu^2}{m^2} \right) + \frac{16}{9\pi} + \mathcal{O}(v^2) \right] , \tag{3.15}$$

where $\tilde{\mu}^2 = \mu^2 e^{\gamma_E}/4\pi$. Equation (3.15) has no imaginary part and therefore drops out in the total cross section. We could have seen this already before solving the integral: The quark propagators can not become on-shell for $(k^0, \mathbf{k}) \sim (m, m)$. By the optical theorem, the result can therefore not have an imaginary part.

The potential region gives a finite result. Performing the k^0 integration in Equation (3.14) by closing the contour either in the upper or lower complex plane, one obtains

$$(\Pi_0^{ij})_{\text{potential}} = 24i m^2 g^{ij} \tilde{\mu}^{2\varepsilon} \int \frac{d^n k}{(2\pi)^n} \frac{i}{2q_0 (mE - \mathbf{k}^2)} \tag{3.16}$$

and using Equation (D.4), the remaining integral evaluates to

$$(\Pi_0^{ij})_{\text{potential}} = i v \frac{3m^2}{2\pi} g^{ij} , \tag{3.17}$$

where $v = \sqrt{E/m}$. Lastly, the soft and ultrasoft integrals are scaleless and vanish:

$$(\Pi_0^{ij})_{\text{soft}} = (\Pi_0^{ij})_{\text{ultrasoft}} = 0 . \tag{3.18}$$

We can check the result by expanding the full amplitude from Equation (2.12) and using Equation (2.4):

$$\Pi_0^{ij} = \frac{3m^2}{2\pi} g^{ij} \left(\frac{2}{3\varepsilon} \frac{1}{\pi} + \frac{2}{3\pi} \log \left(\frac{\mu^2}{m^2} \right) + \frac{16}{9\pi} + i v + \mathcal{O}(v^2) \right) . \tag{3.19}$$

Comparing Equation (3.19) with the results of Equation (3.15) and (3.17), we see that the threshold expansion has indeed reproduced all terms correctly. Thus, we showed that expanding the integral in v before the integration gives the same result as expanding it after the integration.

The threshold expansion has the useful feature that we can determine which power of v the result will have *without* solving the integral. For example, in Equation (3.14), Π_{hard} will only contribute to the endresult in the region where $d^4 k$ scales as m^4 . The integrand scales as m^{-2} . The result

$$\begin{aligned}
\frac{\pm \not{q}/2 + \not{p} + m}{[(\pm q/2 + p)^2 - m^2]_+} &= \frac{m(1 \pm \gamma_0)}{[mE \pm 2m p^0 - \mathbf{p}^2]_+} + \mathcal{O}(1/v) \\
&= \frac{\pi_\pm}{[E/2 \pm p^0 - \mathbf{p}^2/2m]_+} + \mathcal{O}(1/v) ,
\end{aligned} \tag{3.24}$$

where

$$\pi_\pm = \frac{1}{2} (1 \pm \gamma_0) . \tag{3.25}$$

Using Equation (3.24) together with the identity

$$\text{Tr} [\gamma^i \pi_- (\gamma^{\alpha_1} \pi_- \gamma^{\alpha_2} \dots \gamma^{\alpha_n} \pi_-) \gamma^j \pi_+ (\gamma_{\alpha_n} \pi_+ \gamma_{\alpha_{n-1}} \pi_+ \dots \gamma_{\alpha_1} \pi_+)] = 2 g^{ij} (-1)^n , \tag{3.26}$$

which can be easily derived by contracting the indices $\alpha_1, \alpha_2, \dots$, Equation (3.23) takes the form

$$\begin{aligned}
-i \left[\text{diagram} \right]_{\text{pot}} &= \\
&= i N_c (2 g^{ij}) \tilde{\mu}^{4\varepsilon} \int \frac{d^d p_1}{(2\pi)^d} \frac{d^d p_2}{(2\pi)^d} \frac{i (4\pi\alpha_s) C_F}{[\mathbf{p}_2^2]_-} \frac{i}{[E/2 - p_1^0 - \mathbf{p}_1^2/2m]_+} \frac{i}{[E/2 + p_1^0 - \mathbf{p}_1^2/2m]_+} \\
&\quad \times \frac{i}{[E/2 - (p_1^0 + p_2^0) - (\mathbf{p}_1 + \mathbf{p}_2)^2/2m]_+} \frac{i}{[E/2 + (p_1^0 + p_2^0) - (\mathbf{p}_1 + \mathbf{p}_2)^2/2m]_+} .
\end{aligned} \tag{3.27}$$

From this expansion the power in v of the result can already be determined. In the potential region $p^0 \sim v^2$ and $\mathbf{p} \sim v$, so the gluon and quark propagators both scale with v^{-2} (where we left out the scaling in m , because it is the same for every diagram). Together with $d^4 p \sim v^5$, the above expression then scales with $v^0 \alpha_s$.

To see if Equation (3.27) is indeed of order $v^0 \alpha_s$, we perform the p_1^0 and p_2^0 integrals. The integrand has the pole structure shown in Figure 3.1a and closing the contour in either the upper or the lower complex plane gives

$$\begin{aligned}
-i \left[\text{diagram} \right]_{\text{pot}} &= \\
&= i N_c (2 g^{ij}) \tilde{\mu}^{4\varepsilon} \int \frac{d^n p_1}{(2\pi)^n} \frac{d^n p_2}{(2\pi)^n} \frac{i (4\pi\alpha_s) C_F}{[\mathbf{p}_2^2]_-} \frac{i}{[E - \mathbf{p}_1^2/m]_+} \frac{i}{[E - (\mathbf{p}_1 + \mathbf{p}_2)^2/m]_+} \\
&= N_c (2 g^{ij}) (4\pi \alpha_s C_F) m^2 \text{I}^{(2)}(1, 1, 1, mE) ,
\end{aligned} \tag{3.28}$$

where $n = 3 - 2\varepsilon$ and $\text{I}^{(2)}(1, 1, 1, mE)$ denotes the two-loop integral. $\text{I}^{(2)}$ is solved in appendix D.

Using $E = mv^2$ and the solution for $\text{I}^{(2)}$ given in Equation (D.8), one obtains:

$$\begin{aligned}
-i \left[\text{diagram} \right]_{\text{pot}} &= \frac{N_c (2 g^{ij}) (4\pi \alpha_s C_F)}{32 \pi^2} m^2 \left[\frac{1}{2\varepsilon} + 1 + \log \left(-\frac{\mu^2}{Em} \right) - 2 \log 2 \right] \\
&= \alpha_s \frac{2 m^2}{\pi} \left[\frac{1}{4\varepsilon} + \frac{1}{2} + \frac{1}{2} \log \left(\frac{\mu^2}{m^2} \right) - \log(-iv) - \log 2 \right] g^{ij}, \quad (3.29)
\end{aligned}$$

which is indeed of order $\alpha_s v^0$.

The other diagrams are of the form shown in Figure 2.1b, where the gluon line can be attached to either the lower or the upper quark line. The corresponding integrals contain the term

$$\int \frac{d^d p}{(2\pi)^d} \frac{i (4\pi \alpha_s) C_F}{[\mathbf{p}^2]_-} \frac{i}{[E/2 - p_0 - \mathbf{p}^2/2m]_+}. \quad (3.30)$$

This integral has only one pole in p_0 in the upper complex plane (see Figure 3.1b). Upon closing the contour in the lower complex plane, the integral vanishes.

At $\mathcal{O}(\alpha_s^2)$ the lowest order term in v comes from the purely potential region of just one diagram. The calculation of its threshold expansion follows the same steps as for the two-loop integral. The p_0 loop integrations have again residues in the form shown in Figure 3.1a and evaluate to

$$\begin{aligned}
-i \left[\text{diagram} \right]_{\text{pot}} &= i N_c (2 g^{ij}) \tilde{\mu}^{6\varepsilon} \int \frac{d^n p_1}{(2\pi)^n} \frac{d^n p_2}{(2\pi)^n} \frac{d^n p_3}{(2\pi)^n} \frac{i (4\pi \alpha_s) C_F}{[\mathbf{p}_2^2]_-} \frac{i (4\pi \alpha_s) C_F}{[\mathbf{p}_3^2]_-} \\
&\quad \times \frac{i}{[E - \mathbf{p}_1^2/m]_+} \frac{i}{[E - (\mathbf{p}_1 + \mathbf{p}_2)^2/m]_+} \frac{i}{[E - (\mathbf{p}_1 + \mathbf{p}_2 + \mathbf{p}_3)^2/m]_+}. \quad (3.31)
\end{aligned}$$

Using Equation (D.19) for the remaining loop integrals, one obtains

$$\begin{aligned}
-i \left[\text{diagram} \right]_{\text{pot}} &= N_c (2 g^{ij}) (4\pi \alpha_s C_F)^2 m^3 \text{I}^{(3)}(1, 1, 1, 1, 1, mE) \\
&= i \frac{\alpha_s^2}{v} \frac{2\pi m^2}{9} g^{ij}. \quad (3.32)
\end{aligned}$$

All other $\mathcal{O}(\alpha_s^2)$ diagrams have at least one loop momentum with the structures shown in Figure 3.1b and 3.1c, and therefore evaluate to zero.

At higher orders in α_s the pattern from the two- and three-loop integrals continues: The purely

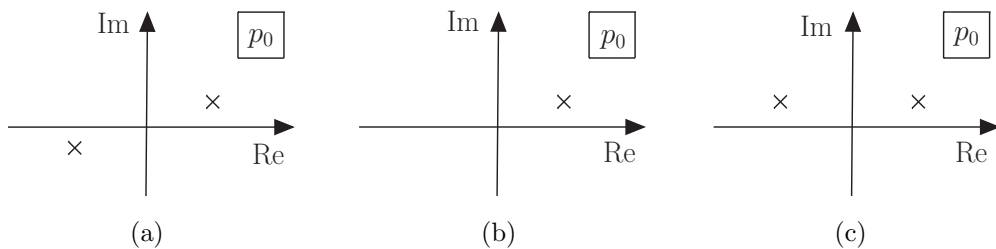


Figure 3.1: Pole structures appearing in the p_0 integrations. (a) gives a non-zero, (b) and (c) a zero contribution in the integration over p_0 .

potential region of the ladder diagrams is the only one that contributes at leading order and every additional gluon contributes a factor α_s/v . Since $\alpha_s \sim v$, the ladder contributions are all of the same order and need to be resummed. We will achieve this with the Schrödinger equation in Section 3.4.3.

At higher orders in the v expansion, the hard and soft regions will also contribute in form of mixed contributions with the potential region. Since the method of regions becomes increasingly complicated at these orders, it is useful to calculate the contributions with the effective field theory vNRQCD instead. vNRQCD is constructed specifically for heavy quarkonia systems at threshold and leaves out all non-resonant degrees of freedom. Additionally, it can resum the large logarithms of the form $(\alpha_s \log(v))^i$, which is not possible with the method of regions.

3.2 Introduction to Effective Field Theories

Effective field theories (EFTs) describe physics in certain energy limits and neglect all degrees of freedom that are not relevant to the problem at hand. In quantum field theory this improves calculations in two ways: approximate symmetries become manifest and large logarithms can be resummed.

Large logarithms generally appear in calculations containing widely separated scales. For example, an amplitude in a theory with two scales m_1 and m_2 , where $m_2 \gg m_1$, has typically the form

$$\mathcal{A} = \sum_{i=1}^{\infty} \alpha_s^i \sum_{j=0}^{\infty} c_{i,j} \left[\alpha_s \log \left(\frac{m_2}{m_1} \right) \right]^j. \quad (3.33)$$

If one scale is much larger than the other, the logarithms also become large. They degrade the convergence of the perturbation series and for

$$\alpha_s \log \left(\frac{m_2}{m_1} \right) \gtrsim 1 \quad (3.34)$$

the perturbation series will break down. EFTs solve this problem by summing the large logarithms such that the second sum in Equation (3.33) includes terms to all orders. The first sum can then be safely truncated at some finite power of α_s .

Because of the large logarithms, EFTs often not only simplify calculations by excluding degrees of freedom not relevant to the problem, but are also the only way to make them possible.

An EFT can be constructed essentially in 4 steps. Consider for example a process involving only scales that are much smaller than a heavy particle with mass M . An EFT integrating out the heavy particle can then be constructed in the following way:

1) *Identify all relevant scales of the problem*, find the expansion parameter, and choose appropriate fields for the EFT.

In our example there are two scales: a low scale at which the process happens, and the high scale of the mass M . The expansion parameter is therefore $1/M$ and the fields of the EFT do not include the heavy particle field, but are otherwise the same as in the full theory.

2) *Construct the Lagrangian \mathcal{L}_{eff}* of the effective theory by writing down all terms allowed by the symmetries of the problem up to some order in the expansion parameter. Theoretically, \mathcal{L}_{eff} includes an infinite number of operators, but the lowest order terms in the expansion parameter are sufficient to get a certain accuracy. For higher precision, more terms can always be included.

3) *Determine the coefficients in \mathcal{L}_{eff}* (called Wilson coefficients). This can be achieved by computing matrix elements in the effective and full theory. Since the EFT amplitude \mathcal{M}_{eff} has to be the same as the full theory amplitude $\mathcal{M}_{\text{full}}$ expanded in the expansion parameter, the coefficients are

found by equating the matrix elements.

4) *Renormalize* \mathcal{L}_{eff} and calculate the renormalization group (RG) running of the Wilson coefficients. The effective theory will generally have more UV divergences than the full theory and therefore more running coefficients. Using their RG evolution, the large logarithms of the full theory (see Equation (3.33)) are resummed into the Wilson coefficients to all orders.

3.2.1 Example: b-Quark Decay

Let's see how this procedure works using the example of a bottom quark decaying into a charm, down, and anti-up quark [24, 25]

$$b \rightarrow c \bar{u} d . \quad (3.35)$$

For step 1 all the relevant scales of the problem need to be determined. The quark 4-momenta and the bottom quark mass m_b are all of order $\mathcal{O}(1 \text{ GeV})$. The W boson, on the other hand, introduces with its mass the scale $m_W = 80 \text{ GeV} \gg m_b$. Since the momenta are of $\mathcal{O}(1 \text{ GeV})$, the W boson will be far off-shell and can be taken out (or "integrated out"¹) of the theory. The effective theory will then include the same fields as the SM except of the W boson (and the Z boson and top quark, but these particles do not occur at the order we are working at). The expansion parameter is easily identified as $1/m_W$.

In step 2 the effective Lagrangian \mathcal{L}_{eff} is constructed. This can be done using one of two approaches. The first approach consists in writing down all possible terms that are allowed by the symmetries of the problem up to a certain order in $1/m_W$, $\alpha_W = g_W^2/4\pi$ and α_s .

For the second approach, the matrix elements are calculated in the full theory, expanded in $1/m_W$, and a term $\Delta\mathcal{L}_{\text{eff}}$ in the Lagrangian is constructed, which reproduces the expanded matrix elements.

The first approach is more general and can also be applied when the full theory is not known (e.g. when constructing an EFT of the Standard Model). In practice, however, it is often more useful to apply the second approach. We will use the second approach now for the example of b quark decay and also in Section 3.3 to construct the vNRQCD Lagrangian.

At tree level, the decay is mediated by the W boson, see Figure 3.2a. It gives the contribution

$$i\mathcal{M}_{\text{full}}^{\text{tree}} = \left(\frac{g_W^2}{2} \right) V_{cb} V_{ud}^* \frac{i}{(p_b - p_c)^2 - m_W^2} \left[\bar{u}_{p_c}^\alpha \gamma_\mu P_L u_{p_b, \alpha} \right] \left[\bar{u}_{p_u}^\beta \gamma^\mu P_L v_{p_d, \beta} \right] , \quad (3.36)$$

where p_b, p_c, p_d, p_u are the momenta of the b, c, d , and \bar{u} quark, respectively. $P_L = (1 - \gamma_5)/2$ is the projection operator for left-handed states, g_W the weak coupling constant, V_{cb} and V_{ud}^* the CKM matrix elements, and u, v the Dirac spinors. α and β denote the color of the quarks, spinor

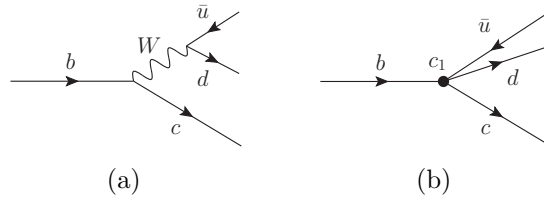


Figure 3.2: b -quark into $c \bar{u} d$ at tree level in the full theory (a) and in the effective theory (b).

¹expression coming from the path integral formulation of EFTs, where the field is taken out of the Lagrangian by integrating over it in the path integral. See e.g. [24]

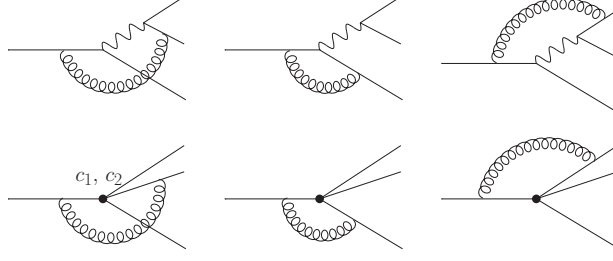


Figure 3.3: One-loop QCD corrections to b-quark decay in the full theory (upper row) and in the effective theory (lower row).

indices are suppressed.

Since $p_i \ll m_W$, the boson propagator can be expanded in $1/m_W^2$:

$$i\mathcal{M}_{\text{eff}}^{\text{tree}} = -i \frac{4G_F}{\sqrt{2}} V_{cb} V_{ud}^* \left[\bar{u}_{p_c}^\alpha \gamma_\mu P_L u_{p_b, \alpha} \right] \left[\bar{u}_{p_u}^\beta \gamma^\mu P_L v_{p_d, \beta} \right], \quad (3.37)$$

where $G_F/\sqrt{2} = g_W^2/8m_W^2$ is the Fermi constant. Equation (3.37) is generated in the effective theory from a 4-particle vertex (see Figure 3.2b). At higher orders in α_s we can expect a new color structure to emerge coming from diagrams of the form shown in Figure 3.3. They will introduce a color structure of the form

$$T_{\alpha\beta}^a T_{\rho\sigma}^a = -\frac{1}{2N_c} \delta_{\alpha\beta} \delta_{\rho\sigma} + \frac{1}{2} \delta_{\alpha\sigma} \delta_{\rho\beta} \quad (3.38)$$

and lead to a factor of

$$\Delta\mathcal{M}_{\text{eff}}^{1\text{-loop}} \propto \left[\bar{u}_{p_c}^\alpha \gamma_\mu P_L u_{p_b, \beta} \right] \left[\bar{u}_{p_u}^\beta \gamma^\mu P_L v_{p_d, \alpha} \right] \quad (3.39)$$

in the corresponding amplitude. Reconstructing a Lagrangian that generates the structures in both Equation (3.37) and (3.39), one obtains:

$$\Delta\mathcal{L}_{\text{eff}} = -\frac{4G_F}{\sqrt{2}} V_{cb} V_{ud}^* (c_1 \mathcal{O}_1 + c_2 \mathcal{O}_2), \quad (3.40)$$

where c_1 and c_2 are Wilson coefficients and the operators $\mathcal{O}_1, \mathcal{O}_2$ read

$$\begin{aligned} \mathcal{O}_1 &= \left[\bar{c}^\alpha \gamma_\mu P_L b_\alpha \right] \left[\bar{u}^\beta \gamma^\mu P_L d_\beta \right] \\ \mathcal{O}_2 &= \left[\bar{c}^\alpha \gamma_\mu P_L b_\beta \right] \left[\bar{u}^\beta \gamma^\mu P_L d_\alpha \right]. \end{aligned} \quad (3.41)$$

Equation (3.40) achieves a factorization into short- and long-distance physics. The Wilson coefficients encode the short-distance physics originating from the W-boson, whereas the operators $\mathcal{O}_1, \mathcal{O}_2$ encode the long-distance physics. Note that in the effective Lagrangian \mathcal{L}_{eff} only the terms containing interactions with the W boson are modified in the form of Equation (3.37). The terms for all other particles are the same as in the Standard Model.

Having derived the Lagrangian \mathcal{L}_{eff} , we can now go to step 3 and determine the Wilson coefficients of \mathcal{L}_{eff} . For this we compare matrix elements in the effective theory with the full theory result expanded in $1/m_W$:

$$i\mathcal{M}_{\text{eff}} = i\mathcal{M}_{\text{full}}^{\text{expanded}}. \quad (3.42)$$

At tree level, we already calculated the amplitude. Comparing the expanded amplitude in the full theory (Equation (3.37)) with the vertex generated from the effective Lagrangian (Equation (3.40)), we find $c_1 = 1$.

At one-loop, the QCD corrections shown in Figure 3.3 contribute. We can simplify the calculations for the matching by assuming that the quark masses are zero and using the same external momenta $-p^2 \sim m_b$ for all external states. The IR divergences are then regulated by $-p^2$.

Note that the external momenta are off-shell. However, this does not affect the determination of the Wilson coefficients, because they encode long-distance physics and do not depend on the quark masses or external momenta.

The full amplitude, including wave-function renormalization, gives [24]

$$i\mathcal{M}_{\text{full}}^{1\text{-loop}} = -i \frac{4G_F}{\sqrt{2}} V_{cb} V_{ud}^* \left\{ D_1 \left[1 + \frac{\alpha_s}{4\pi} 2C_F + \log\left(\frac{\mu^2}{-p^2}\right) + \frac{3}{N_c} \frac{\alpha_s}{4\pi} \log\left(\frac{m_W^2}{-p^2}\right) \right] \right. \\ \left. - D_2 \left[3 \frac{\alpha_s}{4\pi} \log\left(\frac{m_W^2}{-p^2}\right) \right] \right\}, \quad (3.43)$$

where D_1, D_2 encode the external Dirac spinors

$$D_1 = [\bar{u}_p^\alpha \gamma_\mu P_L u_{p,\alpha}] [\bar{u}_p^\beta \gamma^\mu P_L v_{p,\beta}] \\ D_2 = [\bar{u}_p^\alpha \gamma_\mu P_L u_{p,\beta}] [\bar{u}_p^\beta \gamma^\mu P_L v_{p,\alpha}] \quad (3.44)$$

and differ only in their color structure, which is induced by the color matrices (Equation (3.38)).

In the effective theory, the diagrams with vertices from the operators \mathcal{O}_1 and \mathcal{O}_2 , respectively, give

$$i\mathcal{M}_{\text{eff}}^{\mathcal{O}_1} = \frac{4G_F}{\sqrt{2}} V_{cb} V_{ud}^* c_1^0 \left\{ D_1 \left[1 + \frac{\alpha_s}{4\pi} 2C_F \log\left(\frac{\mu^2}{-p^2}\right) + \frac{3}{N_c} \frac{\alpha_s}{4\pi} \left(\frac{1}{\varepsilon} + \log\left(\frac{\mu^2}{-p^2}\right) \right) \right] \right. \\ \left. - D_2 \left[3 \frac{\alpha_s}{4\pi} \left(\frac{1}{\varepsilon} + \log\left(\frac{\mu^2}{-p^2}\right) \right) \right] \right\} \\ i\mathcal{M}_{\text{eff}}^{\mathcal{O}_2} = \frac{4G_F}{\sqrt{2}} V_{cb} V_{ud}^* c_2^0 \left\{ D_2 \left[1 + \frac{\alpha_s}{4\pi} 2C_F \log\left(\frac{\mu^2}{-p^2}\right) + \frac{3}{N_c} \frac{\alpha_s}{4\pi} \left(\frac{1}{\varepsilon} + \log\left(\frac{\mu^2}{-p^2}\right) \right) \right] \right. \\ \left. - D_1 \left[3 \frac{\alpha_s}{4\pi} \left(\frac{1}{\varepsilon} + \log\left(\frac{\mu^2}{-p^2}\right) \right) \right] \right\}, \quad (3.45)$$

where c_1^0 and c_2^0 are the bare Wilson coefficients and the wave function renormalization has already been included. In contrast to Equation (3.43), the amplitude has leftover divergences, which appear because m_W is effectively taken to infinity in the effective theory. The divergences can be absorbed into the Wilson coefficients. The renormalized coefficients c_1 and c_2 are then related to the bare coefficients by

$$\begin{pmatrix} c_1^0 \\ c_2^0 \end{pmatrix} = Z_c \begin{pmatrix} c_1 \\ c_2 \end{pmatrix} \quad \text{with} \quad Z_c = \mathbb{1} + \delta Z_c = \mathbb{1} + \frac{\alpha_s}{4\pi\varepsilon} \begin{pmatrix} -1 & 3 \\ 3 & -1 \end{pmatrix} + \mathcal{O}(\alpha_s^2), \quad (3.46)$$

where δZ_c can be read off from Equation (3.45). Using c_1 and c_2 , the amplitudes are free of divergences:

$$\begin{aligned}
i\mathcal{M}_{\text{eff}}^{\mathcal{O}_1} &= \frac{4G_F}{\sqrt{2}} V_{cb} V_{ud}^* c_1 \left\{ D_1 \left[1 + \frac{\alpha_s}{4\pi} 2C_F \log\left(\frac{\mu^2}{-p^2}\right) + \frac{3}{N_c} \frac{\alpha_s}{4\pi} \log\left(\frac{\mu^2}{-p^2}\right) \right] \right. \\
&\quad \left. - D_2 \left[\begin{array}{c} 3 \frac{\alpha_s}{4\pi} \log\left(\frac{\mu^2}{-p^2}\right) \end{array} \right] \right\} \\
i\mathcal{M}_{\text{eff}}^{\mathcal{O}_2} &= \frac{4G_F}{\sqrt{2}} V_{cb} V_{ud}^* c_2 \left\{ D_2 \left[1 + \frac{\alpha_s}{4\pi} 2C_F \log\left(\frac{\mu^2}{-p^2}\right) + \frac{3}{N_c} \frac{\alpha_s}{4\pi} \log\left(\frac{\mu^2}{-p^2}\right) \right] \right. \\
&\quad \left. - D_1 \left[\begin{array}{c} 3 \frac{\alpha_s}{4\pi} \log\left(\frac{\mu^2}{-p^2}\right) \end{array} \right] \right\}. \tag{3.47}
\end{aligned}$$

Comparing the effective amplitude Equation (3.47) with the expanded full theory amplitude Equation (3.43), the Wilson coefficients are found to be

$$\begin{aligned}
c_1(\mu) &= 1 + \frac{3}{N_c} \frac{\alpha_s}{4\pi} \log\left(\frac{m_W^2}{\mu^2}\right) \\
c_2(\mu) &= -3 \frac{\alpha_s}{4\pi} \log\left(\frac{m_W^2}{\mu^2}\right). \tag{3.48}
\end{aligned}$$

Three important observations can be made from these equations:

1) *Wilson coefficients*: The appearance of the α_s terms in Equation (3.48) can be understood with the method of regions. In the effective theory, every W boson propagator is effectively replaced by $i/(p^2 - m_W^2) \rightarrow (-i/m_W^2)$.

At tree level this is valid, since $p \ll m_W$, but in loop diagrams such as Figure 3.3, p is an integration variable and therefore also takes on values with $p \gg m_W$. The integrand can still be expanded, but the integral has to be split into two parts with the method of regions. This can be done with a cutoff Λ fulfilling $m_W \gg \Lambda \gg m_b$.

The one-loop diagrams from Figure 3.3 then schematically take the form (considering only the radial part of p)

$$\begin{aligned}
\alpha_s \int_0^\infty dp \frac{i}{[p^2 - m_W^2]_+} f(p) &= \alpha_s \left(\int_0^\Lambda dp + \int_\Lambda^\infty dp \right) \frac{i}{[p^2 - m_W^2]_+} f(p) \\
&\simeq \alpha_s \frac{-i}{m_W^2} \int_0^\Lambda dp f(p) + \alpha_s \int_\Lambda^\infty dp \frac{i}{p^2} f(p). \tag{3.49}
\end{aligned}$$

The first integral describes the long distance physics coming from small momenta and is the same integral we would get from using \mathcal{L}_{eff} . The second integral describes the short-distance physics and appears as the α_s term in the Wilson coefficients c_1 and c_2 (Equation (3.48)). In practice, dimensional regularization is used instead of a cutoff, but the principle stays the same.

2) *Large logarithms*: Looking at Equation (3.43) the problem of large logarithms becomes apparent: with $\alpha_s \sim 0.2$ and $-p^2 \sim m_b \sim 4 \text{ GeV}$ the logarithms become large: $\log(m_W^2/-p^2) \sim 6$. The one-loop correction is then of order $\alpha_s \log(m_W^2/-p^2) \sim 1$ and therefore as large as the tree level term! This pattern continues at higher loop orders where terms of the form $(\alpha_s \log(m_W^2/-p^2))^i \sim 1$ appear to all orders in α_s . The perturbative expansion in α_s of the full theory is hence rendered

meaningless.

The effective theory solves the problem of large logarithms by splitting them into two parts:

$$\left[1 + \alpha_s \log \left(\frac{m_W^2}{-p^2} \right)\right] = \left[1 + \alpha_s \log \left(\frac{m_W^2}{\mu^2} \right)\right] \cdot \left[1 + \alpha_s \log \left(\frac{\mu^2}{-p^2} \right)\right]. \quad (3.50)$$

The first logarithm on the right hand side goes into the Wilson coefficients (Equation (3.48)) and the second one into the matrix element (Equation (3.47)). Choosing $\mu \sim m_b$ renders the second logarithm harmless. However, μ has to be set to the same value everywhere and would therefore make the first logarithm large. In the EFT, this problem is solved by the Wilson coefficients. They have an RG running, which reproduces the first logarithm in Equation (3.48), and additionally sums logarithms of the form $(\alpha_s \log(m_W^2/\mu^2))^i$ to all orders in α_s , as we will see in step 4.

3) *Scale choice in the matching*: In the matching (Equation (3.42)) terms containing $\log(\mu/-p^2)$ terms cancel, because the theories have to agree in the IR. The $\log(\mu^2/m_W^2)$ terms remain and to render them small we have to choose $\mu \sim m_W$ in the matching.

In the last step we performed the matching and determined the coefficients $c_1(\mu)$ and $c_2(\mu)$ for scales $\mu \sim m_W$. To get the Wilson coefficients for arbitrary scales μ we now have to calculate their RG running. The renormalized Wilson coefficients c_1, c_2 are related to the bare coefficients by Equation (3.46). Note that c_1 contributes to the renormalization of c_2 and vice versa, a feature often encountered in EFTs and called mixing. To calculate the running it is convenient to change to a basis where Z_c is diagonalized. Using $\mathcal{U} = \mathcal{U}^\dagger = \frac{1}{\sqrt{2}} \begin{pmatrix} 1 & 1 \\ 1 & -1 \end{pmatrix}$ the diagonalized matrix becomes

$$\mathcal{U}^\dagger Z_c \mathcal{U} = \mathbb{1} + \frac{1}{\varepsilon} \frac{\alpha_s}{4\pi} \begin{pmatrix} 2 & 0 \\ 0 & -4 \end{pmatrix} = \begin{pmatrix} Z_+ & 0 \\ 0 & Z_- \end{pmatrix} \quad (3.51)$$

and the Lagrangian takes the form

$$\begin{aligned} \delta \mathcal{L}_{\text{eff}} &= (c_1 \quad c_2) \mathcal{U} \mathcal{U}^\dagger Z_c \mathcal{U} \mathcal{U}^\dagger \begin{pmatrix} \mathcal{O}_1 \\ \mathcal{O}_2 \end{pmatrix} = c_+ Z_+ \mathcal{O}_+ + c_- Z_- \mathcal{O}_- \\ &= c_+^0 \mathcal{O}_+ + c_-^0 \mathcal{O}_-, \end{aligned} \quad (3.52)$$

where $c_\pm = c_1 \pm c_2$, $\mathcal{O}_\pm = \frac{1}{2}(\mathcal{O}_1 \pm \mathcal{O}_2)$, and $Z_\pm = 1 + \delta Z_\pm$.

The bare coefficients c_\pm^0 are independent of the renormalization scale μ :

$$\begin{aligned} \mu \frac{d}{d\mu} c_+^0 &= \mu \frac{d}{d\mu} [c_+ (1 + \delta Z_+)] \\ &= Z_+ \left(\mu \frac{d}{d\mu} c_+ \right) + c_+ \left(\mu \frac{d}{d\mu} \delta Z_+ \right) \stackrel{!}{=} 0. \end{aligned} \quad (3.53)$$

Rearranging gives the renormalization group (RG) equation for c_+ :

$$\begin{aligned} \mu \frac{d}{d\mu} c_+ &= - \left(Z_+^{-1} \mu \frac{d}{d\mu} \delta Z_+ \right) c_+ \\ &= \gamma_+ c_+, \end{aligned} \quad (3.54)$$

where γ_+ is the anomalous dimension of c_+ and the calculation for c_- is analogous. The anomalous

dimension can be written in the form

$$\gamma_{\pm} = \sum_{i=1}^{\infty} \left(\frac{\alpha_s}{4\pi} \right)^i \gamma_{\pm}^{(i)}. \quad (3.55)$$

Using the RG Equation (3.54) for α_s , the one-loop anomalous dimension evaluates to $\gamma_+^{(1)} = 4$ and $\gamma_-^{(1)} = -8$.

Solving Equation (3.54) for c_{\pm} finally gives the μ dependence of the Wilson coefficients

$$c_{\pm}(\mu_1) = c_{\pm}(\mu_0) \left(\frac{\alpha_s(\mu_1)}{\alpha_s(\mu_0)} \right)^{\gamma_{\pm}^{(1)}/2\beta_0}, \quad (3.56)$$

where β_0 is the first coefficient of the β -function for α_s . Equation (3.56) achieves a resummation of terms of the form $\alpha_s \log(\mu_0/\mu_1)^i$ to all orders, as can be seen from its expansion in α_s :

$$c_+(\mu_1) = c_+(\mu_0) \left(1 - \left[\alpha_s(\mu_0) \log \left(\frac{\mu_1}{\mu_0} \right) \right] \frac{\gamma_+^{(1)}}{4\pi} + \left[\alpha_s(\mu_0) \log \left(\frac{\mu_1}{\mu_0} \right) \right]^2 \frac{\gamma_+^{(1)}}{16\pi^2} (\beta_0 + 2\gamma_+^{(1)}) + \dots \right). \quad (3.57)$$

The problem of the large logarithms is now solved in the following way: $c_{\pm}(\mu)$ can be determined from matching at the scale $\mu = m_W$, where the logarithms are small (Equation (3.48)). Using Equation (3.56), the coefficients c_{\pm} are evolved to the scale $\mu^2 = -p^2$, summing large logarithms of the form $\log(\frac{\mu^2}{m_W^2})$ to all orders in the process. Finally, the matrix element from Equation (3.47) is evaluated at $\mu = -p^2$, which renders the remaining logarithms in the matrix element small.

In Equation (3.56) we used the first coefficient of $\gamma_{\pm}^{(1)}$. Amplitudes calculated with this leading order running of c_{\pm} give the leading logarithm (LL) approximation. Using higher order matching and running, we would obtain the next-to-leading-logarithm (NLL), next-to-next-to-leading-logarithm (NNLL) approximation, and so on.

Note that the LL calculation needed the tree-level matching with one-loop running (i.e. at tree level we needed the full amplitudes and at one-loop only the divergent parts). This principle applies generally, such that for the N^i LL approximation one needs to match at i -loops and calculate the running at $(i+1)$ loops.

3.3 Introduction to vNRQCD

3.3.1 NRQCD, pNRQCD, and vNRQCD

The description of non-relativistic bound states has a long history. Already in 1951 Bethe and Salpeter [26], and Schwinger [27] formulated an equation to describe bound state systems in quantum field theory, now known as the Bethe-Salpeter equation. While it correctly resummed terms of the Coulomb singularity (see section 3.4.3), it still used relativistic fields to describe a non-relativistic system and high-precision calculations proved to be difficult.

The first formulation using only the non-relativistic degrees of freedom appeared in 1985 in the form of the effective field theory NRQED (non-relativistic QED) [28]. It was followed in 1995 by its QCD equivalent NRQCD (non-relativistic QCD) [29].

NRQCD describes heavy quarkonium systems at low velocities and factorizes the amplitude of a process into Wilson coefficients c_i , which contain physics at scales of the heavy quark mass m and higher, and long-distance matrix elements $\langle \mathcal{O}_i \rangle$, which contain the physics at the non-relativistic

scales $\mathbf{p} \sim mv$ and $E \sim mv^2$:

$$\mathcal{A} = \sum_i c_i \langle \mathcal{O}_i \rangle . \quad (3.58)$$

The Wilson coefficients can be calculated in perturbation theory only if the mass of the system is larger than the hadronization scale, i.e. $m \gg \Lambda_{\text{QCD}} \sim 200 \text{ MeV}$. With $m_c \sim 1 \text{ GeV}$, $m_b \sim 4 \text{ GeV}$, and $m_t \sim 173 \text{ GeV}$, the charmonium $c\bar{c}$, bottomium $b\bar{b}$ and (fictitious) toponium $t\bar{t}$ fulfill this condition.

The matrix element, on the other hand, can only be calculated in perturbation theory, if also the non-relativistic scales $E \sim mv^2$ and $\mathbf{p} \sim mv$ are larger than Λ_{QCD} . This exclusively applies to the $t\bar{t}$ system, because for $b\bar{b}$ and $c\bar{c}$ non-perturbative effects can come into play.

For the matrix element further complications arise, because NRQCD does not distinguish the scales $\mathbf{p} \sim mv$ and $E \sim mv^2$, and therefore its Lagrangian has no clear power counting in the velocity v . Additionally, it is not suited for dimensional regularization and uses a cutoff instead, which makes calculations difficult.

For $c\bar{c}$ and $b\bar{b}$, the problems of power counting and non-perturbative effects can both be solved by extracting the matrix element from experiment or lattice calculations [30]. The Wilson coefficient does not depend on v , therefore has no problems with power counting, and is calculated in perturbation theory.

NRQCD in this form is widely used today for the description of heavy quarkonium production, decay, and spectroscopy.

For perturbative calculations of the matrix element, two theories were developed to achieve a separation of the scales mv and mv^2 : velocity NRQCD (vNRQCD) and potential NRQCD (pNRQCD). vNRQCD [21] was developed for theories with $mv \gg mv^2 \gg \Lambda_{\text{QCD}}$ and is relevant for $t\bar{t}$ production ($m_t \sim 173 \text{ GeV}$, $v_t \sim 0.15$). It matches to QCD at the scale $\mu = m_t$ and includes the degrees of freedom mv and mv^2 simultaneously.

pNRQCD is constructed in two stages. First, NRQCD is matched to QCD at $\mu = m_t$ and run down to $\mu \sim mv$. Then NRQCD is matched to pNRQCD, integrating out degrees of freedom of the scale mv . It can be used also for calculations where $m \gg mv \gg mv^2 \sim \Lambda_{\text{QCD}}$.

A comprehensive review for the application of NRQCD, lattice NRQCD, and pNRQCD for heavy quark bound states can be found in [30] [31].

For this work we use vNRQCD, which allows a consistent resummation of large logarithms of the form $(\alpha_s \log(v))^i$. Work on power counting and separation of the scales mv and mv^2 [32–36], led to the formulation of vNRQCD in 1999 [21]. A series of papers followed calculating the one-loop matching [37], the running of the potentials [38–40], and the running of the heavy quarkonium production current [41]. Subtleties concerning the ultrasoft renormalization were addressed in [41–45], which lead to small changes in some of the potentials. The application of vNRQCD for $t\bar{t}$ production at threshold was formulated in [11, 46, 47].

An introduction to vNRQCD can also be found in [44, 48], and a comprehensive review in [49].

3.3.2 vNRQCD Lagrangian

To construct the effective Lagrangian $\mathcal{L}_{\text{vNRQCD}}$, we first identify the scales and expansion parameter of the problem, and find appropriate fields. The scales are the quark mass m , the momentum $\mathbf{p} \sim mv$, and the energy $E \sim mv^2$. The expansion parameter is v , which is the velocity of either the quark or the anti-quark in the CM frame.

For the fields we can use the findings from the method of regions (Section 3.1). We identified four regions contributing to processes with small velocity: hard, potential, soft, and ultrasoft. Accord-

ingly, we can split up the quark and gluon fields into hard, potential, soft, and ultrasoft modes. We can immediatly integrate out the hard modes, because they have $k^0 \sim k \sim m$ and are much larger than the scales of the problem.

Similar to b quark decay in Section 3.2.1, only the modes that can become real, on-shell particles are kept in the EFT. For heavy quarkonia the soft heavy quarks as well as the potential gluons, potential light quarks and potential ghosts are always off-shell and therefore integrated out. This leaves the following fields for vNRQCD:

$$\begin{aligned}
&\underline{\text{potential}} \text{ heavy quarks} && (E \sim mv^2, \mathbf{p} \sim mv) \\
&\underline{\text{soft}} \text{ gluons, light quarks, and ghosts} && (E \sim mv, \mathbf{p} \sim mv) \\
&\underline{\text{ultrasoft}} \text{ gluons, light quarks, and ghosts} && (E \sim mv^2, \mathbf{p} \sim mv^2) .
\end{aligned} \tag{3.59}$$

Note that we assume only the heavy quark to have a mass, all other particles are massless. The vNRQCD Lagrangian has a kinetic part \mathcal{L}_{kin} and an interaction part \mathcal{L}_{int} . Both can be further divided into a potential, soft and ultrasoft piece:

$$\begin{aligned}
\mathcal{L}_{\text{vNRQCD}} &= \mathcal{L}_{\text{kin}} + \mathcal{L}_{\text{int}} \\
&= \mathcal{L}_{\text{kin}}^{\text{p}} + \mathcal{L}_{\text{kin}}^{\text{s}} + \mathcal{L}_{\text{kin}}^{\text{us}} + \mathcal{L}_{\text{int}}^{\text{p}} + \mathcal{L}_{\text{int}}^{\text{s}} + \mathcal{L}_{\text{int}}^{\text{us}} .
\end{aligned} \tag{3.60}$$

We will now find the explicit form of the fields from Equation (3.59) and then construct the pieces of the Lagrangian in Equation (3.60).

Fields

The heavy quark and anti-quark fields can be derived from the QCD field

$$\psi_{\text{full}}(x) = \sum_{\lambda} \int \frac{d^3p}{(2\pi)^3} \left(a_{\mathbf{p}}^{\lambda} u_{\mathbf{p}}^{\lambda} e^{-ipx} + (b_{\mathbf{p}}^{\lambda})^{\dagger} v_{\mathbf{p}}^{\lambda} e^{ipx} \right) , \tag{3.61}$$

where $E_{\text{rel}} = \sqrt{\mathbf{p}^2 + m^2}$ and the spinors in the Dirac basis are

$$u_{\mathbf{p}}^{\lambda} = \sqrt{\frac{E_{\text{rel}} + m}{2E_{\text{rel}}}} \begin{pmatrix} \zeta_{\lambda} \\ \frac{\boldsymbol{\sigma} \cdot \mathbf{p}}{E_{\text{rel}} + m} \zeta_{\lambda} \end{pmatrix}, \quad v_{\mathbf{p}}^{\lambda} = \sqrt{\frac{E_{\text{rel}} + m}{2E_{\text{rel}}}} \begin{pmatrix} \frac{\boldsymbol{\sigma} \cdot \mathbf{p}}{E_{\text{rel}} + m} (i\sigma_2 \xi_{\lambda}^*) \\ (i\sigma_2 \xi_{\lambda}^*) \end{pmatrix}. \tag{3.62}$$

$\psi_{\text{full}}(x)$ describes both particles and anti-particles. It can annihilate particles with $a_{\mathbf{p}}^{\lambda}$ and create anti-particles with $(b_{\mathbf{p}}^{\lambda})^{\dagger}$.

In the non-relativistic limit, the heavy quark and anti-quark can neither annihilate each other nor be produced in loops, since this would introduce a scale much larger than mv and mv^2 . Therefore they are independent and can be described with separate fields in the vNRQCD Lagrangian.

Additionally, the spinors $u_{\mathbf{p}}^{\lambda}$ and $v_{\mathbf{p}}^{\lambda}$ get a large upper and lower component, respectively, for $\mathbf{p} \sim mv \ll m$. Instead of 4-momentum spinors one can therefore switch to the simpler 2-component spinors:

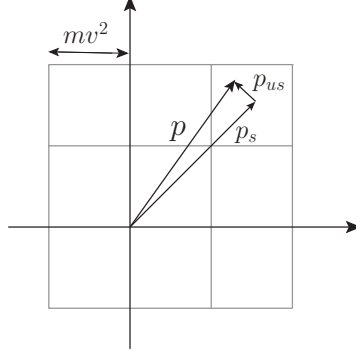


Figure 3.4: Every momentum \mathbf{p} can be split into a soft and an ultrasoft part. The soft part \mathbf{p}_s is discrete and points to a box of size mv^2 .

$$\begin{aligned}\psi(x) &= \sum_{\lambda} \int \frac{d^3\mathbf{p}}{(2\pi)^3} a_{\mathbf{p}}^{\lambda} e^{-i(p^0 x^0 - \mathbf{p}\mathbf{x})} \zeta_{\lambda} \\ \chi(x) &= \sum_{\lambda} \int \frac{d^3\mathbf{p}}{(2\pi)^3} b_{\mathbf{p}}^{\lambda} e^{-i(p^0 x^0 - \mathbf{p}\mathbf{x})} (i\sigma_2 \xi_{\lambda}^*),\end{aligned}\tag{3.63}$$

where $p^0 = m + mv^2 + \mathcal{O}(v^4) = m + E_{\text{nr}} + \mathcal{O}(v^4)$ in the non-relativistic limit. e^{-imt} describes relativistic fluctuations at the scale $m \gg mv$ and will be taken out of the final expression for the quark field. Without e^{-imt} , the quark field will only contain fluctuations at the scales mv and mv^2 .

In order to have a consistent power counting in the Lagrangian, we need a way to distinguish the mv and mv^2 modes. This can be achieved by splitting the momentum \mathbf{p} into an ultrasoft part $\mathbf{p}_{us} \sim mv^2$ and a soft part $\mathbf{p}_s \sim mv$:

$$\mathbf{p} = \mathbf{p}_s + \mathbf{p}_{us} .\tag{3.64}$$

Since $\mathbf{p}_s \ll \mathbf{p}_{us}$, the soft momentum \mathbf{p}_s can be viewed discretely, while the ultrasoft momentum is continuous (see Figure 3.4). The integral over \mathbf{p} is then decomposed into a sum over the soft label-momenta \mathbf{p}_s and an integral over \mathbf{p}_{us} :

$$\int d\mathbf{p} \rightarrow \sum_{\mathbf{p}_s} \int d\mathbf{p}_{us} .\tag{3.65}$$

Plugging this integral into Equation (3.63), one gets:

$$\begin{aligned}\psi(x) &= \sum_{\lambda} \sum_{\mathbf{p}_s} \int \frac{d^3\mathbf{p}_{us}}{(2\pi)^3} a_{\mathbf{p}}^{\lambda} e^{-imt} e^{-iE_{\text{nr}}t} e^{i(\mathbf{p}_s + \mathbf{p}_{us})\mathbf{x}} \zeta_{\lambda} \\ &= e^{-imt} \sum_{\mathbf{p}_s} e^{i\mathbf{p}_s\mathbf{x}} \psi_{\mathbf{p}_s}(x)\end{aligned}\tag{3.66}$$

with

$$\psi_{\mathbf{p}_s}(x) = \sum_{\lambda} \int \frac{d^3\mathbf{p}_{us}}{(2\pi)^3} a_{\mathbf{p}}^{\lambda} e^{i\mathbf{p}_{us}\mathbf{x}} e^{-iE_{\text{nr}}t} \zeta_{\lambda} .\tag{3.67}$$

The quark field $\psi_{\mathbf{p}_s}$ now contains only the long-distance fluctuations from \mathbf{p}_{us} and any derivative acting on it will give a factor of $mv^2 \sim \mathbf{p}_{us}$: $-i \partial \psi_{\mathbf{p}_s} = \mathbf{p}_{us} \psi_{\mathbf{p}_s}$. The momentum \mathbf{p}_s of $\psi_{\mathbf{p}_s}$ is called label momentum.

The heavy anti-quark field $\chi_{\mathbf{p}_s}$ is constructed in the same way. Also for the soft gluon field $A_q^\mu(x)$, the soft and ultrasoft momenta need to be separated

$$A^\mu(x) = \sum_q e^{-iqx} A_q^\mu(x) . \quad (3.68)$$

Note that the sum goes over all four momentum components, while in Equation (3.66) it included only the three momenta. The soft gluon field has $(k_0, \mathbf{k}) \sim (mv, mv)$ and therefore needs the separation in soft and ultrasoft momenta in all four momentum components. In contrast, the heavy quark field scales with $(k_0, \mathbf{k}) \sim (mv^2, mv)$. The k_0 component does not have a soft part and therefore no separation is necessary.

The ultrasoft gluon only has ultrasoft momenta $(k_0, \mathbf{k}) \sim (mv^2, mv^2)$ and is denoted by $A^\mu(x)$, without a soft momentum label.

This method of separating momenta at different scales is called label-formalism. It was originally devised for HQET [50] and is also used in SCET [51].

Kinetic Terms: \mathcal{L}_{kin}

Starting with the kinetic term $\mathcal{L}_{\text{kin}}^p$ for the heavy quark and anti-quark field, we rewrite the 4-spinor field $\psi_{\text{full}}(x)$ from the full theory with the explicit separation into soft and ultrasoft momenta:

$$\psi_{\text{full}}(x) = e^{-imt} \sum_{\mathbf{p}_s} e^{i\mathbf{p}_s \mathbf{x}} \psi_{\text{full}}^+(x) + e^{imt} \sum_{\mathbf{p}_s} e^{-i\mathbf{p}_s \mathbf{x}} \psi_{\text{full}}^-(x) , \quad (3.69)$$

where

$$\begin{aligned} \psi_{\text{full}}^+(x) &= \sum_{\lambda} \int \frac{d^3 \mathbf{p}_{us}}{(2\pi)^3} e^{-iE_{\text{nr}} t} e^{i\mathbf{p}_{us} \mathbf{x}} a_{\mathbf{p}}^{\lambda} u_{\mathbf{p}}^{\lambda} \\ \psi_{\text{full}}^-(x) &= \sum_{\lambda} \int \frac{d^3 \mathbf{p}_{us}}{(2\pi)^3} e^{iE_{\text{nr}} t} e^{-i\mathbf{p}_{us} \mathbf{x}} (b_{\mathbf{p}}^{\lambda})^{\dagger} v_{\mathbf{p}}^{\lambda} \end{aligned} \quad (3.70)$$

and $\mathbf{p} = \mathbf{p}_s + \mathbf{p}_{us}$. Plugging $\psi_{\text{full}}(x)$ into the QCD Lagrangian, one gets:

$$\begin{aligned} \mathcal{L}_{\text{QCD}}^{\text{kin}} &= \bar{\psi}_{\text{full}}(x) (i\partial - m) \psi_{\text{full}}(x) \\ &= \sum_{\mathbf{p}_s} \left[\bar{\psi}_{\text{full}}^+(x) (i\partial - m) \psi_{\text{full}}^+(x) + \bar{\psi}_{\text{full}}^-(x) (i\partial - m) \psi_{\text{full}}^-(x) \right] . \end{aligned} \quad (3.71)$$

The mixed contributions with e^{-2imt} , e^{+2imt} , and $e^{i(\mathbf{p}_s + \mathbf{p}_s') \mathbf{x}}$ vanish, since in the path integral formulation, they would lead to rapid oscillations and thus cancel.

The kinetic term is now separated into a quark and an anti-quark part. Writing out the spinors and Dirac matrices explicitly, and using $E_{\text{nr}} \sim mv^2$, $\mathbf{p}_s \sim mv$, $\mathbf{p}_{us} \sim mv^2$ to expand in v , we obtain the kinetic term for the heavy quark field (the calculation for the anti-quark field goes along the same lines):

$$\begin{aligned}
\bar{\psi}_{\text{full}}^+(x) (i\not{\partial} - m) \psi_{\text{full}}^+(x) &= \\
&= \sum_{\lambda, \lambda'} \int \frac{d^3 \mathbf{p}_{us}}{(2\pi)^3} \frac{d^3 \mathbf{p}'_{us}}{(2\pi)^3} (a_{\mathbf{p}'}^\lambda)^\dagger \left(-\frac{\zeta_{\lambda'}}{E_{\text{rel}} + m} \zeta_{\lambda'} \right)^\dagger (\gamma^0 E_{\text{rel}} - \boldsymbol{\gamma} \mathbf{p} - m) \left(\frac{\zeta_\lambda}{E_{\text{rel}} + m} \zeta_\lambda \right) a_{\mathbf{p}}^\lambda \left(\frac{E_{\text{rel}} + m}{2 E_{\text{rel}}} \right) \\
&= \sum_{\lambda, \lambda'} \int \frac{d^3 \mathbf{p}_{us}}{(2\pi)^3} \frac{d^3 \mathbf{p}'_{us}}{(2\pi)^3} (a_{\mathbf{p}'}^\lambda)^\dagger a_{\mathbf{p}}^\lambda \zeta_\lambda^\dagger \zeta_\lambda \left(E_{\text{nr}} - \frac{(\mathbf{p}_s + \mathbf{p}_{us})^2}{2m} + \frac{\mathbf{p}_s^4}{8m^3} + \mathcal{O}(v^5) \right) \\
&= \psi_{\mathbf{p}_s}^\dagger \left(i\partial_0 - \frac{(\mathbf{p}_s - i\nabla)^2}{2m} + \frac{\mathbf{p}_s^4}{8m^3} + \mathcal{O}(v^5) \right) \psi_{\mathbf{p}_s}, \tag{3.72}
\end{aligned}$$

where $\mathbf{p}' = \mathbf{p}_s + \mathbf{p}_{us}'$. The calculation for the second term of Equation (3.71) is analogous and the kinetic terms for the heavy quark and anti-quark therefore read

$$\mathcal{L}_{\text{kin}}^p = \sum_{\mathbf{p}_s} \psi_{\mathbf{p}_s}^\dagger \left(i\partial_0 - \frac{(\mathbf{p}_s - i\nabla)^2}{2m} + \frac{\mathbf{p}_s^4}{8m^3} + \mathcal{O}(v^5) \right) \psi_{\mathbf{p}_s} + (\psi_{\mathbf{p}_s} \longrightarrow \chi_{\mathbf{p}_s}). \tag{3.73}$$

The form $(\mathbf{p}_s - i\nabla)$ here is no coincidence: When we split the full momentum into a soft and an ultrasoft part, we left the possibility to reparametrize \mathbf{p}_{us} and \mathbf{p}_s by a momentum $\mathbf{q} \sim mv^2$:

$$\mathbf{p} = \mathbf{p}_s + \mathbf{p}_{us} = (\mathbf{p}_s - \mathbf{q}) + (\mathbf{p}_{us} + \mathbf{q}). \tag{3.74}$$

The Lagrangian should therefore be invariant under the change of variable $\mathbf{p}_s \rightarrow \mathbf{p}_s - \mathbf{q}$ and $\mathbf{p}_{us} \rightarrow \mathbf{p}_{us} + \mathbf{q}$. This is only possible, if every soft momentum occurs with an ultrasoft derivative: $(\mathbf{p}_s - i\nabla)$. When we include gauge invariance, this becomes $(\mathbf{p}_s - i\mathbf{D})$. This invariance under the change of variables is called *reparametrization invariance* and appears in a similar form also in HQET and SCET.

In the v -expanded effective Lagrangian (3.73), the lowest order term can easily be identified to be $(i\partial_0 - p^2/2m)$ and gives the Feynman rule for the propagator

$$\longrightarrow \longrightarrow \longrightarrow \frac{i}{p^0 - \mathbf{p}_s^2/2m}. \tag{3.75}$$

Since the kinetic term for the quark and anti-quark fields are exactly the same, also the anti-quark propagator has the form shown in Equation (3.75). The arrows on the propagators always point in the direction of positive energy flow, which leads to different arrows than in QCD. For example the Feynman diagram for the $\mathcal{O}(\alpha_s^0)$ vacuum polarization is

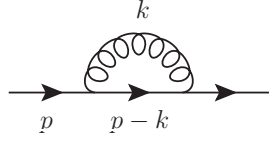
$$\begin{array}{c} \circlearrowleft \\ \circlearrowright \end{array} \quad , \tag{3.76}$$

where the cross denotes an insertion of a production current.

The higher order corrections $\mathbf{p}_s \cdot \nabla$, \mathbf{p}_s^4 , and ∇^2 in Equation (3.73) give insertions on the propagator. For example, an insertion of $\mathbf{p}_s \cdot \nabla$ on a propagator gives

$$\longrightarrow \blacktriangledown \longrightarrow \frac{i}{p^0 - \mathbf{p}_s^2/2m} \left(-i \frac{\mathbf{p}_s \cdot \mathbf{p}_{us}}{m} \right) \frac{i}{p^0 - \mathbf{p}_s^2/2m}. \tag{3.77}$$

Note that in Equation (3.75) the propagator is independent of the ultrasoft three momentum. An ultrasoft loop diagram at lowest order therefore gives



$$= (-ig_{US})^2 C_F \int \frac{d^d k}{(2\pi)^d} \frac{i}{[(p^0 - k^0) - \mathbf{p}^2/2m]_+} \frac{-i}{[k^2]_+}, \quad (3.78)$$

where Feynman gauge was used. The gluon propagator depends on all four components of k^μ , but the quark propagator only involves the k^0 component.

This separation of soft and ultrasoft momenta for the quark propagator could also be achieved by a multipole expansion in the Lagrangian².

Coming next to the kinetic terms $\mathcal{L}_{\text{kin}}^s$ and $\mathcal{L}_{\text{kin}}^{\text{us}}$ of the soft and ultrasoft gluons, we observe that gluons are not affected by the non-relativistic dynamics of the heavy quark. Therefore their kinetic terms are the same as in QCD, just rewritten with the label-formalism:

$$\begin{aligned} \mathcal{L}_{\text{kin}}^s &= -\frac{1}{2} \sum_p \text{Tr} [F_{\mu\nu}^p F^{\mu\nu,p}] \quad , \quad F_{\mu\nu}^p = \left(p_\mu A_\nu^{p,a} - p_\nu A_\mu^{p,a} - g_S f_{bc}^a A_\mu^{p,b} A_\nu^{p,c} \right) T^a \\ \mathcal{L}_{\text{kin}}^{\text{us}} &= -\frac{1}{2} \text{Tr} [G_{\mu\nu} G^{\mu\nu}] \quad , \quad G_{\mu\nu} = \left(\partial_\mu A_\nu^a - \partial_\nu A_\mu^a - g_{US} f_{bc}^a A_\mu^b A_\nu^c \right) T^a \end{aligned} \quad (3.79)$$

where g_S and g_{US} are the soft and ultrasoft coupling constant, respectively.

Ultrasoft Interactions: $\mathcal{L}_{\text{int}}^{\text{us}}$

The ultrasoft gluons interact with each other and with the heavy quark or antiquark, but not with the soft fields, because the ultrasoft modes live at much larger time and length scales than the soft modes. The ultrasoft modes therefore appear frozen with respect to the soft modes and their interactions decouple.

Among each other, the ultrasoft gluons interact in the same way as in QCD, since vNRQCD changes only the structure of the terms involving the heavy quark or antiquark.

The interactions of the ultrasoft gluons with the heavy quark can be determined using gauge invariance. Gauge invariance holds separately for ultrasoft gluons under gauge transformations of length and time scales of $(mv^2)^{-1}$, and for soft gluons under transformations with scales of order $(mv)^{-1}$. Replacing $\partial_\mu \rightarrow \partial_\mu + i\mu_U^\epsilon g_{US} A^\mu$, where $A^\mu = A_a^\mu T^a$, the lowest order interactions of the ultrasoft gluons with the heavy quark and anti-quark field read

$$\sum_{\mathbf{p}_s} -i g_{US} \mu_U^\epsilon (\psi_{\mathbf{p}_s}^\dagger A_0^a T^a \psi_{\mathbf{p}_s} + \chi_{\mathbf{p}_s}^\dagger A_0^a \bar{T}^a \chi_{\mathbf{p}_s}) \quad , \quad (3.80)$$

where the interaction with the anti-quark field $\chi_{\mathbf{p}_s}$ involves the generators $\bar{T}^a = -(T^a)^T$ of the anti-fundamental representation. This replacement can be explained from expanding the interaction term in the QCD Lagrangian. There we have $\bar{\psi}_{\text{full}} T^a \psi_{\text{full}}$, which generates the term $\chi_A T_{AB}^a \chi_B^\dagger$

²instead of using the label formalism, the ultrasoft momentum can be multipole expanded to give $A^\mu(x) = A^\mu(0) + \dots$, which leads to the non-conservation of the ultrasoft momentum in the fermion-gluon vertex (see e.g. [52]). Hence the name "multipole expansion".

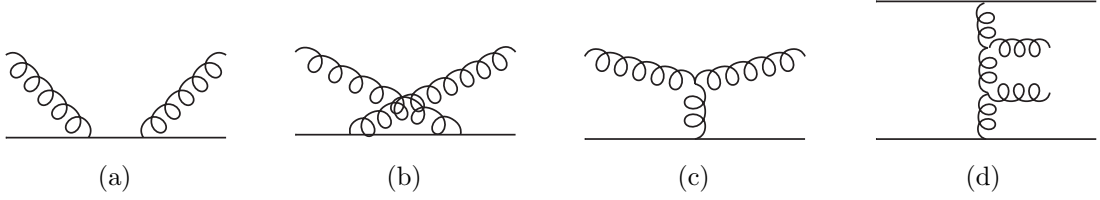


Figure 3.5: QCD diagrams generating soft-potential vertices in the effective theory.

in the effective theory, where A and B are the color indices. To obtain the same form as in Equation (3.80), the fermion fields have to be exchanged, which gives $-\chi_B^\dagger T_{AB}^a \chi_A = \chi^\dagger \bar{T}^a \chi$.

The factor μ_U^ϵ in Equation (3.80) follows from power counting. The measure in dimensional regularization scales with $(mv^2)^{-4+2\epsilon}$ for ultrasoft terms and the derivative ∂_μ scales with mv^2 . Since the action should not depend on the regulator, we can see from Equation (3.79) that A^μ has to scale with $(mv^2)^{1-\epsilon}$. Consequently, $\psi^\dagger A^\mu \psi$ has an additional factor $(mv^2)^{-\epsilon}$ compared to $\psi^\dagger \partial^\mu \psi$. Multiplying with $\mu_U^\epsilon \sim (mv^2)^\epsilon$ then removes the factor and makes the action independent of ϵ .

Altogether, the Lagrangian for interactions of ultrasoft gluons in d dimensions reads

$$\mathcal{L}_{\text{int}}^{\text{us}} = \sum_{\mathbf{p}_s} \left[\psi_{\mathbf{p}_s}^\dagger \left(i D^0 - \frac{(\mathbf{p}_s - i \mathbf{D})^2}{2m} \right) \psi_{\mathbf{p}_s} + (\psi_{\mathbf{p}_s} \rightarrow \chi_{\mathbf{p}_s}, T^a \rightarrow \bar{T}^a) \right] + (\text{interactions involving only ultrasoft particles}) . \quad (3.81)$$

Soft Interactions: $\mathcal{L}_{\text{int}}^s$

In analogy to the ultrasoft interactions, the soft gluons can interact only with each other and the heavy (anti-)quark.

The interactions among the soft particles have again the same structure as in QCD. The structure of the interactions with the heavy quark, however, is different in the soft sector. Since the heavy quark scales with $(E, \mathbf{p}) \sim (mv^2, mv)$, an interaction with a soft gluon with $(E, \mathbf{p}) \sim (mv, mv)$ would throw it off-shell by an amount of mv . Therefore interactions with soft gluons must involve at least two soft gluons. In Figure 3.5a - 3.5c the lowest order QCD diagrams inducing soft interactions are shown. Integrating out the intermediate soft heavy quark propagator in Figure 3.5a and 3.5b, as well as the potential gluon propagator in Figure 3.5c, one obtains the soft vertex shown in Figure 3.6a.

Intermediate heavy quark propagators in soft diagrams like Figure 3.5a have the form $1/q_0$ - the same as in HQET. Loop diagrams in the soft sector therefore have the same divergence structure as in HQET and the RG running can be taken from HQET calculations. To obtain the terms in the vNRQCD Lagrangian, the diagrams in Figure 3.5a-3.5c with HQET vertices are matched to the soft vertices, giving:

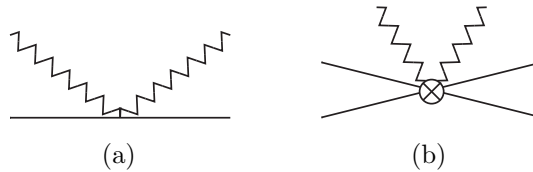


Figure 3.6: Soft vertices in vNRQCD.

$$\mathcal{L}_{\text{int}}^{\text{s}} = -g_S^2 \mu_S^{2\epsilon} \frac{1}{2} \sum_{\mathbf{p}, \mathbf{p}', q, q', \sigma} \left\{ \psi_{\mathbf{p}'}^\dagger \left[A_{q'}^\mu, A_q^\nu \right] U_{\mu\nu}^{(\sigma)} \psi_{\mathbf{p}} + \right. \\ \left. + \psi_{\mathbf{p}'}^\dagger \left\{ A_{q'}^\mu, A_q^\nu \right\} W_{\mu\nu}^{(\sigma)} \psi_{\mathbf{p}} + \dots \right\} + (\psi \rightarrow \chi, T^a \rightarrow \bar{T}^a) + \sum_{\sigma} C_{2A}^{(\sigma)} \mathcal{O}_{2A}^{(\sigma)}, \quad (3.82)$$

where U and W are functions of the external momenta and σ is the order in v of the vertex. The last term comes from 6-field vertices and is described below. Equation (3.82) shows only the soft vertices generated by gluons. Additionally, there are 4-vertices involving the light quarks and ghost fields. The full expressions for $\mathcal{L}_{\text{int}}^{\text{s}}$, U , and W can be found in [37]. Let us here just consider two terms of U for illustration:

$$U_{00}^{(0)} = \frac{1}{q_0} \\ U_{0i}^{(1)} = -\frac{(\mathbf{p} + \mathbf{p}')^i}{2m q_0} + \frac{i c_F (\mathbf{q} \times \boldsymbol{\sigma})^i}{2m q_0} + \frac{q_0 (\mathbf{p} + \mathbf{p}')^i}{2m (\mathbf{p} - \mathbf{p}')^2} + \frac{i c_F q_0 [(\mathbf{p} - \mathbf{p}') \times \boldsymbol{\sigma}]^i}{2m (\mathbf{p} - \mathbf{p}')^2}. \quad (3.83)$$

$U_{00}^{(0)}$ comes from integrating out the intermediate heavy quark propagator in Figure 3.5a and 3.5b. $U_{0i}^{(1)}$ has parts coming from all three diagrams 3.5a - 3.5c, as can be seen from the denominators. They are just the propagators of the intermediate quark and gluon, respectively, which have been integrated out of the theory. c_F is a HQET coefficient, coming from the chromomagnetic term $\delta\mathcal{L}_{\text{HQET}} = Q^\dagger c_F g \frac{\boldsymbol{\sigma} \cdot \mathbf{B}}{2m} Q$ in the HQET Lagrangian [53]. It has a running, which can be taken from HQET.

As can be seen from Equation (3.82), gauge invariance in the soft sector is not manifest. It can be restored, however, by combining it with reparametrization invariance [21].

There is one more type of soft operator corresponding to the diagram in Figure 3.6b. Its structure comes from QCD diagrams of the form shown in Figure 3.5d and generates the last term in Equation (3.82). The terms consist of the Wilson coefficients $C_{2A}^{(\sigma)}$ and the operators $\mathcal{O}_{2A}^{(\sigma)}$, given by

$$C_{2A}^{(\sigma)}(\nu = 1) = 0 \\ \mathcal{O}_{2A}^{(\sigma)} = g_S^4 \mu_S^{4\epsilon} \left[\psi_{\mathbf{p}'} \Gamma_{A, \psi}^{(\sigma)} \psi_{\mathbf{p}} \right] \left[A_{-q}^\mu \Gamma_{A, \mu\nu}^{(\sigma)} A_q^\nu \right] \left[\chi_{-\mathbf{p}'} \Gamma_{A, \chi}^{(\sigma)} \chi_{-\mathbf{p}} \right], \quad (3.84)$$

where the Γ 's are functions of the external momenta. In addition to the six-field vertices involving soft gluons, there are vertices of the same form with soft ghosts and light quarks. The exact form of these vertices can be found in [42], together with the expressions for the Γ 's.

ν is the subtraction velocity, which is related to the soft and ultrasoft renormalization scales by $\mu_S \sim m\nu$ and $\mu_U \sim m\nu^2$. The matching to the QCD amplitudes is done at $\nu = 1$ and large logarithms of v can be resummed by evolving the Wilson coefficients from $\nu = 1$ to $\nu = v$. The details are described in Section 3.3.4.

In the matching at $\nu = 1$, the Wilson coefficients of all six-field soft operators vanish at leading order. The reason is that the only diagram which could produce the operators $\mathcal{O}_{2A}^{(\sigma)}$ (Figure 3.5d) is already accounted for by combining two soft 4-vertices from Figure 3.6a. For $\nu < 1$, however, the Wilson coefficients are not zero, because they receive a running from divergences in diagrams with an additional ultrasoft gluon (see Section 3.3.4).

The factors of μ_S appearing in Equation (3.84) and (3.82) can again be determined with power counting. The soft fields A^μ scale with $(mv)^{1-\epsilon}$ and the measure with $(mv)^{-4+2\epsilon}$. Together with $\psi \sim (mv)^{3/2-\epsilon}$, this gives an extra factor $(mv)^{-2\epsilon}$ in Equation (3.82), which is absorbed by the term $\mu_S^{2\epsilon} \sim (mv)^{2\epsilon}$. Note that $\mu_S \sim mv$ differs from $\mu_U \sim mv^2$ by a factor of v .

Potential Interactions: $\mathcal{L}_{\text{int}}^{\text{P}}$

The diagram in Figure 3.5c had an intermediate potential gluon $(E, \mathbf{p}) \sim (mv^2, mv)$ and integrating it out led to the vNRQCD vertex in Figure 3.6a. Similarly, the diagrams in Figure 3.7a and 3.7b have a potential gluon and give the 4-quark interaction vertex shown in Figure 3.8. The corresponding term in the Lagrangian reads

$$\Delta\mathcal{L} = -\mu_S^{2\epsilon} \sum_{\mathbf{p}, \mathbf{p}'} V_{\alpha\beta\gamma\delta}(\mathbf{p}, \mathbf{p}') \psi_{\mathbf{p}'\alpha}^\dagger \psi_{\mathbf{p}\beta}^\dagger \chi_{-\mathbf{p}'\gamma}^\dagger \chi_{-\mathbf{p}\delta}, \quad (3.85)$$

where the indices $\alpha, \beta, \gamma, \delta$ encode the spin and color structure of the vertex and V is called a potential. It is determined by matching the diagram from Figure 3.8a to the QCD amplitudes in Figure 3.7. Multiplying out the γ matrices and expanding the 4-spinors $u_{\mathbf{p}}$ and $v_{\mathbf{p}}$ in the velocity v , one obtains from the QCD amplitude in Figure 3.7a:

$$\begin{aligned} \text{Diagram} &= -i \left(\frac{4\pi\alpha_s}{k^2} \right) [\bar{u}_{\mathbf{p}'} \gamma^\mu T^a u_{\mathbf{p}}] [\bar{v}_{\mathbf{p}} \gamma_\mu T^a v_{\mathbf{p}'}] \\ &= -i (T^a \otimes \bar{T}^a) \left(\frac{4\pi\alpha_s}{k^2} \right) \zeta_\lambda^\dagger \zeta_\lambda \xi_\lambda^\dagger \xi_\lambda + \mathcal{O}(v^{-1}), \end{aligned} \quad (3.86)$$

where $\mathbf{k} = \mathbf{p}' - \mathbf{p}$ and $(T^a \otimes \bar{T}^a) \zeta^\dagger \zeta \xi^\dagger \xi = T_{ij}^a \bar{T}_{kl}^a \zeta_i^\dagger \zeta_j \xi_k^\dagger \xi_l$ encodes the color structure of the vertex. The term in Equation (3.86) is reproduced in the effective theory by the Coulomb potential

$$V(\mathbf{p}, \mathbf{p}') = (T^a \otimes \bar{T}^a) \frac{\mathcal{V}_c^{(T)}}{k^2} + \mathcal{O}(v^{-1}), \quad (3.87)$$

where $\mathcal{V}_c^{(T)} = 4\pi\alpha_s(m)$ is the Wilson coefficient. The annihilation diagram (Figure 3.7b) can also be expanded, but gives no contribution at this order. We have seen the Coulomb potential already in Section 3.1, where it appeared in the potential regions of the vacuum polarization amplitudes (e.g. Equation (3.27)). $(T^a \otimes \bar{T}^a)$ reduces to $-C_F$ in this amplitude, since the top-antitop quark pair is produced as a color singlet state.

The Coulomb potential induces also higher order terms, which follow from reparametrization invariance. Changing $\mathbf{p} \rightarrow (\mathbf{p} - i\mathbf{D})$, the denominator obtains higher order terms in v . Expanding in v then gives the operators [39]

$$\Delta\mathcal{L} = \left(T^a \otimes \bar{T}^b \right) \mu_S^{2\epsilon} \mu_U^\epsilon \frac{\mathcal{V}_c^{(T)}}{k^4} 2ig_S f^{abc} (\mathbf{k} \cdot \mathbf{A}^c) \psi_{\mathbf{p}'} \psi_{\mathbf{p}} \chi_{-\mathbf{p}'} \chi_{-\mathbf{p}} + \dots, \quad (3.88)$$

where the dots denote terms of the same order involving kinetic insertions. The first term couples a gluon to the Coulomb vertex and the corresponding Feynman diagram is shown in Figure 3.8b.

Let's see what happens when we go to higher orders in α_s and v for the matching of the potential

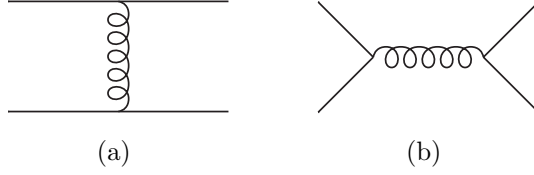


Figure 3.7: QCD vertices leading to 4-fermion vertices in the EFT.

$V(\mathbf{p}, \mathbf{p}')$. For higher order corrections in v the diagrams 3.7 have to be expanded further. At order $\mathcal{O}(v^0)$ both diagrams from Figure 3.7 contribute. They have different color structures, but these can be rewritten in the form

$$V(\mathbf{p}, \mathbf{p}') = (\mathbb{1} \otimes \mathbb{1}) V^{(1)} + (T^a \otimes \bar{T}^a) V^{(T)} \quad (3.89)$$

with Fierz identities. Also when matching at higher orders in α_s , the potentials can always be reduced to this form.

However, for physical applications another basis is more useful. The heavy quarkonium is produced either in a color singlet or octet state and Equation (3.89) is therefore rewritten in a color singlet and octet basis [45, 54, 55]

$$\begin{aligned} V(\mathbf{p}, \mathbf{p}') &= \left(\frac{1}{9} \mathbb{1} \otimes \mathbb{1} - \frac{2}{3} T^a \otimes \bar{T}^a \right) V^{(s)} + \left(\frac{8}{9} \mathbb{1} \otimes \mathbb{1} + \frac{2}{3} T^a \otimes \bar{T}^a \right) V^{(o)} \\ &= P_s V^{(s)} + P_o V^{(o)} , \end{aligned} \quad (3.90)$$

where P_s and P_o are the projection operators on the color singlet and octet state, respectively.

In this thesis, we consider the process $e^+e^- \rightarrow \gamma^* \rightarrow t\bar{t}$, where the quark-antiquark pair is produced in a color singlet state. Therefore we will include from now on only the singlet contribution in the Lagrangian $\mathcal{L}_{\text{vNRQCD}}$.

Returning to the higher order correction in v , Equation (3.86) and the annihilation diagram are expanded. This generates higher order potentials in the effective theory:

$$\begin{aligned} V(\mathbf{p}, \mathbf{p}') &= P_s \left[V_c^{(s)} + V_r^{(s)} + V_2^{(s)} + V_s^{(s)} + V_\Lambda^{(s)} + V_t^{(s)} \right] + \mathcal{O}(v^1) \\ &= P_s \left[\frac{\mathcal{V}_c^{(s)}}{\mathbf{k}^2} + \frac{\mathcal{V}_r^{(s)}}{m^2} \left(\frac{\mathbf{p}^2 + \mathbf{p}'^2}{\mathbf{k}^2} \right) + \frac{\mathcal{V}_2^{(s)}}{m^2} + \frac{\mathcal{V}_s^{(s)}}{m^2} \mathbf{S}^2 + \frac{\mathcal{V}_\Lambda^{(s)}}{m^2} \Lambda(\mathbf{p}, \mathbf{p}') + \frac{\mathcal{V}_t^{(s)}}{m^2} T(\mathbf{k}) \right] + \mathcal{O}(v^1) , \end{aligned} \quad (3.91)$$

where

$$\mathbf{S} = \frac{\boldsymbol{\sigma}_1 + \boldsymbol{\sigma}_2}{2}, \quad \Lambda(\mathbf{p}, \mathbf{p}') = -i \frac{\mathbf{S} \cdot (\mathbf{p}' \times \mathbf{p})}{\mathbf{k}^2}, \quad T(\mathbf{k}) = \boldsymbol{\sigma}_1 \cdot \boldsymbol{\sigma}_2 - \frac{3(\mathbf{k} \cdot \boldsymbol{\sigma}_1)(\mathbf{k} \cdot \boldsymbol{\sigma}_2)}{\mathbf{k}^2} \quad (3.92)$$

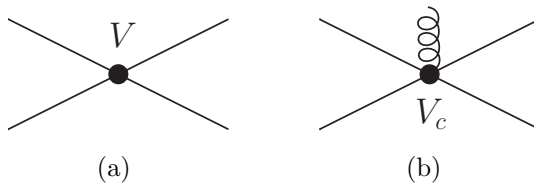


Figure 3.8: Potential vertices in the EFT.

and

$$\begin{aligned}\mathcal{V}_c^{(s)} &= -4\pi \alpha_s(m) C_F, & \mathcal{V}_r^{(s)} &= -4\pi \alpha_s(m) C_F, & \mathcal{V}_2^{(s)} &= 0, \\ \mathcal{V}_s^{(s)} &= \frac{4\pi \alpha_s(m)}{3} C_F, & \mathcal{V}_\Lambda^{(s)} &= 6\pi \alpha_s(m) C_F, & \mathcal{V}_t^{(s)} &= \frac{\pi \alpha_s(m)}{3} C_F.\end{aligned}\quad (3.93)$$

σ_1, σ_2 are the spin operators acting on the quark and the anti-quark field, respectively. $\mathcal{V}_i = \mathcal{V}_i(\nu = 1)$ are the Wilson coefficients of the different potentials at the matching scale $\mu = m$. $\mathcal{V}_2(\nu = 1)$ vanishes in the matching at this order, but similarly to the Wilson coefficient $C_{2A}^{(\sigma)}$ of the soft interaction term in Equation (3.82), it is non-zero for $\nu < 1$ (see Section 3.3.4). The higher order potentials are all of order α_s and are therefore two orders higher than the Coulomb potential $V_c \sim \alpha_s/v^2$.

After examining higher order corrections in v , let us take a look into higher order corrections in α_s . For this, the QCD amplitude has to be computed at higher loop orders. It gives contributions of the form

$$\text{Diagram 1} + \text{Diagram 2} + \dots = A \cdot \frac{\alpha_s^2}{|\mathbf{k}|} + \dots \quad (3.94)$$

The first term from Equation (3.94) is not fully reproduced with the operators from Equation (3.91) and therefore generates a new operator of the form $\alpha_s^2/|\mathbf{k}|$. This operator is of order α_s^2/v and because of $\alpha_s \sim v$ it is of the same order as the higher order potentials from Equation (3.91).

The corresponding operator in the Lagrangian is [41]

$$\Delta\mathcal{L} = \mathcal{V}_k^{(s)} \mathcal{O}_k^{(s)}, \quad (3.95)$$

where

$$\begin{aligned}\mathcal{V}_k^{(s)}(\nu = 1) &= 1 \\ \mathcal{O}_k^{(s)} &= \frac{g_S^4 \tilde{\mu}_S^{4\epsilon}}{4m} \sum_{\mathbf{p}, \mathbf{p}', \mathbf{q}} [C_1 g_0 + C_A C_F g_1 + C_F^2 g_2] [\psi_{\mathbf{p}'} \psi_{\mathbf{p}} \chi_{-\mathbf{p}'} \chi_{-\mathbf{p}}] P_s.\end{aligned}\quad (3.96)$$

The functions g_0, g_1, g_2 depend on the momenta $\mathbf{q}, \mathbf{p}, \mathbf{p}'$ and can be found in the appendix of [41]. In contrast to the potential operators from Equation (3.85), this operator has a sum over the free index \mathbf{q} . It is therefore called "sum operator" and denoted by the diagram in Figure 3.9a. The free index arises from performing only the q_0 integration of the loop diagrams from Equation (3.94). The \mathbf{q} integrations are left unevaluated to ensure consistent renormalization in the effective theory. The $1/|\mathbf{k}|$ structure can be recovered when performing the sum $\sum_{\mathbf{q}} \rightarrow \int \frac{d^n q}{(2\pi)^n}$ in $n = 3 - 2\epsilon$ dimensions and expanding for $\epsilon \rightarrow 0$ [41]

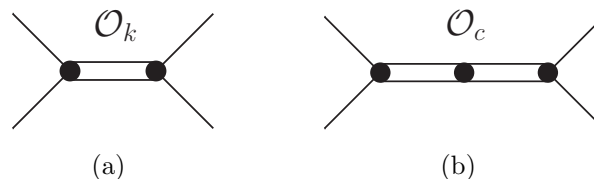


Figure 3.9: Sum operators in the EFT.

$$\int \frac{d^n q}{(2\pi)^n} [C_1 g_0 + C_A C_F g_1 + C_F^2 g_2] = -\frac{1}{4|\mathbf{k}|} \left(\frac{C_F^2}{2} - C_F C_A \right) + \mathcal{O}(\epsilon) . \quad (3.97)$$

Note that leaving the sum over \mathbf{q} unevaluated makes a difference for matrix elements with UV divergences. Together with the $\mathcal{O}(\epsilon)$ terms of the sum operators in Equation (3.97), the UV divergences would give UV finite terms, which are not present if the integral in Equation (3.97) was performed on the Lagrangian level and the $\mathcal{O}(\epsilon)$ terms discarded. Hence it is important to keep the sum unevaluated.

Renormalization induces two more types of sum operators

$$\Delta\mathcal{L} = \sum_{i=1}^3 \mathcal{V}_{ki}^{(s)} \mathcal{O}_{ki}^{(s)} + \sum_{i=1}^3 \mathcal{V}_{ci}^{(s)} \mathcal{O}_{ci}^{(s)} , \quad (3.98)$$

where

$$\begin{aligned} \mathcal{V}_{ki}^{(s)}(\nu=1) &= 0 \\ \mathcal{V}_{ci}^{(s)}(\nu=1) &= 0 \end{aligned} \quad (3.99)$$

$$\begin{aligned} \mathcal{O}_{k1}^{(s)} &= -\frac{\left(\mathcal{V}_c^{(T)} \mu_S^{2\epsilon}\right)^2}{m} \sum_{\mathbf{p}, \mathbf{p}', \mathbf{q}} [f_0 + f_1 + 2f_2] [\psi_{\mathbf{p}'} \psi_{\mathbf{p}} \chi_{-\mathbf{p}'} \chi_{-\mathbf{p}}] P_s \\ \mathcal{O}_{c1}^{(s)} &= -\left(\mathcal{V}_c^{(T)} \mu_S^{2\epsilon}\right)^3 \sum_{\mathbf{p}, \mathbf{p}', \mathbf{q}, \mathbf{q}'} [2h_0 - h_1] [\psi_{\mathbf{p}'} \psi_{\mathbf{p}} \chi_{-\mathbf{p}'} \chi_{-\mathbf{p}}] P_s . \end{aligned} \quad (3.100)$$

Only the operators $\mathcal{O}_{k1}^{(s)}$ and $\mathcal{O}_{c1}^{(s)}$ are displayed here. The other operators have a similar form and can be found in [42, 45]. In contrast to the sum operators in Equation (3.95), the Wilson coefficients $\mathcal{V}_{ki}^{(s)}$, $\mathcal{V}_{ci}^{(s)}$ are zero at the matching scale $\nu=1$ and are non-zero only for $\nu < 1$. The functions f_i and h_i depend on the sum indices \mathbf{p} , \mathbf{p}' , \mathbf{q} , \mathbf{q}' , similarly to g_i in Equation (3.95). Evaluating the sums over the free indices \mathbf{q} and \mathbf{q}' , they take the form

$$\begin{aligned} \int \frac{d^n q}{(2\pi)^n} f_i &\propto \frac{1}{|\mathbf{k}|} + \mathcal{O}(\epsilon) \\ \int \frac{d^n q}{(2\pi)^n} \frac{d^n q'}{(2\pi)^n} h_i &\propto \frac{1}{\mathbf{k}^2} + \mathcal{O}(\epsilon) . \end{aligned} \quad (3.101)$$

$\mathcal{O}_{ki}^{(s)}$ and $\mathcal{O}_{ci}^{(s)}$ therefore give contributions of order α_s^2/v and α_s^3/v^2 , respectively.

For UV finite matrix elements, the sums over the free indices can be performed in the Lagrangian. The sum operators and the Coulomb potential are then replaced by the effective potentials

$$-\Delta V(\mathbf{p}, \mathbf{p}') = \left(\frac{\pi^2}{m|\mathbf{k}|} \mathcal{V}_{\mathbf{k}, \text{eff}}^{(s)} + \frac{\mathcal{V}_{\mathbf{c}, \text{eff}}^{(s)}}{\mathbf{k}^2} \right) P_s \quad (3.102)$$

with

$$\begin{aligned}
\mathcal{V}_{\text{k, eff}}^{(s)} &= \left(\frac{C_F^2}{2} - C_A C_F \right) \alpha_s^2(m\nu) + 2 \alpha_s^2 \left(3 \mathcal{V}_{k1}^{(s)} + 2 \mathcal{V}_{k2}^{(s)} \right) \\
\mathcal{V}_{\text{c, eff}}^{(s)} &= \mathcal{V}_c^{(s)} + \pi \alpha_s^3(m\nu) \left(\mathcal{V}_{c2}^{(s)} + \mathcal{V}_{c3}^{(s)} \right) .
\end{aligned} \tag{3.103}$$

Combining the contributions from Equation (3.85), (3.95), and (3.98), the potential interaction Lagrangian takes the form

$$\begin{aligned}
\mathcal{L}_{\text{int}}^{\text{P}} &= -\mu_S^{2\epsilon} \sum_{\mathbf{p}, \mathbf{p}'} V_{\alpha\beta\gamma\delta}(\mathbf{p}, \mathbf{p}') \psi_{\mathbf{p}'\alpha}^\dagger \psi_{\mathbf{p}\beta} \chi_{-\mathbf{p}'\gamma}^\dagger \chi_{-\mathbf{p}\delta} + \\
&+ \mathcal{V}_k^{(s)} \mathcal{O}_k^{(s)} + \sum_{i=1}^3 \mathcal{V}_{ki}^{(s)} \mathcal{O}_{ki}^{(s)} + \sum_{i=1}^3 \mathcal{V}_{ci}^{(s)} \mathcal{O}_{ci}^{(s)} .
\end{aligned} \tag{3.104}$$

3.3.3 Power counting

The fields in the Lagrangian scale with specific orders of v , as we have already seen in the previous sections:

$$\begin{aligned}
[\psi] &\sim v^{3/2-\epsilon} & [A_\mu^q] &\sim v^{1-\epsilon} & [\mathbf{p}] &\sim v \\
[\chi] &\sim v^{3/2-\epsilon} & [A^\mu] &\sim v^{2(1-\epsilon)} & [\partial_\mu] &\sim v^2 .
\end{aligned} \tag{3.105}$$

The unique scaling in v of the fields and of momenta in loop graphs allows to determine the power of v for Feynman diagrams without calculating any loop integrals. The corresponding power counting formula was derived in [21]. We will denote Feynman diagrams without closed heavy fermion lines to be of order v^A , where [42]

$$A = \sum_i \left[(i-8) V_i^{(U)} + (i-5) V_i^{(P)} + (i-4) V_i^{(S)} - N_S \right] . \tag{3.106}$$

Here N_S is the number of soft loops (loops which only involve soft fields) and V_i denotes the number of vertices with power v^i , where the power of v is determined from the fields in the Lagrangian. The superscripts stand for ultrasoft (U), soft (S), and potential (P). A potential vertex has at least one fermion field and no soft fields, a soft vertex at least one soft field, and an ultrasoft vertex only ultrasoft fields. As an example, consider the soft loop from Figure 3.11a, which has two soft vertices of order $i = 4$ for $\sigma_1 = \sigma_2 = 0$ and one soft loop $N_S = 1$. Using Equation (3.106) and including also the factor α_s^2 coming from the two soft vertices, one finds that the diagram is of order α_s^2/v .

Using for the power counting the convention of Equation (3.106), the power in v can simply be

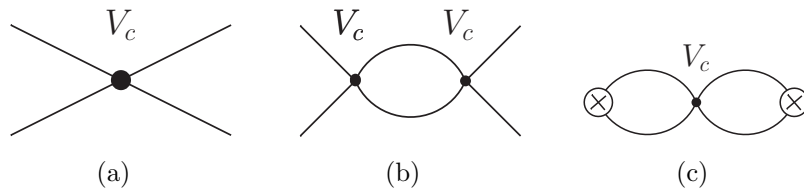


Figure 3.10: Application of the power counting formulas: for (a) and (b) Equation (3.106) is used. (a) is of order α_s/v and (b) of order α_s^2/v^2 . In (c) the fermion lines are closed using an insertion of the electromagnetic current. Applying Equation (3.107), (c) is of order $\alpha_s v^0$.

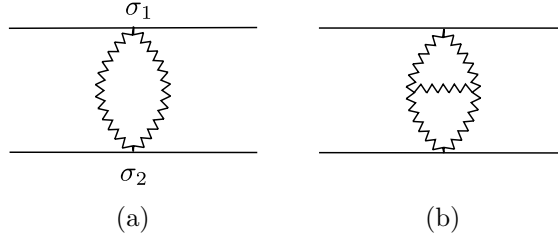


Figure 3.11: Soft loop diagrams renormalizing the potentials.

added together when joining the heavy quark and anti-quark lines of two separate diagrams. For example, the diagram in 3.10a is of order α_s/v . Joining two diagrams of this form, the resulting diagram is then of order α_s^2/v^2 .

If the fermion lines are closed, as is necessary for the calculation of the vacuum polarization, the power in v of the overall diagram is

$$A' = A + 1 . \quad (3.107)$$

Interestingly, the 4-fermion Coulomb vertex $(4\pi\alpha_s)/\mathbf{k}^2$ is of order $\alpha_s/v \sim 1$. Since Equation (3.106) tells us, that every insertion will give an additional factor of α_s/v , we can insert an arbitrary amount of these vertices in Feynman diagrams without changing the overall order of the diagram!

This behavior is called "Coulomb singularity" and we have encountered it already in section 3.1.1 in the form of the ladder diagrams (Equation (3.20)).

Also the insertion of soft loops can add a factor of $1/v$ to a diagram, because the lowest order soft vertices have $i = 4$ and $N_S = 1$. However, soft vertices also come with a factor of α_s and the lowest order loop is therefore of order α_s^2/v . In contrast to the Coulomb vertex, a soft loop insertion changes the overall order of the diagram.

Lastly, consider ultrasoft lines. Naively one would expect that one insertion of an ultrasoft line contributes as α_s at lowest order, because $\psi^\dagger A^0 \psi$ is of order v^5 . However, the leading term $\psi^\dagger A^0 \psi$ can be eliminated from the action with a field redefinition [44]. The lowest order coupling of an ultrasoft gluon to the heavy quark is therefore $\mathcal{O}(v^6)$ and insertions of ultrasoft lines in a diagram come with a factor of at least $\alpha_s v^2$.

3.3.4 Renormalization and Resummation of Logarithms

Due to the large separation of the scales E , \mathbf{p} , and m for heavy quarkonium production near threshold, large logarithms of v appear in QCD (Equation (3.4)). In vNRQCD, they can be rendered harmless by resumming them to all orders using the renormalization group equations of the Wilson coefficients.

As described in Section 3.2, effective field theories have in general more divergences than the original theory. The additional divergences are absorbed into the Wilson coefficients and induce a renormalization group (RG) running. By running the coefficients from the matching scale μ_h to the scale of the process, the logarithms can be resummed. For vNRQCD, we already encountered the soft and ultrasoft renormalization scales μ_S and μ_U respectively, in the construction of the effective Lagrangian. When calculating amplitudes, logarithms of the form

$$\log\left(\frac{|\mathbf{p}|}{\mu_S}\right), \quad \log\left(\frac{\sqrt{E/m}}{\mu_S}\right), \quad \log\left(\frac{E}{\mu_U}\right) \quad (3.108)$$

will appear. By choosing $\mu_U \sim E$ and $\mu_S \sim |\mathbf{p}|$, the logarithms become small and do not pose a problem. To first order, the energy E of the top-antitop pair and the momentum \mathbf{p} of either of the quarks is

$$|\mathbf{p}| \sim mv, \quad E \sim mv^2. \quad (3.109)$$

They are related by the equation of motion for the heavy quarkonium system $E = \mathbf{p}^2/m$ (see section 3.4.3). Accordingly, also the renormalization scales μ_U and μ_S have to be correlated by $\mu_U \sim \mu_S^2/m$. They can be expressed by one single scale in analogy to Equation (3.109)

$$\mu_S \sim m\nu, \quad \mu_U \sim m\nu^2, \quad (3.110)$$

where ν is called "subtraction velocity". This correlation between the renormalization scales is a very unique feature of vNRQCD and allows to resum logarithms of the form in Equation (3.108) simultaneously. For this the subtraction velocity is evolved from $\nu = 1$ at the matching scale to $\nu \sim v$.

There are 3 types of coefficients, which can receive an RG running through renormalization. Looking at the interaction Lagrangians from Equation (3.81), (3.82), and (3.104), one finds the following coefficients:

- the soft and ultrasoft couplings g_S and g_{US}
- the couplings between the heavy quark and soft gluon fields
- the Wilson coefficients $\mathcal{V}_i^{(s)}$ of the potentials and sum operators

The renormalization of the soft and ultrasoft couplings g_S and g_{US} is very simple. vNRQCD only modifies the interactions of gluons with the heavy quark, but not the structure of the interactions of the gluons amongst themselves. The interactions for these fields in the soft and ultrasoft sector is the same as in QCD and the renormalization of g_S and g_{US} can be taken from the strong coupling constant g in QCD. Only the choice of the renormalization scale differs between the soft and ultrasoft sector, because ultrasoft particles live at scales $m\nu^2$, while soft particles live at $m\nu$:

$$\frac{g_S^2}{4\pi} = \alpha_S = \alpha_s(\mu_S), \quad \frac{g_{US}^2}{4\pi} = \alpha_{US} = \alpha_s(\mu_U), \quad (3.111)$$

where $\mu_S \sim m\nu$ is the soft and $\mu_U \sim m\nu^2$ the ultrasoft scale. The couplings between the heavy quark and the soft gluons describing e.g. the vertices from Figure 3.6a, are renormalized only by soft modes. Their renormalization can be taken from HQET and is encoded in the HQET coefficients c_F, c_s, \dots

Note that ultrasoft modes do not contribute to the renormalization of the soft 4-vertex, because soft and ultrasoft modes can not be distinguished in the single heavy quark sector [39, 42].

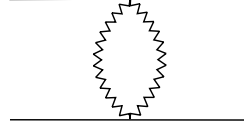
The 6 particle vertex from Figure 3.6b, on the other hand, has both the heavy quark and anti-quark and is therefore also renormalized by ultrasoft gluons:

$$\begin{array}{ll} \begin{array}{c} \text{Diagram 1: A vertex with two heavy quark lines (solid) and two gluon lines (wavy) meeting at a central point. The gluon lines are labeled with } \sigma = 2. \end{array} & \text{renormalized at LL by} \quad \begin{array}{c} \text{Diagram 2: A vertex with two heavy quark lines and two gluon lines. The gluon lines are labeled with } \sigma = 0. \end{array}, \dots \quad [42, 43] \\ \begin{array}{c} \text{Diagram 3: A vertex with two heavy quark lines and two gluon lines. The gluon lines are labeled with } \sigma = 2. \end{array} & \text{renormalized at NLL by} \quad \begin{array}{c} \text{Diagram 4: A vertex with two heavy quark lines and two gluon lines. The gluon lines are labeled with } \sigma = 0. \end{array}, \dots \quad [42, 43], \quad (3.112) \end{array}$$

where $\sigma = 0, 2$ refer to the v scaling of the soft vertices and the dots stand for all possible combinations of attaching the gluon line to the fermion lines. Note that only the $\sigma = 2$ vertex receives a running, because the soft vertices on the right side are already of the lowest order in v and gluon

lines add altogether at least a factor of v^2 to the counting.

The Wilson coefficients $\mathcal{V}_i^{(s)}$ can be renormalized by both soft and ultrasoft fields. Consider first the Coulomb potential V_c . It is renormalized only by soft loops, two of which are shown in Figure 3.11. At lowest order in v (i.e. $\sigma_1 = \sigma_2 = 0$), the first diagram has a divergence proportional to the β_0 coefficient of the α_s β -function [49]



$$= -i\mu_S^{2\epsilon} \frac{g_S^4}{4\pi \mathbf{k}^2} \frac{\beta_0}{\epsilon} (T^a \otimes \bar{T}^a) + \dots \quad (3.113)$$

It is therefore associated to the renormalization of the running coupling g_S . At two and three loops, the divergences are also related to the β coefficients and are absorbed by the counterterms of g_S . The Wilson coefficient $\mathcal{V}_c^{(s)}$ with three-loop running therefore has the particularly simple form

$$\mathcal{V}_c^{(s)} = -4\pi \alpha_s^{[3]}(m\nu) C_F, \quad (3.114)$$

where the superscript [3] denotes the three-loop running of α_s .

Note that the diagrams renormalizing a certain potential have to reproduce the momentum and spin structure of the potential, and therefore also the correct power of v . The Coulomb potential, for example, is of order α_s/v . Using Equation (3.106) we can see that the soft one-loop diagram in Figure 3.11a is of order α_s^2/v (for $\sigma_1 = \sigma_2 = 0$) and can therefore renormalize the Coulomb potential.

Adding one ultrasoft line, on the other hand, produces diagrams, which can not renormalize V_c . The gluon lines add a factor of v^2 in the counting and a diagram of the form



$$\quad (3.115)$$

is of order $\alpha_s v$. This is the order of the higher order potentials and therefore renormalizes them instead of V_c .

The only diagrams that have the same power in v as V_c appear at higher orders, e.g.



$$\quad (3.116)$$

Diagrams of this type are of order $\alpha_s^3/v^3 \cdot v^2 \sim \alpha_s^3/v$. However, their divergences are of the form $\frac{1}{\epsilon} \sum_{\mathbf{q}} f(\mathbf{p}, \mathbf{p}', \mathbf{q})$ and they therefore renormalize the sum operators $\mathcal{O}_{c1}^{(s)}$, $\mathcal{O}_{c2}^{(s)}$, and $\mathcal{O}_{c3}^{(s)}$ instead of the Coulomb potential. The resulting expressions of the Wilson coefficients $\mathcal{V}_{c1}^{(s)}$, $\mathcal{V}_{c2}^{(s)}$, $\mathcal{V}_{c3}^{(s)}$ can be found in [42].

The other potentials receive their running through soft diagrams like Figure 3.11a (with $\sigma_1 + \sigma_2 = 2$) and through mixing from diagrams like Equation (3.115). The LL renormalization of the potentials has the following structure

	renormalized by	, $\sigma = 2$	[38]
	renormalized by		[38, 42]
	renormalized by	, ...	[39, 41, 42]
	renormalized by	, ...	[42]
	renormalized by	, ...	[42] . (3.117)

The dots stand for diagrams of similar form and the details of the renormalization can be found in the references next to the diagrams.

Note that interactions with ultrasoft gluons and soft gluons with a $\sigma = 0$ vertex do not depend on the spin of the heavy quark and anti-quark. Consequently, diagrams including only these vertices renormalize the spin-independent potentials V_c , V_2 , and V_r , as can be seen in the first line (the vertex of the soft loop is non-zero only through its running, and the running in turn originates from diagrams with $\sigma = 0$ vertices, see (3.112)).

The soft loop in the second line, on the other hand, has $\sigma_1 = \sigma_2 = 0$ for the renormalization of V_c and $\sigma_1 + \sigma_2 = 2$ for the higher order potentials. It has terms that affect the spin structure and therefore renormalizes also the spin-dependent potentials. The $\mathcal{O}_k^{(s)}$ in the third line involves only soft loops and the loop diagrams are proportional to the β function coefficients. Therefore, they simply renormalize the coupling g_s , leaving the form given in Equation (3.96) otherwise unchanged.

At NLL, the ultrasoft renormalization of the spin-independent potentials V_2 and V_r , and the sum operators $\mathcal{O}_{k1}^{(s)}$, $\mathcal{O}_{k2}^{(s)}$, $\mathcal{O}_{k3}^{(s)}$ has been calculated in [43–45]. It involves diagrams of the form

	renormalized by	, ...	[43, 44]
	renormalized by	, ...	[44, 45] . (3.118)

The full NLL running of the potentials also includes further soft contributions. They are currently unknown, but are assumed to be tiny for top quark pair production when compared to the error from the variation of the renormalization scales (see also the discussion in Section 3.4.1).

3.4 Top Quark Pair Production in vNRQCD

Now that we have set up the formalism of vNRQCD to calculate contributions at threshold and resum logarithms of v to all orders, we can finally tackle the problem of the Coulomb singularity.

In Section 3.1.1 we saw, that the leading order contributions are of order v , α_s , α_s^2/v , \dots . In this work we will consider contributions up to NNLO, which take schematically the form

$$\sigma_{\text{NNLO}}^{\text{FO}} = v \sum_n \left(\frac{\alpha_s}{v} \right)^n + v^2 \sum_n \left(\frac{\alpha_s}{v} \right)^n + v^3 \sum_n \left(\frac{\alpha_s}{v} \right)^n . \quad (3.119)$$

Here the first term corresponds to the LO contributions and adding the second and third part gives the NLO and NNLO cross section, respectively. Since the logarithms are not resummed, we call this form of the cross section fixed-order (FO).

Using vNRQCD to resum the logarithms in v , the cross section takes the form:

$$\begin{aligned} \sigma_{\text{NNLL}}^{\text{RGI}} &= v \sum_{n,m} \left(\frac{\alpha_s}{v} \right)^n (\alpha_s \log v)^m \\ &+ v^2 \sum_{n,m} \left(\frac{\alpha_s}{v} \right)^n (\alpha_s \log v)^m \\ &+ v^3 \sum_{n,m} \left(\frac{\alpha_s}{v} \right)^n (\alpha_s \log v)^m . \end{aligned} \quad (3.120)$$

The first line now gives the leading-logarithm (LL) contributions the second NLL, and the third NNLL. The logarithms are resummed with the renormalization group equation of the Wilson coefficients and we will therefore call this cross section renormalization-group-improved (RGI).

We will now calculate the contributions to the NNLL RGI cross section in three steps. First, we have to know the coupling of the photons to the heavy quark fields, which we have not treated up to now. Second, we need to identify the NLO and NNLO order contributions. Finally, the Coulomb singularity needs to be resummed, which we will achieve with the Schrödinger equation.

3.4.1 Production Current

The inclusive top quark pair production cross section can be calculated in QCD from the vacuum polarization (Section 2.1), which is defined with the electromagnetic current $j^\mu(x) = \bar{\psi}(x) \gamma^\mu \psi(x)$. Using Equation (3.69), the current can be rewritten in the form

$$\begin{aligned} j^i(x) &= e^{-2imt} \sum_{\mathbf{p}} \left[\psi_{\text{full}}^+(x, \mathbf{p}) \gamma^i \psi_{\text{full}}^-(x, -\mathbf{p}) \right] + h.c. \\ &= e^{-2imt} \sum_{\mathbf{p}} \left(J_{\mathbf{p}}^i(x) + h.c. \right) + \mathcal{O}(v^3) , \end{aligned} \quad (3.121)$$

where \mathbf{p} is the soft momentum and $J_{\mathbf{p}}^i$ is the non-relativistic current including terms up to $\mathcal{O}(v^2)$. To calculate the non-relativistic current, we expand the spinors $u_{\mathbf{p}}$ and $v_{-\mathbf{p}}$, which are contained in ψ_{full}^+ and ψ_{full}^- , respectively:

$$\begin{aligned}
\bar{u}_{\mathbf{p}} \gamma^i v_{-\mathbf{p}} &= \zeta_{\mathbf{p}}^\dagger \sigma^i (i\sigma_2 \xi_{-\mathbf{p}}^*) - \frac{1}{2m^2} \zeta_{\mathbf{p}}^\dagger \left[(\boldsymbol{\sigma} \cdot \mathbf{p}) p^i \right] (i\sigma_2 \xi_{-\mathbf{p}}^*) \\
&= \zeta_{\mathbf{p}}^\dagger \sigma^i (i\sigma_2 \xi_{-\mathbf{p}}^*) + \frac{1}{m^2} \zeta_{\mathbf{p}}^\dagger \left[-\frac{1}{2} \left((\boldsymbol{\sigma} \cdot \mathbf{p}) p^i - \frac{1}{3} \mathbf{p}^2 \sigma^i \right) - \frac{1}{6} \mathbf{p}^2 \sigma^i \right] (i\sigma_2 \xi_{-\mathbf{p}}^*),
\end{aligned} \tag{3.122}$$

where the spin indices have been suppressed. Plugging (3.122) into ψ_{full}^\pm in Equation (3.121), the non-relativistic current takes the form

$$J_{\mathbf{p}}^i = c_1 \mathcal{O}_{\mathbf{p},1}^i + c_2 \mathcal{O}_{\mathbf{p},2}^i + c_4 \mathcal{O}_{\mathbf{p},4}^i, \tag{3.123}$$

where

$$\begin{aligned}
c_1 &= 1 + \mathcal{O}(\alpha_s), & \mathcal{O}_{\mathbf{p},1}^i &= \psi_{\mathbf{p}}^\dagger \sigma^i (i\sigma_2 \chi_{-\mathbf{p}}^*) \\
c_2 &= -\frac{1}{6} + \mathcal{O}(\alpha_s), & \mathcal{O}_{\mathbf{p},2}^i &= \frac{1}{m^2} \psi_{\mathbf{p}}^\dagger \mathbf{p}^2 \sigma^i (i\sigma_2 \chi_{-\mathbf{p}}^*) \\
c_4 &= -\frac{1}{2} + \mathcal{O}(\alpha_s), & \mathcal{O}_{\mathbf{p},4}^i &= \frac{1}{m^2} \psi_{\mathbf{p}}^\dagger \left((\boldsymbol{\sigma} \cdot \mathbf{p}) p^i - \frac{1}{3} \mathbf{p}^2 \sigma^i \right) (i\sigma_2 \chi_{-\mathbf{p}}^*).
\end{aligned} \tag{3.124}$$

The first two operators produce s-wave states and are of order v^0 and v^2 , respectively. They can contribute to the NNLO cross section in the form $\langle \mathcal{O}_{\mathbf{p},1} \mathcal{O}_{\mathbf{p},1}^\dagger \rangle$ and $\langle \mathcal{O}_{\mathbf{p},2} \mathcal{O}_{\mathbf{p},1}^\dagger + \mathcal{O}_{\mathbf{p},1} \mathcal{O}_{\mathbf{p},2}^\dagger \rangle$. $\langle \mathcal{O}_{\mathbf{p},2} \mathcal{O}_{\mathbf{p},2}^\dagger \rangle$ is suppressed by v^4 and is therefore beyond NNLO.

The third operator describes d-wave states, which are orthogonal to s-wave states: $\langle \mathcal{O}_{\mathbf{p},1} \mathcal{O}_{\mathbf{p},4}^\dagger \rangle = 0$. It can therefore only contribute through $\langle \mathcal{O}_{\mathbf{p},4} \mathcal{O}_{\mathbf{p},4}^\dagger \rangle$, which is v^4 suppressed, and is not included in the NNLO cross section.

There is also a p-wave current $\mathcal{O}_{\mathbf{p},3}$ coming from the expansion of the axial production current. It contributes at NNLO through $\langle \mathcal{O}_{\mathbf{p},3} \mathcal{O}_{\mathbf{p},3}^\dagger \rangle$ and comes from Z-boson exchange. We do not consider Z-boson exchange in this thesis, but the contribution originating from $\mathcal{O}_{\mathbf{p},3}$ can be found in [47].

With the expansion in v of Equation (3.122) we have already performed the tree level matching for the Wilson coefficients c_1 and c_2 . They will however receive higher order corrections through loop diagrams. Figure 3.12 shows the matching for c_1 at NLO. The left diagram is the QCD diagram, which can be calculated with the method of regions. It has a potential part and a hard part. The potential part is reproduced by the vNRQCD diagram 3.12b and the hard part goes into the Wilson coefficient c_1 . At higher orders, divergences appear in the matching, which are canceled by the counterterm Z_{c_1} of c_1 . Together with the NNLO matching, the renormalized Wilson coefficient c_1 for $\nu = 1$ reads [56]

$$c_1(1, h) = 1 - C_F \frac{2}{\pi} \alpha_h + \alpha_h^2 \left[C_F^2 \left(\frac{\log 2}{3} - \frac{31}{24} - \frac{2}{\pi^2} \right) + C_F C_A \left(\frac{\log 2}{2} - \frac{5}{8} \right) + \frac{\kappa}{2} \right], \tag{3.125}$$

where $\mu_h = hm$ is the matching scale and κ can be found in [46]. For the NNLO contributions, c_1 is needed up to α_s^2 , because $\mathcal{O}_{\mathbf{p},1}$ is of order v^0 . For c_2 on the other hand, the $\mathcal{O}(\alpha_s^0)$ matching is sufficient, because $\mathcal{O}_{\mathbf{p},2}$ is already of order v^2 .

Additionally to corrections in α_s , c_1 absorbs divergences from loop diagrams and therefore has an RG running. For the NNLL cross section, we need the running of c_1 and c_2 . For c_2 the LL running

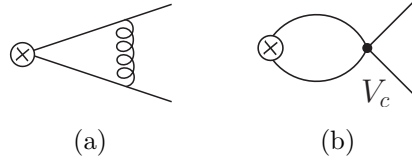


Figure 3.12: Determination of c_1 at NLO by matching. The difference between the QCD diagram (a) and the effective diagram (b) is put into Wilson coefficient c_1 .

is sufficient and was calculated in [47]:

$$c_2(\nu, h) = -\frac{1}{6} - \frac{8 C_F}{3 \beta_0} \log \left(\frac{\alpha_{US}}{\alpha_h} \right) \quad \text{with} \quad \alpha_{US} = \alpha_s(mh \nu^2). \quad (3.126)$$

For c_1 , on the other hand, the running up to NNLL is needed, i.e. the three-loop anomalous dimension

$$\nu \frac{\partial}{\partial \nu} \log [c_1(\nu, h)] = \gamma^{\text{NLL}} + \gamma_{\text{mix}}^{\text{NNLL}} + \gamma_{\text{non-mix}}^{\text{NNLL}}, \quad (3.127)$$

where the NNLL anomalous dimension is split into non-mixing $\gamma_{\text{non-mix}}^{\text{NNLL}}$ and mixing $\gamma_{\text{mix}}^{\text{NNLL}}$ contributions, which are explained below.

At one-loop, the diagram from Figure 3.12b is finite and the LL anomalous dimension of c_1 is therefore zero. At two-loop, however, the anomalous dimension is not zero. There are three types of diagrams which generate divergences at this order. An example is shown in Figure 3.13a. Using the V_2 potential in this diagram, the integral takes the form of $I^{(2)}(1, 1, 1; m^2)$ (see appendix D) and using Equation (D.9) the diagram has the following divergence:

$$\text{Diagram (a)} = -c_1 \mathcal{V}_c^{(s)} \mathcal{V}_2^{(s)} \sigma_i \left(\frac{1}{16\pi^2 \epsilon} + \dots \right). \quad (3.128)$$

Absorbing the divergence in c_1 , the running of c_1 originating from Equation (3.128) can easily be calculated to be $\nu \frac{\partial \log c_1}{\partial \nu} = -\mathcal{V}_c^{(s)}(\nu) \mathcal{V}_2^{(s)}(\nu) \frac{1}{64\pi^2}$. Including also diagrams with the $V_{r,s}$ potentials, as well as diagrams with sum operators and kinetic insertions, the full NLL anomalous dimension reads [21, 41]:

$$\begin{aligned} \gamma^{\text{NLL}} = & -\frac{\mathcal{V}_s^{(s)}}{16\pi^2} \left[\frac{\mathcal{V}_c^{(s)}}{4} + \mathcal{V}_2^{(s)} + \mathcal{V}_r^{(s)} + \mathcal{S}^2 \mathcal{V}_s^{(s)} \right] + \alpha_s^2(m\nu) \left[\frac{C_F^2}{2} - C_F C_A \right] \\ & + \alpha_s^2(m\nu) \left[3\mathcal{V}_{k1}^{(s)} + 2\mathcal{V}_{k2}^{(s)} \right], \end{aligned} \quad (3.129)$$

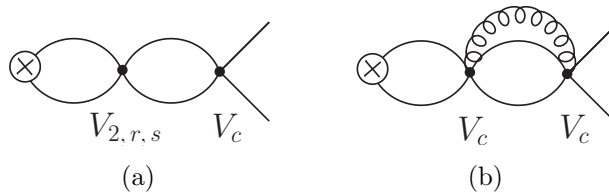


Figure 3.13: Example diagrams for the running of c_1 at (a) NLL and (b) NNLL order.

where the potentials and α_s have LL running.

At NNLL order, there are two kinds of contributions. Including the NLL running of the potentials in Equation (3.129) gives the mixing contributions $\gamma_{\text{mix}}^{\text{NNLL}}$. Additionally, three-loop vertex diagrams with an extra soft or ultrasoft loop lead to the non-mixing contributions $\gamma_{\text{non-mix}}^{\text{NNLL}}$. An example of a diagram contributing to $\gamma_{\text{non-mix}}^{\text{NNLL}}$ is shown in Figure 3.13b and the full calculation of all contributions can be found in [41].

The solution of the RG Equation (3.127) for c_1 can be written as

$$\log \left[\frac{c_1(\nu, h)}{c_1(1, h)} \right] = \xi^{\text{NLL}}(\nu, h) + \xi_{\text{non-mix, us}}^{\text{NNLL}}(\nu, h) + \xi_{\text{mix, us}}^{\text{NNLL}}(\nu, h) + \xi_{\text{non-mix, s}}^{\text{NNLL}}(\nu, h) + \xi_{\text{mix, s1}}^{\text{NNLL}}(\nu, h) , \quad (3.130)$$

where the exact expressions for ξ can be found in [56].

For $\xi_{\text{mix}}^{\text{NNLL}}$, the ultrasoft contributions to the NLL running of the potentials have been calculated in [43–45]. For the soft mixing contributions, only the linear logarithmic term $\alpha_s^3 \log \nu$ is known [41] and denoted above as $\xi_{\text{soft1}}^{\text{NNLL}}$, but the remaining terms are expected to be small. In fact, the known soft contributions to $\xi_{\text{non-mix, s}}^{\text{NNLL}}$ are about 20 times smaller than the overall ultrasoft contributions $\xi_{\text{non-mix, us}}^{\text{NNLL}}$. Expecting a similar size for the unknown soft mixing contributions, their effect would be much smaller than the variation of the renormalization scale ν and can safely be neglected. For a detailed discussion see [57].

3.4.2 LO, NLO, and NNLO Contributions

With the vNRQCD formalism set up in Section 3.3 and the non-relativistic expansion of the production current in Equation (3.123), we can now identify the LO, NLO, and NNLO contributions to the top quark pair production cross section at threshold.

Taking Equations (2.9) and (2.3) for the cross section derived in Chapter 2 and replacing the relativistic current with its non-relativistic form from Equations (3.121) and (3.123), the non-relativistic cross section becomes [47]

$$\begin{aligned} \sigma_{\text{vNRQCD}} &= \frac{4\pi}{s} Q_t^2 \sigma_{\text{pt}} \text{Im} \left[-i \int d^4x e^{iq \cdot x} \langle 0 | T j_\mu(x) j^\mu(0) | 0 \rangle \right] \\ &= \frac{4\pi}{s} Q_t^2 \sigma_{\text{pt}} \text{Im} \left[i \sum_{\mathbf{p}, \mathbf{p}'} \int d^4x e^{i\hat{q} \cdot x} \langle 0 | T \mathbf{J}_{\mathbf{p}}(x) \mathbf{J}_{\mathbf{p}'}^\dagger(0) | 0 \rangle \right] \\ &= \frac{4\pi}{s} Q_t^2 \sigma_{\text{pt}} \text{Im} \left[c_1^2(\nu) \mathcal{A}_1(v, m, \nu) + 2 c_1(\nu) c_2(\nu) \mathcal{A}_2(v, m, \nu) \right] , \end{aligned} \quad (3.131)$$

where $q = (\sqrt{s}, \mathbf{0})$ and $\hat{q} = (\sqrt{s} - 2m, \mathbf{0})$. \sqrt{s} is the CM energy and is related to the velocity v by

$$v = \sqrt{\frac{E}{m}} = \sqrt{\frac{\sqrt{s} - 2m + i\varepsilon}{m}} . \quad (3.132)$$

The form of the exponential $e^{i\hat{q} \cdot x}$ in Equation (3.123) follows from Equation (3.121). c_1 and c_2 are the Wilson coefficients, and $\mathcal{A}_1, \mathcal{A}_2$ the matrix elements containing the production currents $\mathcal{O}_{\mathbf{p}, 1}, \mathcal{O}_{\mathbf{p}, 2}$:

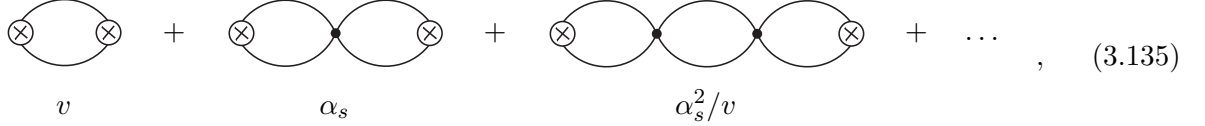
$$\begin{aligned}
\mathcal{A}_1(v, m, \nu) &= i \sum_{\mathbf{p}, \mathbf{p}'} \int d^4x e^{i\hat{q}\cdot x} \langle 0 | T \mathcal{O}_{\mathbf{p},1}(x) \mathcal{O}_{\mathbf{p}',1}^\dagger(0) | 0 \rangle \\
\mathcal{A}_2(v, m, \nu) &= \frac{i}{2} \sum_{\mathbf{p}, \mathbf{p}'} \int d^4x e^{i\hat{q}\cdot x} \langle 0 | T \left(\mathcal{O}_{\mathbf{p},1}(x) \mathcal{O}_{\mathbf{p}',2}^\dagger(0) + \mathcal{O}_{\mathbf{p},2}(x) \mathcal{O}_{\mathbf{p}',1}^\dagger(0) \right) | 0 \rangle . \quad (3.133)
\end{aligned}$$

Since the only difference between $\mathcal{O}_{\mathbf{p},1}$ and $\mathcal{O}_{\mathbf{p},2}$ is a factor of $p^2/m^2 = v^2$, \mathcal{A}_2 is related to \mathcal{A}_1 by

$$\mathcal{A}_2 = v^2 \mathcal{A}_1 . \quad (3.134)$$

The contributions to \mathcal{A}_1 and \mathcal{A}_2 follow from power counting (see Equation (3.106)): an insertion of the Coulomb potential V_c increases the power of the overall diagram by a factor α_s/v and the lowest order soft loop increases it by a factor of α_s^2/v . The higher order potentials $V_{2,r,s}$ add $\alpha_s v$ to the counting and the sum operators \mathcal{O}_{ki} a factor of α_s^2 . Additionally, using the production current $\mathcal{O}_{\mathbf{p},2}$ instead of $\mathcal{O}_{\mathbf{p},1}$ increases the power of v by 2.

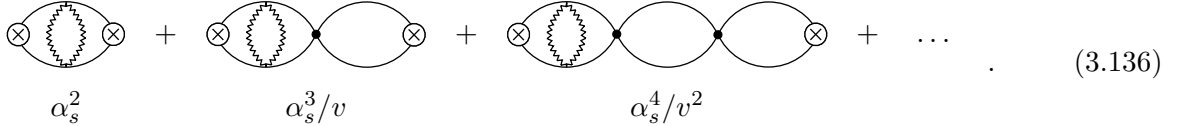
At LO, there are only insertions of V_c , denoted here by black circles:



$$\text{Diagram 1} + \text{Diagram 2} + \text{Diagram 3} + \dots , \quad (3.135)$$

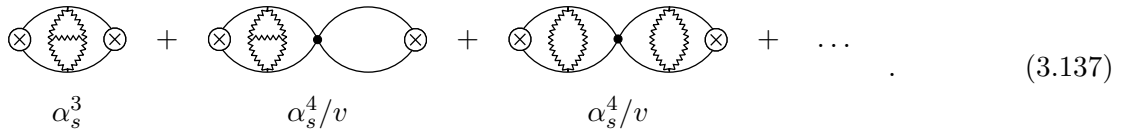
where the term below the diagrams denotes their power in α_s and v . The crossed circle denotes an insertion of the $\mathcal{O}_{\mathbf{p},1}$ current.

At NLO there are additionally insertions of soft loops, which raise the power of the diagram by α_s^2/v :



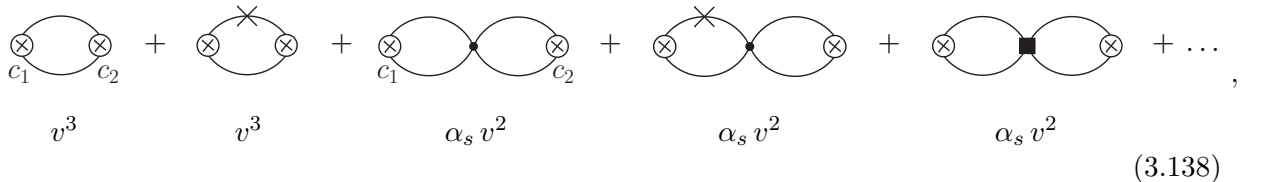
$$\text{Diagram 1} + \text{Diagram 2} + \text{Diagram 3} + \dots . \quad (3.136)$$

Finally, at NNLO higher order soft loops contribute:



$$\text{Diagram 1} + \text{Diagram 2} + \text{Diagram 3} + \dots . \quad (3.137)$$

Additionally, there are contributions from the higher order potentials $V_{2,r,s}$, the sum operators, and kinetic insertions:



$$\text{Diagram 1} + \text{Diagram 2} + \text{Diagram 3} + \text{Diagram 4} + \text{Diagram 5} + \dots , \quad (3.138)$$

where the cross denotes a kinetic insertion and the square a 4-fermion vertex coming from the higher order potentials. Note that ultrasoft loops only contribute beyond NNLO, since ultrasoft lines add at least a factor of $\alpha_s v^2$ to a diagram. From the higher order potentials in Equation (3.91) all potentials contribute except V_Λ and V_t .

The soft loops in Equation (3.136) and (3.137) behave similar to a potential, because they are proportional to $1/\mathbf{k}^2$ and therefore have a similar form as the Coulomb potential. Hence an effective Coulomb potential can be defined by [47]

$$V_{\text{c, eff}} = \frac{\mathcal{V}_{\text{c, eff}}^{(s)}}{\mathbf{k}^2} - \frac{\alpha_s^2(m\nu)}{\mathbf{k}^2} C_F [-\beta_0 \log(\mathbf{k}^2/m^2\nu^2) + a_1] \\ - \frac{\alpha_s^3(m\nu)}{\mathbf{k}^2} \frac{C_F}{4\pi} [\beta_0^2 \log^2(\mathbf{k}^2/m^2\nu^2) - (2\beta_0 a_1 + \beta_0) \log(\mathbf{k}^2/m^2\nu^2) + a_2] , \quad (3.139)$$

where the second and third term are contributions from one-loop and two-loop soft diagrams and were first calculated in [58, 59]. β_0 and β_1 are the coefficients of the α_s β -function and a_1, a_2 can be found in [59]. $\mathcal{V}_{\text{c, eff}}^{(s)}$ is the Wilson coefficient of the effective potential including the \mathcal{O}_{ci} sum operators (see Equation (3.103)).

Using the effective Coulomb potential, the insertions at LO, NLO, and NNLO can be summarized in the form:

$$V_{\text{LO}} = V_{\text{c, eff}}^{\text{LO}} \\ V_{\text{NLO}} = V_{\text{c, eff}}^{\text{NLO}} \\ V_{\text{NNLO}} = V_{\text{c, eff}}^{\text{NNLO}} + V_2^{(s)} + V_s^{(s)} + V_r^{(s)} + V_k^{(s)} + \sum_i V_{ki}^{(s)} , \quad (3.140)$$

where $V_{\text{c, eff}}^{\text{LO}}, V_{\text{c, eff}}^{\text{NLO}}$, and $V_{\text{c, eff}}^{\text{NNLO}}$ include the contributions from Equation (3.139) up to α_s, α_s^2 , and α_s^3 , respectively. $V_k^{(s)}$ and $V_{ki}^{(s)}$ are the potentials coming from the sum operators in Equation (3.95) and (3.98), respectively. $V_k^{(s)}$ and $V_{k1}^{(s)}$ read

$$V_k^{(s)} = \mathcal{V}_k^{(s)} \frac{g_S^4 \tilde{\mu}_S^{4\epsilon}}{4m} \sum_{\mathbf{p}, \mathbf{p}', \mathbf{q}} [C_1 g_0 + C_A C_F g_1 + C_F^2 g_2] \\ V_{k1}^{(s)} = \mathcal{V}_{k1}^{(s)} \frac{(\mathcal{V}_c^{(T)} \mu_S^{2\epsilon})^2}{m} \sum_{\mathbf{p}, \mathbf{p}', \mathbf{q}} [f_0 + f_1 + 2 f_2] \quad (3.141)$$

and $V_{k2}^{(s)}$ and $V_{k3}^{(s)}$ follow analogously from Equation (3.98).

3.4.3 Resummation of the Coulomb Singularity

The infinite sum from Equation (3.135)-(3.138) can be rewritten into an integral equation, which turns out to be just the non-relativistic Schrödinger equation known from quantum mechanics. By solving it the contributions are resummed to all orders.

For the derivation of the integral equation we start with the expressions for the LO contributions after the p^0 integrations. They were calculated for the first three loop orders using the method of regions in Equation (3.16), (3.28), and (3.31), respectively, and have the form:

$$\begin{aligned}
(-i) \otimes \text{---} \text{---} \otimes &= 6N_c \tilde{\mu}_S^{2\varepsilon} \int \frac{d^n \mathbf{p}}{(2\pi)^n} P(\mathbf{p}) \\
(-i) \otimes \text{---} \text{---} \otimes &= -6N_c \tilde{\mu}_S^{4\varepsilon} \int \frac{d^n \mathbf{p}_1}{(2\pi)^n} \frac{d^n \mathbf{p}_2}{(2\pi)^n} P(\mathbf{p}_1) \tilde{V}_{\text{LO}}(\mathbf{p}_1, \mathbf{p}_2) P(\mathbf{p}_2) \\
(-i) \otimes \text{---} \text{---} \otimes &= 6N_c \tilde{\mu}_S^{6\varepsilon} \int \frac{d^n \mathbf{p}_1}{(2\pi)^n} \frac{d^n \mathbf{p}_2}{(2\pi)^n} \frac{d^n \mathbf{p}_3}{(2\pi)^n} P(\mathbf{p}_1) \tilde{V}_{\text{LO}}(\mathbf{p}_1, \mathbf{p}_2) P(\mathbf{p}_2) \tilde{V}_{\text{LO}}(\mathbf{p}_2, \mathbf{p}_3) P(\mathbf{p}_3) \\
&\vdots \qquad \qquad \qquad \vdots
\end{aligned} \tag{3.142}$$

where

$$\begin{aligned}
P(\mathbf{p}) &= \frac{-1}{E - \mathbf{p}^2/m + i\varepsilon} \\
\tilde{V}_{\text{LO}}(\mathbf{p}_1, \mathbf{p}_2) &= \frac{-4\pi\alpha_s C_F}{(\mathbf{p}_1 - \mathbf{p}_2)^2} .
\end{aligned} \tag{3.143}$$

In this section we use a tilde over V and G to distinguish between momentum and position space. The diagrams above correspond to the leading order contributions of \mathcal{A}_1 (Equation (3.133)) and therefore the indices on g^{ij} have been contracted to $(2g^i_i) N_c = 6N_c$. The pattern of Equation (3.142) continues to all orders, as can be easily seen by applying the methods described in Section 3.1 to the higher loop orders. To sum the contributions, we define the function $G(\mathbf{p}_1, \mathbf{p}_2)$

$$\begin{aligned}
\mathcal{A}_{1,\text{LO}} &= (-i) \otimes \text{---} \text{---} \otimes + (-i) \otimes \text{---} \text{---} \otimes + \dots \\
&= 6N_c \tilde{\mu}_S^{2\varepsilon} \int \frac{d^n \mathbf{p}_1}{(2\pi)^n} \frac{d^n \mathbf{p}_2}{(2\pi)^n} \tilde{G}_{\text{LO}}(\mathbf{p}_1, \mathbf{p}_2) .
\end{aligned} \tag{3.144}$$

Using the expressions for the ladder diagrams from Equation (3.142), the above equation takes the form

$$\begin{aligned}
\tilde{G}_{\text{LO}}(\mathbf{p}_1, \mathbf{p}_2) &= (2\pi)^n \delta^{(n)}(\mathbf{p}_1 - \mathbf{p}_2) P(\mathbf{p}_1) - P(\mathbf{p}_1) \tilde{V}_{\text{LO}}(\mathbf{p}_1, \mathbf{p}_2) P(\mathbf{p}_2) \\
&\quad + \tilde{\mu}_S^{2\varepsilon} \int \frac{d^n \mathbf{p}_3}{(2\pi)^n} P(\mathbf{p}_1) \tilde{V}_{\text{LO}}(\mathbf{p}_1, \mathbf{p}_3) P(\mathbf{p}_3) \tilde{V}_{\text{LO}}(\mathbf{p}_3, \mathbf{p}_2) P(\mathbf{p}_2) \\
&\quad - \dots ,
\end{aligned} \tag{3.145}$$

which can be rewritten into the following integral equation:

$$\tilde{G}_{\text{LO}}(\mathbf{p}_1, \mathbf{p}_2) = (2\pi)^n \delta^{(n)}(\mathbf{p}_1 - \mathbf{p}_2) P(\mathbf{p}_1) - \tilde{\mu}_S^{2\varepsilon} \int \frac{d^n \mathbf{p}_3}{(2\pi)^n} P(\mathbf{p}_1) \tilde{V}_{\text{LO}}(\mathbf{p}_1, \mathbf{p}_3) \tilde{G}_{\text{LO}}(\mathbf{p}_3, \mathbf{p}_2) . \tag{3.146}$$

Inserting $P(\mathbf{p})$ and rewriting the equation gives

$$\left(\frac{\mathbf{p}_1^2}{m} - E \right) \tilde{G}_{\text{LO}}(\mathbf{p}_1, \mathbf{p}_2) + \tilde{\mu}_S^{2\varepsilon} \int \frac{d^n \mathbf{p}_3}{(2\pi)^n} \tilde{V}_{\text{LO}}(\mathbf{p}_1, \mathbf{p}_3) \tilde{G}_{\text{LO}}(\mathbf{p}_3, \mathbf{p}_2) = (2\pi)^n \delta^{(n)}(\mathbf{p}_1 - \mathbf{p}_2) . \tag{3.147}$$

This is just the Schrödinger equation in momentum space and G can be identified with its Green's function. Translating to position space with $n = 3$ it takes the more familiar form

$$(H_0 + V_{\text{LO}}(\mathbf{x}) - E) G_{\text{LO}}(\mathbf{x}, \mathbf{y}) = \delta^{(3)}(\mathbf{x} - \mathbf{y}) , \quad (3.148)$$

where $H_0 = -\nabla_x^2/m$. Rewriting Equation (3.144) with G_{LO} in position space, one thus finds that the matrix element \mathcal{A}_1 is proportional to the zero distance Green's function $G(\mathbf{0}, \mathbf{0})$ of the non-relativistic Schrödinger equation

$$\mathcal{A}_1 = 6N_c \lim_{|\mathbf{x}| \rightarrow 0} G(\mathbf{x}, \mathbf{0}) . \quad (3.149)$$

This equality holds at NLO and NNLO as well. Note that in the derivation of G_{LO} the exact form of the potential V was not needed. Since at NLO only the Coulomb potential and potential-like soft loops contribute, Equation (3.147) also holds at NLO. At NNLO, kinetic insertions start to contribute, which gives the NNLO Schrödinger equation:

$$\begin{aligned} & \left(\frac{\mathbf{p}_1^2}{m} - \frac{\mathbf{p}_1^4}{8m^3} - E \right) \tilde{G}_{\text{NNLO}}(\mathbf{p}_1, \mathbf{p}_2) + \\ & + \tilde{\mu}_S^{2\varepsilon} \int \frac{d^n \mathbf{p}_3}{(2\pi)^n} \tilde{V}_{\text{NNLO}}(\mathbf{p}_1, \mathbf{p}_3) \tilde{G}_{\text{NNLO}}(\mathbf{p}_3, \mathbf{p}_2) = (2\pi)^n \delta^{(n)}(\mathbf{p}_1 - \mathbf{p}_2) . \end{aligned} \quad (3.150)$$

LO Solution

At leading order, the solution of Equation (3.147) has already been obtained in the 1960s [60–62]. It reads

$$G_{\text{LO}}(\mathbf{x}, \mathbf{0}) = -i \frac{m^2 v}{2\pi} \int_0^\infty dt e^{imv|\mathbf{x}|(1+2t)} \left(\frac{1+t}{t} \right)^{\frac{i\alpha}{2v}} , \quad (3.151)$$

where v was defined in Equation (3.132). A derivation of this solution is given in Appendix C and it can also be easily checked by plugging $G_{\text{LO}}(\mathbf{x}, \mathbf{0})$ into the Schrödinger equation (3.148). The expansion for small $|\mathbf{x}|$ gives

$$\begin{aligned} G_{\text{LO}}(\mathbf{0}, \mathbf{0}) = \lim_{|\mathbf{x}| \rightarrow 0} \frac{m^2}{4\pi} & \left(\frac{1}{m|\mathbf{x}|} + iv \right. \\ & \left. - \alpha_s C_F \left[\log(m|\mathbf{x}|) + \log(-iv) + \psi \left(1 - \frac{i\alpha_s C_F}{2v} \right) + \gamma_E - \frac{1}{2} + \log 2 \right] \right) , \end{aligned} \quad (3.152)$$

where γ_E is the Euler-Mascheroni constant and $\psi(x) = \Gamma'(x)/\Gamma(x)$ the digamma function. The digamma function resums α_s/v terms to all orders, as can be seen from its expansion for $\alpha_s/v < 1$

$$\psi \left(1 - \frac{i\alpha_s C_F}{2v} \right) = -\gamma_E - i C_F \frac{\pi^2}{12} \frac{\alpha_s}{v} + C_F^2 \frac{\zeta(3)}{4} \frac{\alpha_s^2}{v^2} + \dots . \quad (3.153)$$

$G_{\text{LO}}(\mathbf{0}, \mathbf{0})$ is divergent. In Equation (3.152) the divergence is regulated with $|\mathbf{x}|$, which acts as a cutoff. In dimensional regularization, the power divergence vanishes and the term $\log(m|\mathbf{x}|)$ turns into a $1/\varepsilon$ divergence. Since the divergent term appears only at order α_s , it can be determined by calculating the $\mathcal{O}(\alpha_s)$ two-loop integral from Equation (3.142) in dimensional regularization.

The corresponding integral $I^{(2)}(1, 1, 1; Em)$ is solved in Appendix D and generates a divergent contribution of the form $\frac{\alpha_s C_F m^2}{16\pi\epsilon} + \frac{\alpha_s C_F m^2}{4\pi} \log(\mu/m) + \dots$.

G_{LO} in dimensional regularization therefore reads

$$G_{\text{LO}}(\mathbf{0}, \mathbf{0}) = \frac{m^2}{4\pi} \left(\frac{\alpha_s C_F}{4\epsilon} + iv - \alpha_s C_F \left[\log\left(\frac{-iv}{\nu}\right) + \psi\left(1 - \frac{i\alpha_s C_F}{2v}\right) + \gamma_E - \frac{1}{2} + \log 2 \right] \right), \quad (3.154)$$

where ν is the subtraction velocity defined by $\mu = m\nu$. At this point the type of regularization for $G_{\text{LO}}(\mathbf{0}, \mathbf{0})$ is not important for the final result, because the divergence appears only in the real part and therefore does not contribute to the cross section, see Equations (3.131) together with (3.149). This is also true at NLO. At NNLO, however, divergences appear also in the imaginary part and need to be renormalized in dimensional regularization.

Leading order electroweak effects can be implemented in Equation (3.154) by giving the energy from Equation (3.132) an imaginary part $E + i\epsilon \rightarrow E + i\Gamma_t$, where $\Gamma_t = 1.5 \text{ GeV}$ is the top width (see also Section 3.4.4). Figure 3.14 shows the cross section $\sigma_{\text{LO}} \sim \text{Im}[G_{\text{LO}}]$ with and without electroweak effects. In Figure 3.14a the cross section is continuously non-zero only above the threshold. This region corresponds to scattering states. Below threshold it has divergences at $\sqrt{s} = 2m - \frac{m\alpha_s^2 C_F^2}{4(1+n)^2}$ for $n = 0, 1, 2, 3, \dots$, which come from the digamma function and correspond to bound states of the $t\bar{t}$ pair.

However, when taking into account the top quark width, the poles are shifted away from the imaginary axis and the resonances smear out. Figuratively speaking, the $t\bar{t}$ pair decays before it can form a bound state and therefore no peaks appear in the leading order cross section in Figure 3.14b.

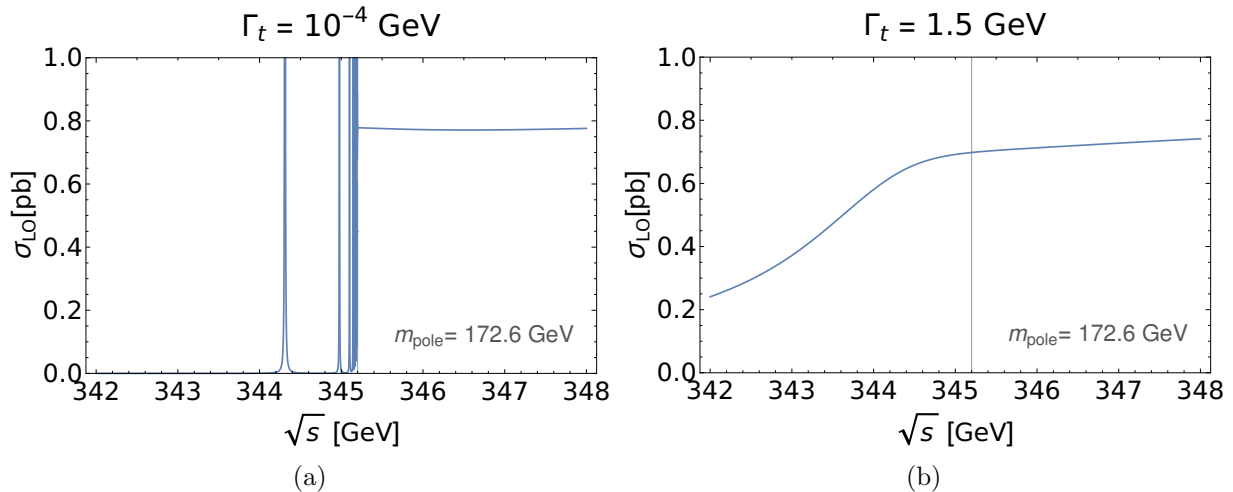


Figure 3.14: The leading order cross section σ_{LO} with a very small width (a) and the top width (b). The black horizontal line corresponds to $2m_t$.

NLO and NNLO Solution

At NLO and NNLO two kind of corrections appear. First, the Coulomb potential obtains α_s and α_s^2 corrections from soft loops and secondly, higher order potentials V_2, V_s, \dots as well as kinetic insertions start to contribute (see Equations (3.136)-(3.138)).

The higher order corrections to the Coulomb potential do not change the divergence structure of the Green's function. As for G_{LO} , the divergences are real and drop out for the inclusive cross

section. The contributions generated by $V_{c,\text{eff}}$ can therefore be resummed into the Coulomb Green's function $\tilde{G}_c(\mathbf{p}_1, \mathbf{p}_2)$ by solving the Schrödinger equation

$$\left(\frac{\mathbf{p}_1^2}{m^2} - E\right) \tilde{G}_c(\mathbf{p}_1, \mathbf{p}_2) + \tilde{\mu}_S^{2\varepsilon} \int \frac{d^n \mathbf{p}_3}{(2\pi)^n} \tilde{V}_{c,\text{eff}}(\mathbf{p}_1, \mathbf{p}_3) \tilde{G}_c(\mathbf{p}_3, \mathbf{p}_2) = (2\pi)^n \delta^{(n)}(\mathbf{p}_1 - \mathbf{p}_2) . \quad (3.155)$$

with the effective Coulomb potential $V_{c,\text{eff}}$.

An analytic solution for $\tilde{G}_c(\mathbf{p}_1, \mathbf{p}_2)$ at NLO and NNLO does not exist, but it can be calculated numerically by solving the Schrödinger equation. For this thesis, we use the program TOPPIK [63], which calculates the Coulomb Green's function numerically using a cutoff.

The other potentials and the kinetic insertions generate divergences that *do* affect the cross section and need to be renormalized in dimensional regularization. To see this, consider contributions to the cross section with insertions of the leading order Coulomb potential together with one insertion of the V_2 potential. Since the Green's function G_0 of the Schrödinger equation with the leading order Coulomb potential is known exactly, G_0 can be used to find solutions for the Green's function G_2 for the Schrödinger equation with the V_2 potential perturbatively. Similar to the perturbative expansion in Equation (C.5) from Appendix C, the first correction takes the form

$$\delta G_2(\mathbf{0}, \mathbf{0}) = - \lim_{|\mathbf{x}| \rightarrow 0} \int d^3 \mathbf{x}_1 G_{\text{LO}}(\mathbf{x}, \mathbf{x}_1) V_2(\mathbf{x}_1) G_{\text{LO}}(\mathbf{x}_1, \mathbf{0}) . \quad (3.156)$$

where $V_2(\mathbf{x}_1)$ is the Fourier transform of $\tilde{V}_2(\mathbf{p}, \mathbf{p}')$. Since $V_2(\mathbf{p}, \mathbf{p}')$ does not depend on the momentum, its Fourier transformation is

$$V_2(\mathbf{x}) = \frac{\mathcal{V}_2^{(s)}}{m^2} \delta^{(3)}(\mathbf{x}) \quad (3.157)$$

and Equation (3.156) therefore becomes

$$\begin{aligned} \delta G_2(\mathbf{0}, \mathbf{0}) &= \frac{\mathcal{V}_2^{(s)}}{m^2} \left[G_{\text{LO}}(\mathbf{0}, \mathbf{0}) \right]^2 \\ &= \mathcal{V}_2^{(s)} \frac{m^2}{16\pi^2} \left[\frac{\alpha_s C_F}{4\varepsilon} + iv + \dots \right]^2 . \end{aligned} \quad (3.158)$$

δG_2 has divergent imaginary parts, which need to be renormalized. They are canceled by the counterterms of the Wilson coefficient c_1 . The remaining quadratic divergence is real and drops out in the total cross section.

The NNLO order corrections δG_r , δG_s , δG_k , δG_{k1} , δG_{k2} and δG_{kin} coming from the other potentials, sum operators, and kinetic insertions, are calculated in a similar way and can be found in [41, 42, 47]. To resum the logarithms of the velocity v , the subtraction velocity ν is chosen to be of order $\nu \sim v$ and the full NNLL cross section with general ν then takes the form:

$$\sigma_{\text{vNRQCD}} = F(s) R(s) , \quad (3.159)$$

where

$$\begin{aligned}
F(s) &= \frac{4\pi}{s} Q_t^2 \sigma_{\text{pt}} \\
R(s) &= 6 N_c \text{Im} \left[2 c_1(\nu, h) c_2(\nu, h) v^2 G_c^{\text{LL}}(v, m, \nu, h) \right. \\
&\quad + c_1^2(\nu, h) \left(G_c^{\text{NNLL}}(v, m, \nu, h) + \delta G_2(v, m, \nu, h) + \delta G_s(v, m, \nu, h) \right. \\
&\quad \left. + \delta G_r(v, m, \nu, h) + \delta G_{\text{kin}}(v, m, \nu, h) + \delta G_{\text{k1}}(v, m, \nu, h) \right. \\
&\quad \left. \left. + \delta G_{\text{k2}}(v, m, \nu, h) + \delta G_{\text{k}}(v, m, \nu, h) \right) \right] .
\end{aligned} \tag{3.160}$$

Note that the notation used here is slightly different from [41, 42, 47]. Here the Wilson coefficients \mathcal{V}_i of the potentials are contained in the δG 's and δG_k includes the contributions coming from insertions of the sum operator \mathcal{O}_k (which corresponds to δG_{CF2} and δG_{CACF} in [41]).

Up to now, we have been working in the pole mass scheme and accordingly the mass m in Equation (3.159) is the pole mass. However, in QCD it is better to use a short-distance mass, as will be described in Chapter 4. We will use for σ_{vNRQCD} the 1S mass and in this massscheme, $R(s)$ will receive an additional contribution $\delta G_{1\text{S}}$ from the mass conversion, see Section 4.3.

3.4.4 Electroweak and Non-Perturbative Effects

In the last sections we mostly considered QCD contributions to the top quark pair production cross section. Electroweak effects, however, contribute already at LO and the finite lifetime of the top quark in particular is essential for obtaining a smooth lineshape (as shown in Figure 3.14). In the matching, we will consider only the leading order effects of the top width, which already give the bulk of all contributions.

We now give a short overview of the electroweak contributions at threshold. The electroweak coupling α_{EW} counts as

$$\alpha_{\text{EW}} \sim \alpha_s^2 \sim v^2 \tag{3.161}$$

and electroweak effects are therefore more suppressed than QCD effects.

Nevertheless, at LL there are already three different kinds of electroweak contributions: the finite width of the top quark, the intermediate γ or Z boson, and initial state QED effects from the e^+e^- pair. Initial state QED effects include initial state radiation, beamstrahlung, and beam energy spread. They are combined in the luminosity spectrum, which differs from collider to collider (see e.g. [9] for predictions of the luminosity spectrum at CLIC, ILC, and FCC-ee). They are included in the cross section by convoluting the luminosity spectrum with the theoretical calculation.

The intermediate particle producing the top quark pair can be either a photon or a Z boson. The bulk of all contributions comes from the γ induced cross section. The Z boson leads to small changes in the coupling of the vector current and induces an axial vector current, which is however v^2 suppressed and therefore only appears at NNLL.

The width of the top quark enters through the matching of the quark bilinear terms. Consider the one-loop self-energy contribution

$$-i\Sigma^0 = \text{---} \xrightarrow{t} \text{---} \xrightarrow{b} \text{---} \xrightarrow{t} \text{---} . \tag{3.162}$$

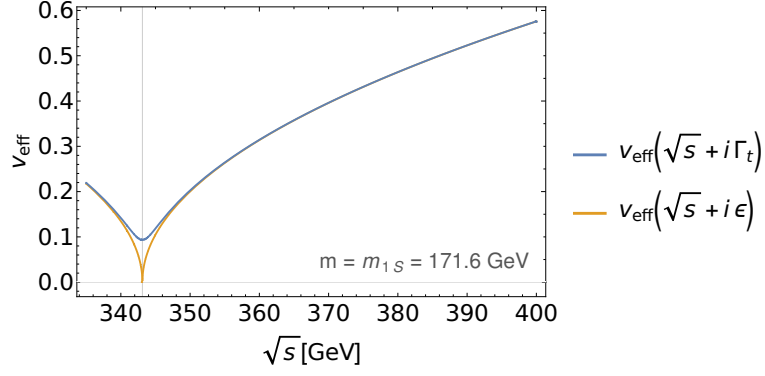


Figure 3.15: The effective velocity v_{eff} with and without the width Γ_t . Without Γ_t , the velocity is zero at threshold, but with Γ_t it is always non-zero.

The momentum in the loop is much larger than the scales $m_t v$ and $m_t v^2$ and therefore this diagram is integrated out in the effective theory. To match it to a bilinear quark term, we observe that the real part is absorbed into the pole mass definition, since we work with on-shell renormalization. The imaginary part, on the other hand, is related to the decay width of the top quark by the optical theorem, see Equation (A.8). With the non-relativistic renormalization $u\bar{u} = 1$ for the Dirac spinors, one gets

$$\text{Im} \left[\bar{u} \Sigma^0 u \right] = \frac{\Gamma_t}{2} . \quad (3.163)$$

This term is reproduced in the vNRQCD Lagrangian by

$$i \sum_{\mathbf{p}} \bar{\psi}_{\mathbf{p}} \frac{\Gamma_t}{2} \psi_{\mathbf{p}} . \quad (3.164)$$

Because $\Gamma_t = 1.5 \text{ GeV} \sim m v^2$, this term is of leading order in the Lagrangian and therefore contributes to the non-relativistic propagator. In loop diagrams contributing to the $t\bar{t}$ production cross section, the heavy quark propagator therefore takes the form

$$\frac{i}{\left(\frac{E}{2} \pm p^0 \right) - \frac{\mathbf{p}_s^2}{2m} + i \frac{\Gamma_t}{2}} , \quad (3.165)$$

where p^μ is the loop momentum and $E = \sqrt{s} - 2m$ the non-relativistic CM energy. In practice, the width can be implemented in the vNRQCD calculations of the previous chapters by a simple prescription. Observing that Γ_t and E only appear in the heavy quark propagators, the width can be included in the results for the cross section from Equation (3.159)-(3.160) by

$$\sqrt{s} + i\epsilon \rightarrow \sqrt{s} + i\Gamma_t , \quad (3.166)$$

which was first realized in [64]. The implementation of the width at leading order is crucial, since it leads to large changes in the cross section by smearing out the bound state resonance states. It is also essential for suppressing non-perturbative effects, since it renders the effective velocity

$$v_{\text{eff}}(\sqrt{s} + i\Gamma_t) = \left| \sqrt{\frac{(\sqrt{s} + i\Gamma_t) - 2m}{m}} \right|$$

finite even at threshold, see Figure 3.15. Non-perturbative effects are therefore estimated to be tiny ($\delta\sigma/\sigma \sim 10^{-4}$) [65–68] and can be neglected (uncertainties in the NNLL cross section due to scale variations are larger than 10^{-2} , see Figure 3.20).

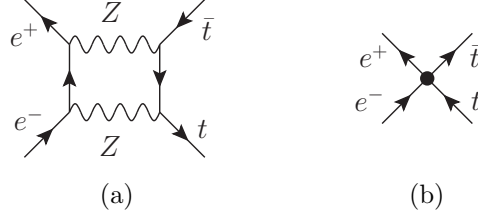


Figure 3.16: Example of an electroweak correction at NNLL: the full theory diagram (a) contains two Z bosons, which are integrated out in the EFT, giving the 4-fermion vertex (b).

At NLL and NNLL, effects from additional insertions of the W boson, Z boson, and the photon come into play. At NLL, exchanges of Coulomb photons lead to similar effects as from the exchange of Coulomb gluons. At NNLL, electroweak one-loop corrections to $e^+e^- \rightarrow t\bar{t}$ appear (see for example Figure 3.16a) and have to be integrated out, giving the 4-fermion vertex in Figure 3.16b. Interesting implications arise from the large top quark decay width. Since the top decays almost instantly into W^+b , the experimentally measured final state is not $t\bar{t}$, but rather $W^+b W^- \bar{b}$. Therefore also diagrams with a single on-shell top quark have to be considered (e.g. Figure 3.17b). The top quark decay is integrated out in the EFT, giving imaginary contributions to the Wilson coefficients from Figure 3.16b [69]. The effects described above apply to top-quarks near their mass-shell. However, also off-shell top quarks can contribute, giving so-called non-resonant effects at NLL and NNLL order [70, 71].

For details on the higher order electroweak contributions see [69–73].

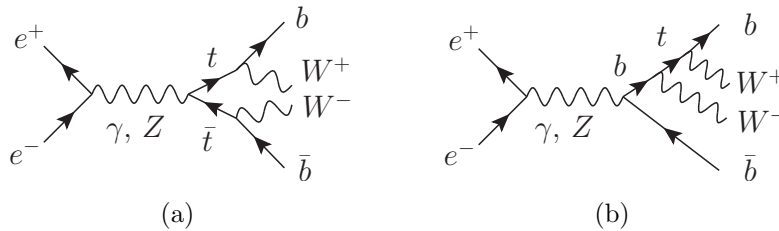


Figure 3.17: Diagrams with the final state $bW^+ \bar{b}W^-$. While (a) is double-resonant, (b) contains only one top quark.

3.5 Analysis of the Threshold Contributions

For the matching we will consider the photon induced double-resonant $t\bar{t}$ production cross section with NNLL QCD effects, and LO electroweak contributions at threshold. The NNLL order QCD contributions are computed with Equation (3.159) and (3.160), and the LO electroweak effects are included with the prescription given in Equation (3.166). The contributions $R(s)$ to the cross section at LL, NLL, and NNLL order then read

$$\begin{aligned}
R_{\text{LL}}(s) &= 6N_c \text{Im} \left[(c_1^{\text{LL}})^2 G_c^{\text{LL}} \right] \\
R_{\text{NLL}}(s) &= 6N_c \text{Im} \left[(c_1^{\text{NLL}})^2 G_c^{\text{NLL}} \right] \\
R_{\text{NNLL}}(s) &= 6N_c \text{Im} \left[2 c_1^{\text{LL}} c_2^{\text{LL}} + (c_1^{\text{NNLL}})^2 G_c^{\text{NNLL}} \right. \\
&\quad \left. + (c_1^{\text{LL}})^2 \left(\delta G_2 + \delta G_s + \delta G_r + \delta G_{\text{kin}} + \delta G_k + \delta G_{k1} + \delta G_{k2} \right) \right]
\end{aligned} \tag{3.167}$$

where the superscripts on G_c denote the order of the Coulomb potential in the Green's function and the superscripts on c_1, c_2 stand for the order of the running and the power of α_s included, e.g.

$$\begin{aligned}
c_1^{\text{LL}} &= 1 \\
c_1^{\text{NLL}} &= \left(1 - \frac{2C_F}{\pi} \alpha_s(\mu_h) \right)^2 \exp [\xi^{\text{NLL}}(h, \nu)] \\
&= \left(1 - \frac{4C_F}{\pi} \alpha_s(\mu_h) + \mathcal{O}(\alpha_s^3) \right) \exp [\xi^{\text{NLL}}(h, \nu)] .
\end{aligned} \tag{3.168}$$

c_1^{NNLL} is expanded in the same way up to α_s^3 . This choice for c_1 is not unique and we discuss different choices at the end of this section. Both the Wilson coefficients c_1, c_2 and the Green's functions depend on h and ν . h describes the variation of the matching scale μ_h and ν the variation of the renormalization scales μ_S and μ_U . The renormalization scales are related to the matching scale by

$$\mu_S = \nu \mu_h , \quad \mu_U = \nu^2 \mu_h , \tag{3.169}$$

where ν is called "subtraction velocity". These relations ensure that $\mu_S^2 \sim \mu_U$ is fulfilled at all times. With $\mu_h = hm$, the scales take the form

$$\mu_h = hm , \quad \mu_S = hm \nu , \quad \mu_U = hm \nu^2 . \tag{3.170}$$

h and ν can be used to estimate the theoretical error of σ_{vNRQCD} . The cross section is independent of ν and h when including all powers in α_s and v . Taking only the contributions up to NNLL, the cross section will exhibit a ν and h dependence, which has to cancel with the (unknown) higher order corrections. By varying ν and h , the size of the missing corrections can be estimated. The values for h and ν are restricted, because they have to be chosen such that they neither produce large logarithms nor make the coupling α_s non-perturbative.

In this work two different choices for ν are considered: $\nu \sim v$ resums logarithms of the velocity v to all orders through the renormalization group running of the potentials and the production current. We therefore call $\sigma_{\text{vNRQCD}}(\nu \sim v)$ the renormalization-group-improved (RGI) cross section. We also consider $\nu = 1$, which switches the resummation of logarithms off. We therefore call $\sigma_{\text{vNRQCD}}(\nu = 1)$ the fixed-order (FO) cross section.

RGI Cross Section

The RGI cross section resums large logarithms of v to all orders. To estimate the theoretical error we use scale variations as presented in [57]. At threshold we have the three scales μ_h , μ_S , and μ_U with the default values

$$\mu_h^{\text{def}} = m, \quad \mu_S^{\text{def}} = m\nu, \quad \mu_U^{\text{def}} = m\nu^2, \quad (3.171)$$

where $\nu = f \nu_*$ and ν_* is related to the effective velocity:

$$\nu_* = 0.05 + \left| \sqrt{\frac{\sqrt{s} - 2m + i\Gamma_t}{m}} \right|, \quad (3.172)$$

The small constant offset of 0.05 is motivated in [56, 57]. The dependence of ν_* on the CM energy \sqrt{s} is shown in Figure 3.18.

Since μ_S and μ_U are correlated, only μ_h and either μ_S or μ_U can be varied independently. We choose to vary μ_h and μ_U between 1/2 and 2:

$$\begin{aligned} \frac{1}{2} \mu_h^{\text{def}} < \mu_h < 2 \mu_h^{\text{def}} \\ \frac{1}{2} \mu_U^{\text{def}} < \mu_U < 2 \mu_U^{\text{def}}. \end{aligned} \quad (3.173)$$

For h and ν this translates to

$$\begin{aligned} \frac{1}{2} < h < 2 \\ \frac{1}{2} < hf^2 < 2, \end{aligned} \quad (3.174)$$

where $h = 1$, $f = 1$ give the default values from Equation (3.171). The values covered by these conditions are shown in Figure 3.19. μ_U is chosen such that the coupling $\alpha_s(\mu_U)$ does not become non-perturbative. With Equation (3.174), the lowest value of μ_U is $(\nu_*^{\text{min}})^2 (1/2) m \sim 0.14^2 \cdot 0.5 \cdot 170 \sim 1.7 \text{ GeV}$, for which the ultrasoft coupling is $\alpha_s(\mu_U = 1.7) \sim 0.27$. Smaller values of h and f would make the coupling even larger and spoil the perturbative expansion in $\alpha_s(\mu_U)$.

The RGI cross section in the 1S mass scheme is shown in Figure 3.20b (for a discussion of the mass schemes see Chapter 4).

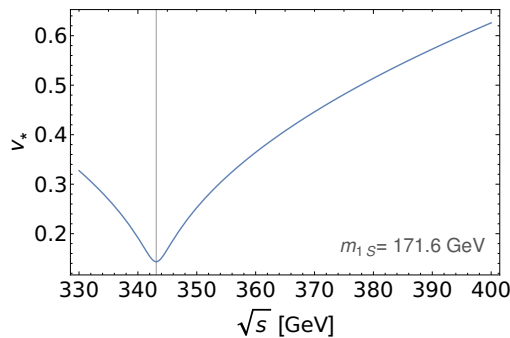


Figure 3.18: Dependence of ν_* on the CM energy \sqrt{s} .

Fixed Order Cross Section

The RG running of the Wilson coefficients resums logarithms of $\log(\mu_h/\mu_S)$ and $\log(\mu_h/\mu_U)$ to all orders in α_s . For the fixed-order (FO) cross section we do not use this resummation and therefore choose

$$\mu_h = \mu_S = \mu_U . \quad (3.175)$$

This leaves only one scale, the matching scale $\mu_h = hm$, to estimate the theoretical error.

When choosing a value for μ_h , two effects have to be considered. On the one hand, the large logarithms of $\log(\mu_h/\mu_S)$ can be partially resummed by the running of the strong coupling constant. At LL, the only coefficient with an RG running is the LL Coulomb potential and it is determined fully by the running of α_s (see Equation (3.114)). By choosing $\mu_h \sim mv$ all large logarithms are resummed at this order.

At NLL, the matrix element \mathcal{A}_1 includes again only terms whose running is determined by $\alpha_s(\mu_S)$. However, its Wilson coefficient c_1 depends on μ_h , μ_S , and μ_U , and the large logarithms can not be resummed into c_1 by choosing $\mu_h \sim \mu_S \sim mv$. Finally, at NNLL order the matrix element \mathcal{A}_1 includes the higher order potentials, which have soft as well as ultrasoft running. The logarithms are therefore not fully resummed neither in the matrix elements nor in c_1 and c_2 .

On the other hand, if the scale μ_h becomes smaller, $\alpha_s(\mu_h)$ gets larger, which degrades the convergence of the perturbative series. The missing higher order logarithms will therefore become even larger and lower the accuracy of the calculated terms.

As a compromise between the partial resummation of large logarithms into the coupling constant for $\mu_h \sim hm\nu_*$ and the small coupling at $\mu_h \sim hm$, we choose the geometric mean of the two scales:

$$\mu_h = hm\sqrt{\nu_*} , \quad 1/2 < h < 2 , \quad (3.176)$$

where h is varied to estimate the theoretical error.

The fixed-order cross section at order LO, NLO, and NNLO is shown in Figure 3.20a. At LO and NLO the error band is thinner than the corresponding one of the RGI cross section. This occurs, because the coupling $\alpha_s(\mu)$ and therefore also the cross section, vary more strongly at small scales μ . This can be seen from the leading-order cross section, which only depends on one scale, μ_S . The value for the scale $\mu_S = \mu_h = mh\sqrt{\nu_*}$ is larger than the corresponding RGI value $\mu_S = hm\nu_*$. Correspondingly, the scale variations are larger for the RGI cross section. At NLO the situation is similar. At NNLO, however, a large part of the logarithms resummed in the RGI cross section is not included in the fixed-order cross section, leading to the larger error band of the fixed-order cross section when compared to the RGI cross section.

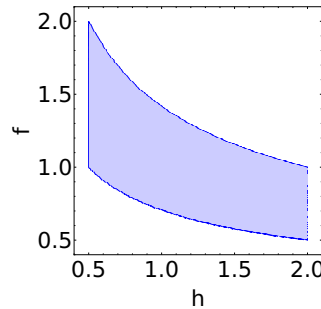


Figure 3.19: Values for h and f covered by Equation (3.174).

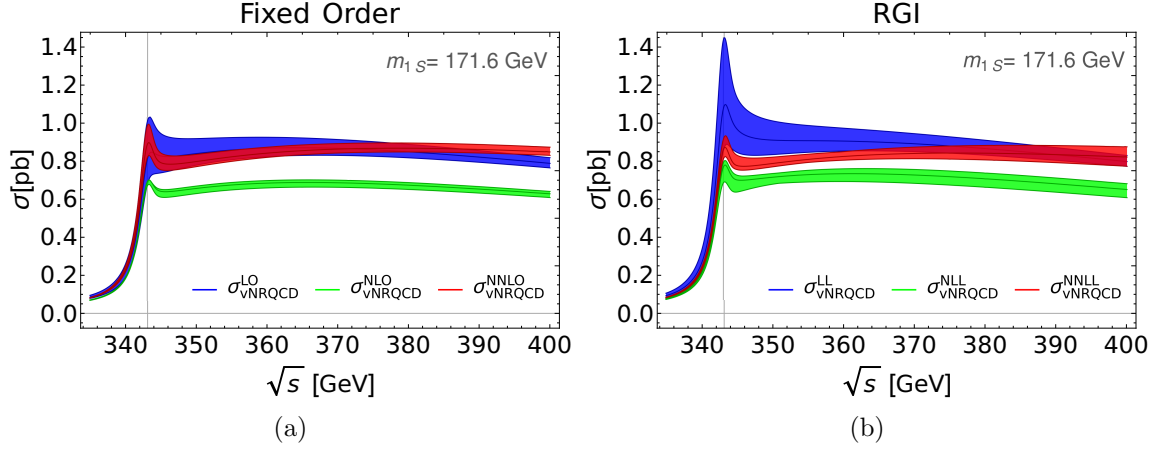


Figure 3.20: vNRQCD cross section in the 1S mass scheme: (a) fixed-order cross section at order LO, NLO, and NNLO and (b) RGI cross section at order LL, NLL, and NNLL.

Comparison of Choices for the Current Wilson Coefficient c_1^2

In Equation (3.167) we expanded c_1^2 in α_h such that no higher order terms beyond NLL or NNLL were generated. At threshold, c_1^2 could instead also be left unexpanded. For the matching, however, the expanded version is needed.

If at every order the highest order of c_1 is used, $R(s)$ from Equation (3.167) takes the form

$$\begin{aligned}
 R_{\text{LL}}(s) &= 6N_c \text{Im} \left[(c_1^{\text{LL}})^2 G_c^{\text{LL}} \right] \\
 R_{\text{NLL}}(s) &= 6N_c \text{Im} \left[(c_1^{\text{NLL}})^2 G_c^{\text{NLL}} \right] \\
 R_{\text{NNLL}}(s) &= 6N_c \text{Im} \left[2c_1^{\text{NNLL}} c_2^{\text{LL}} + (c_1^{\text{NNLL}})^2 G_c^{\text{NNLL}} \right. \\
 &\quad \left. + (c_1^{\text{NNLL}})^2 \left(\delta G_2 + \delta G_s + \delta G_r + \delta G_{\text{kin}} + \delta G_k + \delta G_{k1} + \delta G_{k2} \right) \right] \quad (3.177)
 \end{aligned}$$

where $(c_1^{\text{NNLL}})^2$ and $(c_1^{\text{NLL}})^2$ are left unexpanded and therefore produce terms of order $(1, \alpha_h, \alpha_h^2)$ and $(1, \alpha_h, \alpha_h^2, \alpha_h^3, \alpha_h^4)$, respectively. This generates order terms up to order N⁴LO. The higher order term can be an advantage since c_1 contains factorized long-distance contributions and one could expect that including all known contributions up to c_1^2 reduces the theoretical error of the cross section. The form given in Equation (3.177) was used in [57] to estimate the NNLL uncertainties of the top quark pair production cross section at threshold for a future linear colliders.

At threshold, we are free to choose the expanded or unexpanded version of c_1^2 . For the matching, however, using the unexpanded coefficient with the terms beyond NNLL leads to problems. Consider for example the contribution $(c_1^{\text{NNLL}})^2 \delta G_{\text{kin}}$ to the cross section. δG_{kin} generates NNLL contributions of the form $v^3, v^2\alpha_s, v\alpha_s^2, \dots$. Multiplying with $(c_1^{\text{NNLL}})^2$ then gives a term of order $\alpha_s v^3$, for example. At threshold, we have $\alpha_s \sim v \sim 0.15$ and therefore $\alpha_s v^3 \sim 5 \cdot 10^{-4}$, which is of N³LL order. In the intermediate region however, v becomes large and for $v \sim 0.5$ the contribution is of order $v^3\alpha_s \sim 2 \cdot 10^{-2}$, which is already NLL order.

Note that the $\alpha_s v^3$ term generated by $(c_1^{\text{NNLL}})^2$ is not the full $\alpha_s v^3$ contribution to the cross section. Therefore this term would have to be subtracted in the matched cross section, and all other terms beyond NNLL with v^i with $i = 1, 2, 3$ as well (terms of the form of e.g. α_s^5/v are not a problem above threshold, since they get smaller for larger v and are therefore in the intermediate region even *more* suppressed than at threshold).

Instead of subtracting the terms beyond NNLL, one can also expand c_1^2 in α_s to ensure they are not generated in the first place. For the corrections to the Green's function $\delta G_{\text{kin}}, \delta G_k, \dots$ this means that $c_1^{\text{expanded}} = 1$, since the Green's function corrections are already of NNLL order. Additionally, the coefficients c_1^2 multiplying the Coulombic Green's function G_c need to be expanded. The resulting contributions then take the form presented in Equations (3.167) and (3.168). This is the form we will use for the matching.

A comparison of the cross section with the full and the expanded implementation of the Wilson coefficient c_1^2 is shown in Figure 3.21 for both the fixed-order and the RGI setting. The leading order cross section is not shown, since it is the same for both cases. At NLL the difference between the full and the expanded implementation of the Wilson coefficient is very small. At NNLL, however, the difference is large and for the fixed-order cross section the error bands of the two versions even have no overlap at all above ~ 378 GeV. The large change comes mainly from changing the Wilson coefficients multiplying the Green's function corrections δG from c_1^{NNLL} to c_1^{LL} . For the RGI cross section, including more long-distance contributions by using the full Wilson coefficients reduces the error band slightly at threshold, but leaves the form at threshold otherwise unchanged. Both in the fixed-order as well as the RGI setting, the curves with the expanded and full Wilson coefficient, respectively, start to differ soon after the peak region. For the fixed-order cross section, the difference is clearly visible directly after the peak and for the RGI cross section, the curves start to differ at $\sqrt{s} \sim 352$ GeV ($v \sim 0.2$), indicating that higher order contributions become sizeable. This suggests, that above 352 GeV we will very likely need the matched cross section, which includes higher order contributions beyond NNLL.

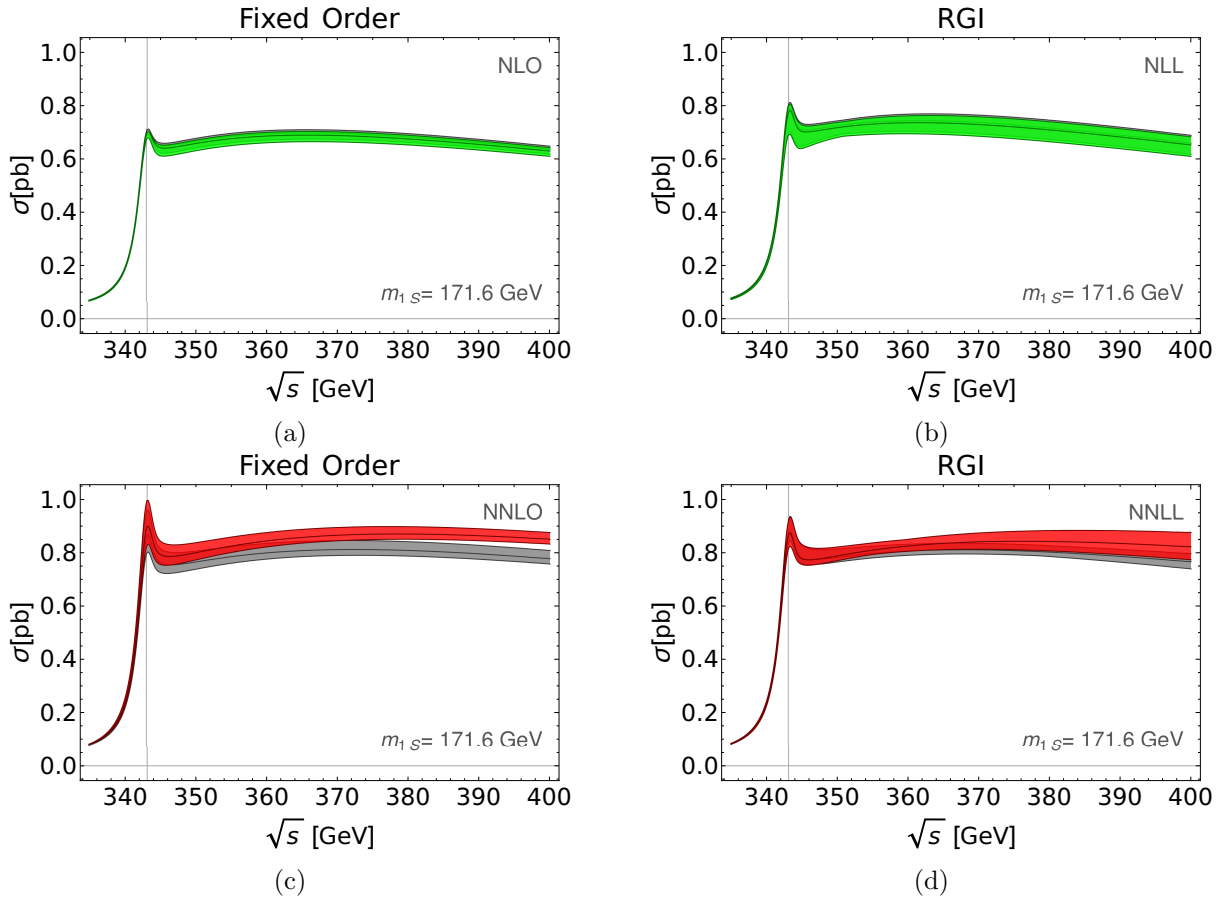


Figure 3.21: Comparison of the cross section with the full contributions from the Wilson coefficient c_1^2 (gray) and the expanded version of c_1^2 (green and red, respectively) for the fixed-order cross section (left) and the RGI cross section (right). All plots are in the 1S mass scheme.

Chapter 4

Mass Schemes

In most areas of physics the mass of a particle is a fixed concept and it is typically identified with the rest mass. In QFT, however, masses are defined by renormalization and different renormalization schemes give different values for the mass of a particle. For physical observables, it should of course not matter, which mass scheme is chosen in the calculation. A change between mass schemes just reorganizes the perturbation series of the observable, leaving the observable itself unchanged. It can, however, affect the convergence of the perturbation series. Since we can usually only calculate the first few terms in the perturbation series, it is important to choose the mass scheme carefully.

In this chapter four different mass scheme are described: the pole mass, $\overline{\text{MS}}$ mass, 1S mass, and MSR mass. The pole mass corresponds most closely to the physical rest mass, but it is sensitive to the IR region, which causes a rapid divergence in its relation to the bare mass and to short distances masses [74, 75]. This divergent behavior is called renormalon and it not only causes a bad convergence in the perturbation series of physical observables, but also leads to an intrinsic ambiguity of the pole mass of order Λ_{QCD} .

Masses free of the renormalon are called short-distance masses. An example is the $\overline{\text{MS}}$ mass, which is well-suited for calculations in the continuum. At threshold, however, it breaks the power counting in v . Instead, so-called "threshold masses", which are specifically designed for threshold application, have to be used. Examples are the 1S mass [63, 76, 77], the PS mass [78], and the kinetic mass [79].

For the matching a mass scheme is needed, that is renormalon-free and can be used both at threshold and in the continuum. We choose the MSR mass for this purpose. The MSR mass depends on an adjustable scale R , which can be used to interpolate between a threshold mass at low scales and the $\overline{\text{MS}}$ in the continuum.

4.1 Pole Mass

The pole mass is closely related to the physical mass of a particle, since it corresponds to the pole in the full propagator S_F . S_F in terms of the bare mass m_0 and the one particle-irreducible self-energy contributions Σ reads

$$S_F = \frac{i}{\not{p} - m_0 + \Sigma(\not{p}, m_0)} . \quad (4.1)$$

The pole mass m_{pole} is defined as the pole of the propagator [14]:

$$\not{p} - m_0 + \Sigma(\not{p}, m_0) \Big|_{p^2 = m_{\text{pole}}^2} = 0 . \quad (4.2)$$

m_{pole} not only absorbs UV divergences, but also finite contributions from the self-energy Σ . To study the finite contributions, consider the relation of the pole mass to the $\overline{\text{MS}}$ mass. Since the $\overline{\text{MS}}$ mass only contains the UV divergent contributions of Σ , $m_{\text{pole}} - m_{\overline{\text{MS}}}$ provides insight into

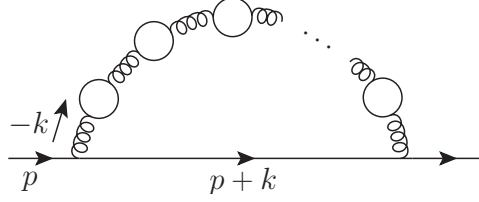


Figure 4.1: Self-energy diagram containing a chain of fermion bubbles.

the behaviour of the finite terms. To illustrate their behaviour at large orders in α_s , consider the bubble-chain (see Figure 4.1) contributions to Σ [80]. Replacing $-2n_f/3 \rightarrow \beta_0$ to include non-abelian contributions (known as naive non-Abelization), they give the following contribution to $m_{\text{pole}} - m_{\overline{\text{MS}}}(\mu)$ [80]:

$$m_{\text{pole}} - m_{\overline{\text{MS}}}(\mu) = -i C_F g^2 \tilde{\mu}^{2\epsilon} \sum_{n=0}^{\infty} \int \frac{d^d k}{(2\pi)^d} \left(\frac{\beta_0 \alpha_s(\mu)}{4\pi} \right)^n \log \left(-\frac{\mu^2 e^{5/3}}{k^2} \right)^n \frac{\gamma^\mu (\not{p} + \not{k} + m_{\overline{\text{MS}}}) \gamma_\mu}{((p+k)^2 - m_{\overline{\text{MS}}}^2) k^2} \Big|_{p^2 = m_{\text{pole}}^2}, \quad (4.3)$$

where $m_{\overline{\text{MS}}}$ is the $\overline{\text{MS}}$ mass and $\beta_0 = 11 - 2n_f/3$. For large n , the logarithm enhances contributions from small and large k to the integrand. For small k , the integrand scales as $dk k^3/k^3$ and the logarithm enhances the contributions in the IR region. Expanding in small k and performing the integral, the divergent behaviour becomes apparent [80]

$$m_{\text{pole}} - m_{\overline{\text{MS}}}(\mu) = e^{5/6} \mu \frac{C_F \alpha_s}{\pi} \sum_{n=0}^{\infty} \left(\frac{\alpha_s \beta_0}{2\pi} \right)^n n!. \quad (4.4)$$

This factorial pattern of divergence is known as IR renormalon (UV renormalons also exist - they have a negative sign in the $(\alpha_s \beta_0/(2\pi))^n$ term). It often leads to a bad convergence of the perturbative expansion already at low orders, which is also the case for the top quark production cross section at threshold. Additionally, it can be shown that the divergent behaviour of Equation (4.4) leads to an intrinsic ambiguity of order Λ_{QCD} in the pole mass [80]. Since the renormalon appears in the finite self-energy contributions absorbed by the pole mass, it is an intrinsic problem of the pole mass. The $\overline{\text{MS}}$ mass and other short-distance masses are free of renormalons and they all exhibit the large order asymptotic behaviour shown in Equation (4.4) when they are related to the pole mass.

In Figure 4.3 the RGI vNRQCD cross section is shown in the pole mass scheme and the 1S mass scheme. The peak position is very sensitive to the top quark mass and will be used to determine the top quark mass to high precision at future linear colliders. In the pole mass scheme, however, the peak position shows a large variation from order to order. From NLL to NNLL it varies by

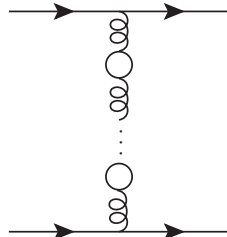


Figure 4.2: Fermion bubble chain contributing to the potential $V(\mathbf{x})$.

500 MeV, which is much larger than the expected experimental precision of below 100 MeV at a future linear collider. Luckily, the large uncertainty is not intrinsic to σ_{vNRQCD} , but rather induced by the renormalon of the pole mass. To see this, consider the terms

$$H_0 - V(\mathbf{x}) + E = H_0 - V(\mathbf{x}) + \sqrt{s} + 2 m_{\text{pole}} . \quad (4.5)$$

that appear in the non-relativistic Schroedinger equation (Equation (3.148)). The potential $V(\mathbf{x})$ has a renormalon ambiguity similar to the pole mass. To see this, consider the contributions to $V(\mathbf{x})$ generated by the bubble chain shown in Figure 4.2. Although the potential at lowest order depends on $1/|\mathbf{x}|$, the contributions become independent of $|\mathbf{x}|$ at large orders and behave asymptotically for n fermion loops as [49]

$$- 2 e^{5/6} \mu \frac{C_F \alpha_s}{\pi} \left(\frac{\alpha_s \beta_0}{2\pi} \right)^n n! . \quad (4.6)$$

$V(\mathbf{x})$ therefore has a similar asymptotic large order behaviour as $(m_{\text{pole}} - m_{\overline{\text{MS}}})$ from Equation (4.4), or more generally, as $(m_{\text{pole}} - m_{\text{sd}})$, where m_{sd} is a short-distance mass. Rewriting the pole mass as $m_{\text{pole}} = m_{\text{sd}} + \delta m$, where δm contains the renormalon with the large order behaviour of Equation (4.4), the sum of the potential and the pole mass from Equation (4.5) becomes

$$V(\mathbf{x}) + 2(m_{\text{sd}} + \delta m) \quad (4.7)$$

and the renormalon ambiguity cancels between $V(\mathbf{x})$ and δm (see Equations (4.4) and (4.6)). Thus the manifestation of the renormalon from Figure 4.3a can be avoided in the $t\bar{t}$ production cross section by using a short-distance mass m_{sd} . In Figure 4.3b the RGI vNRQCD cross section is shown in the 1S scheme, which is a low-scale short distance mass scheme. The large variation from order to order has vanished for the 1S scheme and the peak position is stable.

For the short-distance mass, we will use at threshold the 1S mass and MSR mass, and in the continuum the $\overline{\text{MS}}$ mass.

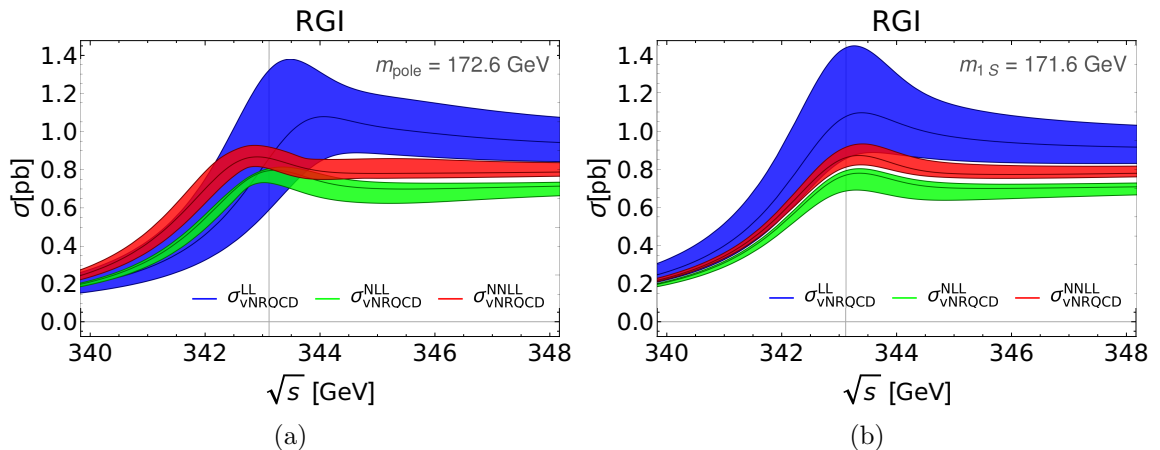


Figure 4.3: vNRQCD cross section in the pole mass scheme (a) and the 1S scheme (b). The vertical line denotes the threshold at $2m_{1S}$.

4.2 $\overline{\text{MS}}$ Mass

The $\overline{\text{MS}}$ mass only absorbs the divergent terms from the self-energy diagrams. The denominator of the full propagator therefore takes the form

$$\not{p} - m_0 + \Sigma = \not{p} - m_{\overline{\text{MS}}} + \Sigma_{\text{finite}} . \quad (4.8)$$

Together with Equation (4.2), the perturbative relation to the pole mass can be obtained. It reads:

$$m_{\text{pole}} = \overline{m} + \overline{m} \sum_{n=1}^{\infty} a_n(n_l, n_h) \left(\frac{\alpha_s^{(n_f)}(\overline{m})}{4\pi} \right)^n . \quad (4.9)$$

where \overline{m} is a shorthand notation for the $\overline{\text{MS}}$ mass evaluated at $\mu = m_{\overline{\text{MS}}}$:

$$\overline{m} = m_{\overline{\text{MS}}}(\mu = m_{\overline{\text{MS}}}) . \quad (4.10)$$

The coefficients contain contributions from the self-energy diagrams with $n_h = 1$ heavy quarks n_l light (massless) quarks. The coupling α_s runs with $n_f = n_h + n_l$ flavors. The relation has been calculated up to 4-loop order [81–88]. a_1 , a_2 , and a_3 are known analytically, while a_4 has been obtained numerically. A summary of the coefficients can be found in [89].

The $\overline{\text{MS}}$ mass is well-suited for calculations in the continuum. At threshold, however, it breaks the power counting. To see this, consider the full propagator of a heavy quark with the non-relativistic energy $E_{\text{pole}} = \sqrt{s}/2 - m_{\text{pole}}$ [49]

$$\frac{i}{E_{\text{pole}} - \mathbf{p}^2/2m_{\text{pole}} + \mathbf{p}^4/8m_{\text{pole}}^3 + \dots} , \quad (4.11)$$

which is calculated from the vNRQCD effective Lagrangian. In Section 3.3 m was the pole mass, since on-shell renormalization is well-suited for the matching and renormalization [49]. Changing to the $\overline{\text{MS}}$ mass with $m_{\text{pole}} = \overline{m} + \delta m$, the denominator of the full propagator takes the form

$$E_{\overline{\text{MS}}} - \delta m - \frac{\mathbf{p}^2}{2\overline{m}} + \frac{\delta m}{\overline{m}} \frac{\mathbf{p}^2}{2\overline{m}} + \frac{\mathbf{p}^4}{8\overline{m}^3} + \dots , \quad (4.12)$$

where $E_{\overline{\text{MS}}} = \sqrt{s}/2 - \overline{m}$. $E_{\overline{\text{MS}}}$ and $\mathbf{p}^2/2m$ are both of order $mv^2 \sim m\alpha_s^2$. The first order correction δm , in contrast, is of order $m\alpha_s$. It is therefore much larger than the leading order terms, should not be counted as a perturbation and therefore breaks the power counting.

Another way to see the power breaking explicitly is to change the mass scheme of the terms in σ_{vNRQCD} . Consider the contribution $v_{\text{pole}} = \sqrt{(\sqrt{s} - 2m_{\text{pole}})/m_{\text{pole}}}$ to σ_{vNRQCD} , which contributes at leading order, see Equation (3.135). Converting v_{pole} to the $\overline{\text{MS}}$ scheme with Equation (4.9) and using $A_s = \alpha_s^{(n_f)}(\overline{m})/4\pi$, the velocity in the pole mass scheme transforms into

$$\begin{aligned} v_{\text{pole}} &= \sqrt{\frac{\sqrt{s} - 2m_{\text{pole}}}{m_{\text{pole}}}} = \sqrt{\frac{\sqrt{s} - 2(\overline{m} + \overline{m} a_1 A_s)}{\overline{m} + \overline{m} a_1 A_s}} \\ &= v_{\overline{\text{MS}}} - A_s a_1 \left(\frac{v_{\overline{\text{MS}}}}{2} + \frac{1}{v_{\overline{\text{MS}}}} \right) + A_s^2 a_1^2 \left(\frac{3v_{\overline{\text{MS}}}}{8} + \frac{1}{2v_{\overline{\text{MS}}}} - \frac{1}{2v_{\overline{\text{MS}}}^3} \right) + \mathcal{O}(A_s^3) , \end{aligned} \quad (4.13)$$

where $v_{\overline{\text{MS}}} = \sqrt{(\sqrt{s} - 2\overline{m})/\overline{m}}$ and only the first order correction $\overline{m} A_s a_1$ to the mass was used. Higher order corrections of the mass give similar contributions.

A good mass scheme should only generate contributions that are of the same order in α_s and v as the original term, and additionally subleading contributions. For the conversion above, however, v_{pole} generates terms of order $\alpha_s/v_{\overline{\text{MS}}}$, $\alpha_s^2/v_{\overline{\text{MS}}}^2$, \dots , which are *larger* than the leading order terms. This is a manifestation of the power counting breaking and makes $\overline{\text{MS}}$ unusable at threshold. These contributions can be avoided in a short distance mass scheme, which has a first order correction of order $\delta m \sim m_{\text{sd}} \alpha_s^2$ in its relation to the pole mass. The conversion of the velocity takes the form

$$\begin{aligned} v_{\text{pole}} &= \sqrt{\frac{\sqrt{s} - 2(m_{\text{sd}} + m_{\text{sd}} a_1 A_s^2)}{m_{\text{sd}} + m_{\text{sd}} a_1 A_s^2}} \\ &= v_{\text{sd}} - A_s^2 a_1 \left(\frac{v_{\text{sd}}}{2} + \frac{1}{v_{\text{sd}}} \right) + A_s^3 a_1^2 \left(\frac{3v_{\text{sd}}}{8} + \frac{1}{2v_{\text{sd}}} - \frac{1}{2v_{\text{sd}}^3} \right) + \mathcal{O}(A_s^4) , \end{aligned} \quad (4.14)$$

which has only leading order terms (v , A_s , A_s^2/v , \dots) and subleading contributions. We will use as the low-energy short-distance mass the 1S mass.

4.3 1S Mass

To construct a renormalon-free threshold mass with $\delta m \sim m \alpha_s^2$ in the relation to the pole mass at lowest order, the potential $V(\mathbf{x})$ can be used, because it has a renormalon ambiguity similar to the one of the pole mass.

For stable quarks ($\Gamma_t = 0$), the binding energy E_{bin} of the heavy quark-antiquark pair in the spin-triplet ground state can be calculated from the potential. E_{bin} contains the renormalon, which cancels in the sum of the binding energy with $2m_{\text{pole}}$:

$$M_{t\bar{t}}^{3S1} = E_{\text{bin}} + 2m_{\text{pole}} , \quad (4.15)$$

$M_{t\bar{t}}^{3S1}$ is the physical mass of the $t\bar{t}$ system up to non-perturbative corrections [49] and renormalon-free. The 1S mass of the top quark is then defined as half the mass of the entire system [63, 76, 77]:

$$m_{1\text{S}} = \frac{1}{2} M_{t\bar{t}}^{3S1} = m_{\text{pole}} + \frac{1}{2} E_{\text{bin}} . \quad (4.16)$$

Since $E_{\text{bin}} \sim mv^2 \sim m \alpha_s^2$ at threshold, the first order correction in the relation to the pole mass is of order $m \alpha_s^2$ and complies with the non-relativistic power counting. E_{bin} can be calculated perturbatively from the Schroedinger equation using time-independent perturbation theory and is known up to NNLL order [40], where the $E_{\text{bin}}^{\text{LL}}$ contribution involves the LL Coulomb potential, the $E_{\text{bin}}^{\text{NLL}}$ the NLL Coulomb potential, and $E_{\text{bin}}^{\text{NNLL}}$ the NNLL Coulomb potential, the kinetic insertions, and the higher order potentials.

The perturbative relation between m_{pole} and $m_{1\text{S}}$ reads

$$\begin{aligned} m_{1\text{S}} &= m_{\text{pole}} - m_{\text{pole}} [\Delta^{\text{LL}}(h, \nu) + \Delta^{\text{NLL}}(h, \nu) + \Delta_{\text{c}}^{\text{NNLL}}(h, \nu) + \Delta_{\text{m}}^{\text{NNLL}}(h, \nu)] \\ &= m_{\text{pole}} - \frac{2}{9} \alpha_s^2 m_{\text{pole}} + \dots . \end{aligned} \quad (4.17)$$

where $\Delta^{\text{LL}} = -2/9 \alpha_s^2$ is the LL term. $\Delta_{\text{c}}^{\text{NNLL}}$ originates from corrections to the binding energy related to the Coulomb potential at NNLL and $\Delta_{\text{m}}^{\text{NNLL}}$ comes from corrections related to the higher order potentials as well as kinetic insertions. The expressions for Δ^{NLL} , $\Delta_{\text{c}}^{\text{NNLL}}$, and $\Delta_{\text{m}}^{\text{NNLL}}$ can be found in [47] together with the modifications described in [42], which concern changes in $\mathcal{V}_{\text{c}}^{(s)}$

and $\mathcal{V}_k^{(s)}$ due to the sum operators.

We use the implementation of the 1S mass described in [47], where Δ^{LL} , Δ^{NLL} , and Δ_c^{NNLL} are implemented directly in the Coulomb Schrödinger equation, see Equation (3.155). The correction Δ_m^{NNLL} is treated as a perturbation, similar to the higher order potentials as described in Section 3.4.3. The vNRQCD cross section from Equation (3.159) then receives an additional contribution of the form [47]

$$\Delta\sigma_{\text{vNRQCD}} = F(s) \text{Im} \left[\delta G_{1\text{S}}(v_{1\text{S}}, m_{1\text{S}}, \nu, h) \right]$$

$$\delta G_{1\text{S}} = -\frac{\Delta_m^{\text{NNLL}}}{v_{1\text{S}}} \frac{d}{dv_{1\text{S}}} G_{\text{LO}}(v_{1\text{S}}, m_{1\text{S}}, \nu, h), \quad (4.18)$$

where $v_{1\text{S}}$ is the velocity with the 1S mass.

4.4 MSR Mass

While the 1S mass is well-suited for threshold applications and the $\overline{\text{MS}}$ mass works well in the continuum, for the matching a mass scheme is needed, that can be used both at threshold *and* in the continuum.

The MSR mass [89–91] is well-suited for this purpose. It is a low-scale short-distance mass and directly connected to the $\overline{\text{MS}}$ mass. The basic idea is that the renormalon ambiguity in the relation of the pole mass to the $\overline{\text{MS}}$ mass is independent of the mass. Therefore, the scale of the corrections on the right hand side of Equation (4.9) can be changed from \overline{m} to an arbitrary scale R without changing the asymptotic behaviour of the series in the conversion:

$$m_{\text{pole}} = m_{\text{MSRn}}(R) + R \sum_{n=1}^{\infty} a_n(n_l, 0) \left(\frac{\alpha_s^{(n_l)}(R)}{4\pi} \right)^n, \quad (4.19)$$

where $\mu = R$ and m_{MSRn} is the natural MSR mass. The coefficients a_n coming from self-energy diagrams are the same coefficients as in the definition of the $\overline{\text{MS}}$ mass in Equation (4.9). However, they do not include the contributions coming from the heavy quark mass and therefore $n_h = 0$ in Equation (4.19). The heavy quark contributions are integrated out, because the MSR mass is designed for low-scale applications, i.e. for problems that involve only dynamical scales smaller than the heavy quark mass. At these scales, the heavy quark mass is typically integrated out, such that the running of α_s , and the coefficients a_n coming from self-energy contributions, only depend on the number of light flavors n_l .

It is also possible to only change the coupling $\alpha_s^{(n_l+n_h)}$ from the $\overline{\text{MS}}$ mass definition to n_l flavors and leave the contributions from the self-energy unchanged. The resulting MSR mass is called "practical MSR mass" m_{MSRp} and is numerically very similar to the natural MSR mass [89]. It is called practical, because its relation to the $\overline{\text{MS}}$ mass at $R = m_{\text{MSRp}}$ has a particularly simple form: $m_{\text{MSRp}}(m_{\text{MSRp}}) = m_{\overline{\text{MS}}}(m_{\overline{\text{MS}}})$.

The natural MSR mass, however, is conceptually cleaner and we therefore use m_{MSRn} . It depends on the scale R , which can be varied to interpolate between a threshold mass for $R \sim mv$ and a mass very similar to the $\overline{\text{MS}}$ mass for $R \sim m_{\text{MSRn}}$. R can be interpreted as a cutoff on the self-energy contributions that are absorbed into the mass [92]. It only contains the self-energy contributions from scales larger than R . For $R = 0$ it therefore absorbs all of the self-energy and we obtain the pole mass.

Similarly as the $\overline{\text{MS}}$ mass evolves with the UV cut-off μ , the MSR mass can be varied with both

the UV-cutoff μ and the IR-cutoff R . The running of R is called "R evolution" and follows from the R-independence of the pole mass:

$$\begin{aligned}
R \frac{d}{dR} m_{\text{pole}} &= R \frac{d}{dR} m_{\text{MSRn}}(R) + R \frac{d}{dR} \left(R \sum_{n=1}^{\infty} a_n \left(\frac{\alpha_s(R)}{4\pi} \right)^n \right) = 0 \\
R \frac{d}{dR} m_{\text{MSRn}}(R) &= -R \sum_{n=1}^{\infty} a_n \left(\frac{\alpha_s(R)}{4\pi} \right)^n - \sum_{n=1}^{\infty} a_n R \frac{d}{dR} \left(\frac{\alpha_s(R)}{4\pi} \right)^n \\
&= -R \sum_{n=0}^{\infty} \gamma_n^R \left(\frac{\alpha_s(R)}{4\pi} \right)^{n+1}
\end{aligned} \tag{4.20}$$

$$\longrightarrow m_{\text{MSRn}}(R_2) - m_{\text{MSRn}}(R_1) = - \sum_{n=0}^{\infty} \gamma_n^R \int_{R_1}^{R_2} dR \left(\frac{\alpha_s(R)}{4\pi} \right)^{n+1}, \tag{4.21}$$

where γ_i^R can be calculated from the coefficients a_i and the RG-equation of α_s (see Appendix E). At the first two orders we have $\gamma_0^R = a_1$, $\gamma_1^R = a_2 - 2\beta_0 a_1$ and the general formula for γ_i^R at any order i can be found in [89]. Since the coefficients a_i are known up to a_4 , the highest known anomalous dimension is γ_3^R . Equation (4.21) can be solved either numerically or analytically. At leading order, its solution can be computed in terms of incomplete gamma functions and its asymptotic expansion for $\alpha_s \rightarrow 0$ reads [90]

$$m_{\text{MSRn}}(R_2) - m_{\text{MSRn}}(R_1) = \frac{\gamma_0^R R_2}{2\beta_0} \sum_{n=0}^{\infty} \left(\frac{\beta_0 \alpha_s(R_2)}{2\pi} \right) \sum_{k=n+1}^{\infty} \frac{n!}{k!} \log^k \left(\frac{R_2}{R_1} \right). \tag{4.22}$$

Two important observations can be made from Equation (4.21). First, it is a convergent series and therefore the evolution from one scale R_1 to another R_2 is renormalon-free. Second, it sums logarithms of $\log(R_2/R_1)$ to all orders.

Note that $m_{\text{MSRn}}(R_1)$ and $m_{\text{MSRn}}(R_2)$ could also be related directly using the fixed order expansion from Equation (4.19). However, for $R_1 \ll R_2$ logarithms of (R_2/R_1) become large and degrade the perturbative expansion. Using Equation (4.21) then improves the accuracy of the conversion.

Logarithms of infrared scales similar to $\log(R_2/R_1)$ also occur when relating the $\overline{\text{MS}}$ mass to a low-scale short-distance mass. For example, the relation between the 1S mass and the $\overline{\text{MS}}$ mass includes logarithms of the form $\log(\overline{m}/m_{1\text{S}} \alpha_s C_F)$. Using R-evolution, these logarithms can be resummed and the convergence of the MS mass to the 1S improved. For this the $\overline{\text{MS}}$ mass is first related to the MSR mass at the high scale $R_1 \sim \overline{m}$, where no large logarithms occur in the conversion. Then the MSR mass is evolved to the low scale $R_2 \sim mv \sim 20 \text{ GeV}$ with Equation (4.21), resumming large logarithms of R_2/R_1 to all orders in the process. At the low scale, the MSR mass can then be related to the 1S mass. This procedure improves the precision of the conversion between the 1S mass and the $\overline{\text{MS}}$ mass, when compared to the fixed order conversion without resummation of the logarithms. Details on the improvement can be found in [89].

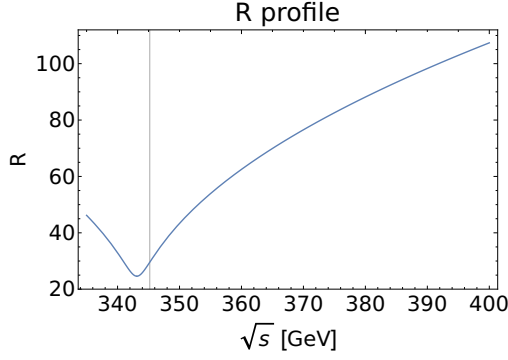


Figure 4.4: Profile for the parameter R used in the cross section in Figure 4.5b.

4.5 QCD Cross Section in the MSR Mass Scheme

At threshold, the QCD cross section does not converge well from order to order, because it is missing higher order threshold contributions. For $\Gamma_t = 0$ the QCD cross section even diverges at threshold at NNLO and N³LO, see Figure 2.2a.

The convergence near threshold can be improved by converting σ_{QCD} to the MSR mass. To avoid power counting breaking effects we have to choose $R \sim mv$ near threshold. We parametrize R in the form

$$\begin{aligned} R &= m_{1S} \nu_* & \text{for} & \quad m_{1S} \nu_* < \bar{m} \\ R &= \bar{m} & \text{for} & \quad m_{1S} \nu_* \geq \bar{m}, \end{aligned} \quad (4.23)$$

where ν_* was defined in Equation (3.172) and the profile of R at threshold and in the intermediate region is shown in Figure 4.4. With this choice for R we effectively interpolate between a low-scale short-distance mass at threshold and a mass nearly identical with the $\overline{\text{MS}}$ mass in the continuum. In Equation (4.23) we use the 1S mass, because in the matching the vNRQCD cross section is also in the 1S scheme. A different value for the mass is also possible, as long as $R \sim mv$ is fulfilled.

Changing to the MSRn scheme and using (4.23), the QCD cross section takes the form shown in Figure 4.5b. Comparing Figure 4.5b with the QCD cross section in the pole mass scheme (Figure 4.5a), one can see that the convergence from order to order near threshold is better for the MSRn mass scheme. In addition, the change from the pole mass to the MSRn mass rearranges the perturbation series such that the cross section becomes less divergent at threshold.

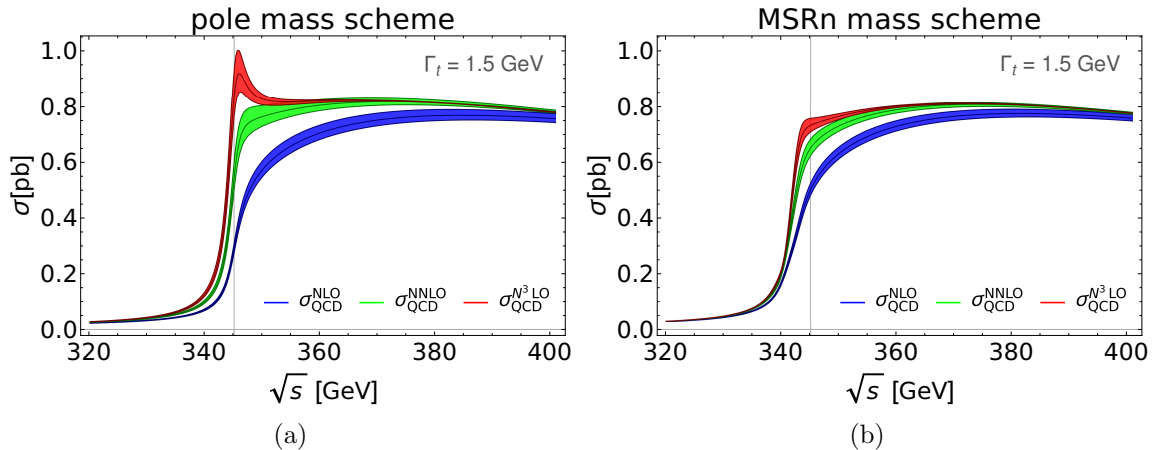


Figure 4.5: QCD cross section near threshold: the cross section in the MSRn mass scheme (b) converges better from order to order than in the pole mass scheme (a).

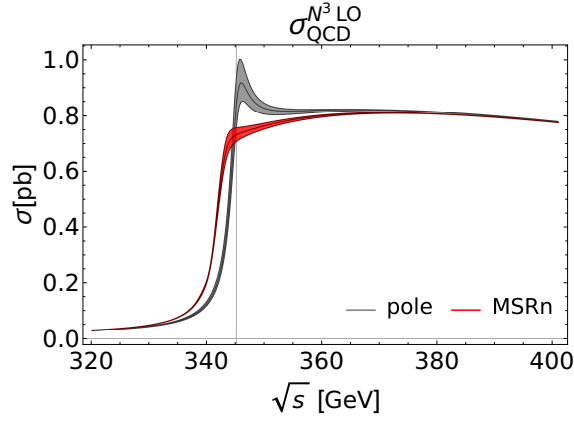


Figure 4.6: QCD cross section at $N^3\text{LO}$ order in the pole mass scheme (gray) and the MSRn mass scheme (red).

Physical observables should of course be independent of the mass scheme. Comparing the cross section in the pole mass and MSRn mass scheme at $N^3\text{LO}$ shows that above 380 GeV they are indeed very similar, see Figure 4.6. Below 360 GeV, however, they diverge, indicating that threshold contributions not included in the QCD cross section become important. From Figure 4.6 we can assume that in the region between 360 GeV and 380 GeV higher order threshold contributions become important and a matched cross section including these contributions is needed.

Chapter 5

Matching Threshold and Continuum Contributions

The vNRQCD cross section is only valid directly at threshold. This was shown explicitly in Section 3.5, where different choices for the Wilson coefficients indicated that shortly after the threshold higher order corrections beyond NNLL seem to become relevant.

On the other hand, the QCD cross section is clearly unusable below about 360 GeV, because the values in different mass schemes start to diverge (see Figure 4.6).

In this chapter the matched cross section for the intermediate region between the threshold and the continuum is constructed. The matching is based on a simple principle (Section 5.1): σ_{QCD} and σ_{vNRQCD} include different powers of α_s and v . In order to include all relevant contributions, we just add them together. Some terms, however, appear in both σ_{QCD} and σ_{vNRQCD} . These double counted terms have to be identified and subtracted (Section 5.2 and 5.3). Lastly, we use a combination of the 1S and the MSR mass scheme to implement a consistent mass scheme in all regions (Section 5.4).

5.1 Matching Formula

In the intermediate region, contributions from both σ_{QCD} and σ_{vNRQCD} are important. The matched cross section σ_{mat} is therefore a combination of σ_{QCD} and σ_{vNRQCD} , minus the double counted terms σ_{exp} , that are contained in both σ_{QCD} and σ_{vNRQCD} . The double counted terms can be determined from expanding σ_{vNRQCD} and σ_{QCD} and therefore we call σ_{exp} the expanded cross section. Since vNRQCD is valid only for $v \ll 1$, we turn the non-relativistic contributions $\sigma_{\text{vNRQCD}} - \sigma_{\text{exp}}$ off in the continuum using a switch-off function f_s :

$$\sigma_{\text{mat}}(\mu_h, \mu_S, \mu_U) = \sigma_{\text{QCD}}(\mu_h) + f_s \left[\sigma_{\text{vNRQCD}}(\mu_h, \mu_S, \mu_U) - \sigma_{\text{exp}}(\mu_h, \mu_S, \mu_U) \right], \quad (5.1)$$

where μ_h , μ_S , and μ_U are the hard, soft, and ultrasoft renormalization scale, respectively. We vary the scales of the QCD, vNRQCD, and expanded cross section simultaneously according to scale choices described in Section 3.5.

The switch-off function f_s is one at threshold and zero in the continuum. The exact form in between, as well as the exact points where it starts to differ from 0 and 1 are to some degree arbitrary and can be used to estimate the theoretical error of the matching. The switch-off function should be continuously differentiable to ensure that there are no unphysical kinks in the cross section. We choose a quadratic switch-off function of the form

$$f_s = \begin{cases} 1 & v_{\text{eff}} < v_1 \\ 1 - \frac{2(v_{\text{eff}} - v_1)^2}{(v_2 - v_1)^2} & v_1 < v_{\text{eff}} < \frac{v_1 + v_2}{2} \\ \frac{2(v_{\text{eff}} - v_2)^2}{(v_2 - v_1)^2} & \frac{v_1 + v_2}{2} < v_{\text{eff}} < v_2 \\ 0 & v_2 < v_{\text{eff}} \end{cases}, \quad (5.2)$$

where v_{eff} is the effective velocity

$$v_{\text{eff}} = \left| \sqrt{\frac{\sqrt{s} - 2m_{1S} + i\Gamma_t}{2m_{1S}}} \right| \quad (5.3)$$

and depends on the 1S mass m_{1S} , because in the matching the vNRQCD cross section is in the 1S mass scheme. The starting and end points of f_s are given by v_1 and v_2 . Exactly at threshold, f_s has to be zero, since the non-relativistic corrections are dominant. Directly over the peak region, however, the relativistic corrections start to get large and we therefore choose the starting point of the switch-off function in a region directly over the peak region. For the end point we choose values around 370 GeV, which corresponds to $v \sim 0.4$, since Figure 4.6 indicates that the non-relativistic corrections are already small in this region. Additionally, the velocity becomes large in this region and the non-relativistic cross section can therefore not be trusted anymore. Thus we choose for v_1 and v_2 the following values

$$0.1 < v_1 < 0.2 \quad \longleftrightarrow \quad 344.5 \text{ GeV} < \sqrt{s_1} < 349.9 \text{ GeV} \quad (5.4)$$

$$0.3 < v_2 < 0.5 \quad \longleftrightarrow \quad 358.5 \text{ GeV} < \sqrt{s_2} < 386.0 \text{ GeV}, \quad (5.5)$$

where $\sqrt{s_1}$ and $\sqrt{s_2}$ are the values of the CM-energy corresponding to v_1 and v_2 according to Equation (5.3). Figure 5.1 shows the values of f_s covered by these conditions.

We perform the matching with the RGI as well as fixed-order cross section. In order to examine the behaviour of the matched cross section from order to order, we consider the following orders:

$$\begin{aligned} \sigma_{\text{mat}}^{\text{LL}} &= \sigma_{\text{QCD}}^{\text{NLO}} + f_s(\sigma_{\text{vNRQCD}}^{\text{LL}} - \sigma_{\text{exp}}^{\text{LL}}) \\ \sigma_{\text{mat}}^{\text{NLL}} &= \sigma_{\text{QCD}}^{\text{NNLO}} + f_s(\sigma_{\text{vNRQCD}}^{\text{NLL}} - \sigma_{\text{exp}}^{\text{NLL}}) \\ \sigma_{\text{mat}}^{\text{NNLL}} &= \sigma_{\text{QCD}}^{\text{N}^3\text{LO}} + f_s(\sigma_{\text{vNRQCD}}^{\text{NNLL}} - \sigma_{\text{exp}}^{\text{NNLL}}), \end{aligned} \quad (5.6)$$

The exact form of the expanded cross section σ_{exp} is specified in Section 5.2 and 5.3. The superscripts LL, NLL, and NNLL indicate the use of the RGI cross section with the resummation of large logarithms of the velocity. For the fixed-order cross section we use the equivalent formulas, only with LL, NLL, NNLL replaced by LO, NLO, NNLO to indicate that the logarithms of v are not resummed.

To complete the matching formula, the double counted contributions σ_{exp} have to be identified, which we will do in the next two sections.

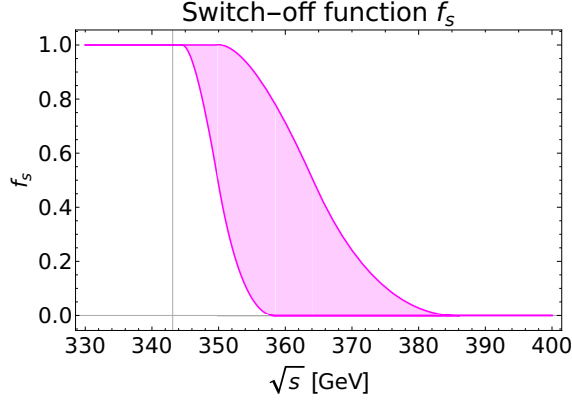


Figure 5.1: Switch-off function f_s : the shaded area shows all values covered by the condition in Equation (5.4). The vertical line denotes the threshold at $2 m_{1S}$.

5.2 Expanded Cross Section at Leading Order

In the intermediate region between $v \sim 0.1$ and $v \sim 0.5$, α_s and v fulfill the relations

$$v < 1, \quad \frac{\alpha_s}{v} < 1, \quad \alpha_s \log v < 1, \quad (5.7)$$

where v is the real velocity $v = \sqrt{\frac{\sqrt{s}-2m+i\varepsilon}{m}}$ without electroweak effects. We will use it to construct the expanded cross section and change $i\varepsilon \rightarrow i\Gamma$ in the end to include leading order electroweak effects at threshold. Note that in the intermediate region the real velocity is numerically very similar to the absolute value of the complex velocity (see Figure 3.15). The leading order vNRQCD cross section can be expanded in α_s/v and $\alpha_s \log v$. Using Equations (3.154), (3.159), and (3.167), it takes the form

$$\begin{aligned} \sigma_{\text{vNRQCD}}^{\text{LL}} = F(s) 6N_c \frac{m^2}{4\pi} \text{Im} \left\{ i v - C_F \alpha_s(\mu_S) \left[\log(-i v) + \log\left(\frac{m}{\mu_S}\right) - \frac{1}{2} + \log 2 \right] \right. \\ \left. + C_F^2 \frac{\alpha_s^2(\mu_S)}{v} \frac{i \pi^2}{12} + \mathcal{O}\left(\frac{\alpha_s^3}{v^2}\right) \right\}. \end{aligned} \quad (5.8)$$

In order to compare this expansion to the relativistic QCD cross section, it has to be expanded in $\alpha_s(\mu_h)$. Using Equation (D.3) to expand $\alpha_s(\mu_S)$, σ_{vNRQCD} takes the form

$$\begin{aligned} \sigma_{\text{vNRQCD}}^{\text{LL}} = F(s) 6N_c \frac{m^2}{4\pi} \\ \times \text{Im} \left\{ i v - C_F \left(\alpha_s(\mu_h) + \alpha_s^2(\mu_h) \frac{\beta_0}{2\pi} \log\left(\frac{\mu_h}{\mu_S}\right) \right) \left[\log(-i v) + \log\left(\frac{m}{\mu_S}\right) - \frac{1}{2} + \log 2 \right] \right. \\ \left. + C_F^2 \frac{\alpha_s^2(\mu_h)}{v} \frac{i \pi^2}{12} + \mathcal{O}\left(\frac{\alpha_s^3}{v^2}\right) \right\}. \end{aligned} \quad (5.9)$$

The QCD cross section $\sigma_{\text{QCD}}^{\text{NLO}}$ can be expanded using the analytic expressions given in Section 2.2. Transforming $\sqrt{s} = m(2 + v^2)$ to the velocity v , we obtain:

$$\sigma_{\text{QCD}}^{\text{NLO}} = F(s) 6N_c \frac{m^2}{4\pi} \text{Im} \left\{ \left[i v - \frac{8v^2}{9\pi} + \mathcal{O}(v^3) \right] - \alpha_s(\mu_h) C_F \left[\left(\log(-i v) + \frac{3}{2} \log 2 - \frac{11}{16} - \frac{3}{2\pi^2} + \frac{21\zeta(3)}{4\pi^2} \right) + \frac{4}{\pi} i v + \mathcal{O}(v^2) \right] \right\} . \quad (5.10)$$

Equations (5.9) and (5.10) both contribute at the orders v and α_s . Their contributions to the cross section are exactly the same and the double counted terms are

$$\sigma_{\text{exp}}^{\text{LL}} = F(s) 6N_c \frac{m^2}{4\pi} \text{Im} \left[i v - \alpha_s(\mu_h) C_F \log(-i v) \right] , \quad (5.11)$$

where all other contributions from Equations (5.9) and (5.10) are real and drop out when taking the imaginary part.

To calculate the fixed-order expanded terms, the soft scale in Equation (5.8) is set to $\mu_S = \mu_h$ and compared to the QCD cross section in Equation (5.10). At leading order, one can see that the higher order logarithms in the RGI vNRQCD cross section do not appear in the QCD cross section and therefore do not contribute to $\sigma_{\text{exp}}^{\text{LL}}$. The fixed-order and RGI expanded cross section are therefore the same at leading order:

$$\sigma_{\text{exp}}^{\text{LO}} = \sigma_{\text{exp}}^{\text{LL}} . \quad (5.12)$$

5.3 Expanded Cross Section at Higher Orders

In the last section we showed that the double counted terms from the QCD and vNRQCD cross section are exactly the same for the leading order matching. This has to be the case, since the effective theory calculation and the expanded full theory terms have to be the same for physical observables.

At higher orders, however, it turns out that some of the double counted terms appearing in both σ_{vNRQCD} and σ_{QCD} are not the same. There are two reasons for this. First, at order $\mathcal{O}(\alpha_s^2)$ and $\mathcal{O}(\alpha_s^3)$ we are using Padé approximations for the QCD cross section, because the analytic expressions are currently unknown. Secondly, the vNRQCD cross section misses some contributions induced by the finite width. The effective field theory approach only includes QCD modes (i.e. the velocity v is real) and the width is included only after the EFT calculation is completed.

To examine the higher order contributions, we define

$$\sigma = \frac{4m^2}{s} \text{Im}[\varrho] . \quad (5.13)$$

The expanded cross section for the fixed-order cross section then has the general form

$$\varrho_{\text{exp}}^{\text{FO}} = \sum_{i=1}^{n_{\text{max}}} \sum_{j=0}^{n_{\text{max}}} v^i \left(\frac{\alpha_h}{v} \right)^j b_{ij}(m, \mu_h, v) , \quad (5.14)$$

where $n_{\text{max}} = (1, 2, 3)$ for the (LO, NLO, NNLO) cross section, respectively. The coefficients $b_{ij} = b_{ij}^{\text{pole}}$ include logarithms of v , m , and μ_h and are specified in Appendix G. Note that up to now, we have been in the pole mass scheme and therefore $m = m_{\text{pole}}$. A different mass scheme is discussed in Section 5.4.

For the RGI matching, the resummed logarithms in the vNRQCD cross section lead to additional double counted terms:

$$\begin{aligned}
\varrho_{\text{exp}}^{\text{LL}} &= \varrho_{\text{exp}}^{\text{LO}} \\
\varrho_{\text{exp}}^{\text{NLL}} &= \varrho_{\text{exp}}^{\text{NLO}} + v^2 \left(\frac{\alpha_h}{v} \right) c_{211}(L) \alpha_h \\
\varrho_{\text{exp}}^{\text{NNLL}} &= \varrho_{\text{exp}}^{\text{NNLO}} + v^2 \left(\frac{\alpha_h}{v} \right) c_{212}(L) \alpha_h^2 + v^3 \sum_{j=0}^2 \sum_{k=1}^{3-j} \left(\frac{\alpha_h}{v} \right)^j c_{3jk}(L) \alpha_h^k, \quad (5.15)
\end{aligned}$$

where the functions $c_{ijk}(L)$ include logarithms of power L^k and $L = (\log v, \log \nu)$ can be a logarithm of either v or ν . We will now calculate the expansions of the vNRQCD and QCD cross section for both the fixed-order and RGI matching, and discuss which of their terms to include in the expanded cross section σ_{exp} .

Fixed-Order Matching

For the QCD cross section the extraction of the expanded terms is simple, because the analytic expressions are known. However, the analytic expressions are only exact at order $\mathcal{O}(\alpha_s^0)$ and $\mathcal{O}(\alpha_s^1)$. At order $\mathcal{O}(\alpha_s^2)$ and $\mathcal{O}(\alpha_s^3)$ Padé approximations are used and only the lowest order terms $\mathcal{O}(\alpha_s^2/v, \alpha_s^2, v\alpha_s^2)$ and $\mathcal{O}(\alpha_s^3/v^2, \alpha_s^3/v, \alpha_s^3)$, which are used together with expansions in the low energy and high energy limit to construct the Padé approximation, are exact. They are taken from vNRQCD calculations and therefore are the same in the QCD and vNRQCD cross section. The QCD cross section σ_{QCD} expanded in v is listed in Table F.1 and Table F.2.

The vNRQCD cross section from Equation (3.159) has contributions coming from the effective Coulomb potential on the one hand and the higher order potentials as well as kinetic insertions on the other hand. The contributions coming from the higher order potentials and kinetic insertions are known analytically, cf. Section 3.4.3). The Coulombic part of the cross section coming from G_c^{NNLL} , on the other hand, is determined by solving the Schrödinger equation numerically. To find the lowest order terms generated by G_c^{NNLL} , we calculate the lowest order loop diagrams with the effective Coulomb potential from Equation (3.139). For the expanded cross section we need the terms up to α_s^3 , since the QCD amplitude also includes powers in α_s up to this order. The relevant diagrams are

$$G_c^{\text{NNLL}} = G_c^{\text{LL}} + (-i) \text{ (diagram with two loops and } V_{c,\text{eff}}^{\text{NLO}} \text{)} + 2(-i) \text{ (diagram with three loops and } V_{c,\text{eff}}^{\text{NLO}}, V_{c,\text{eff}}^{\text{LO}} \text{)} + (-i) \text{ (diagram with two loops and } V_{c,\text{eff}}^{\text{NNLO}} \text{)} + \dots \quad (5.16)$$

These diagrams were calculated in Section 3.1.1 with the leading order Coulomb potential $V_{c,\text{eff}}^{\text{LO}} \propto \frac{1}{\mathbf{k}^2}$ using the method of regions. At higher orders the effective Coulomb potential has terms of the form $V_{c,\text{eff}}^{\text{NNLO}} \propto \left(\frac{1}{\mathbf{k}^2}, \frac{\log \mathbf{k}^2}{\mathbf{k}^2}, \frac{\log^2 \mathbf{k}^2}{\mathbf{k}^2} \right)$, which can be rewritten with the trick

$$\frac{\log^n(\mathbf{k}^2)}{\mathbf{k}^2} = (-1)^n \frac{d^n}{dx^n} \frac{1}{(\mathbf{k}^2)^x} \Big|_{x=1}. \quad (5.17)$$

The integrals from Equation (5.18) can then be reduced to the same form as the integrals from Section 3.1.1 and take the form

$$\begin{aligned}
(-i) \text{ (diagram)} &= (6N_c) (\alpha_S^2 C_F) m^2 \left[a_1 I^{(2)}(1) + \beta_0 \left(\log(\mu_S^2) I^{(2)}(1) + \frac{d}{dx} I^{(2)}(x) \right) \right] \Big|_{x=1} \\
&\quad V_{c,\text{eff}}^{\text{NLO}} \\
(-i) \text{ (diagram)} &= (4\pi) (6N_c) (\alpha_S^3 C_F^2) m^2 \\
&\quad V_{c,\text{eff}}^{\text{NLO}} \quad V_{c,\text{eff}}^{\text{LO}} \\
&\quad \times \left[a_1 I^{(3)}(1) + \beta_0 \left(\log(\mu_S^2) I^{(3)}(1) + \frac{d}{dx} I^{(3)}(x) \right) \right] \Big|_{x=1} \\
(-i) \text{ (diagram)} &= (6N_c) \left(\frac{\alpha_S^3 C_F}{4\pi} \right) m^2 \\
&\quad V_{c,\text{eff}}^{\text{NNLO}} \\
&\quad \times \left[a_2 I^{(3)}(1) + (2\beta_0 a_1 + \beta_1) \left(\log(\mu_S^2) I^{(3)}(1) + \frac{d}{dx} I^{(3)}(x) \right) \right. \\
&\quad \left. + \beta_0^2 \left(\log^2(\mu_S^2) I^{(2)}(1) + \log(\mu_S^2) \frac{d}{dx} I^{(3)}(x) + \frac{d^2}{dx^2} I^{(3)}(x) \right) \right] \Big|_{x=1} \\
&\quad (5.18)
\end{aligned}$$

where $m = m_{\text{pole}}$ and $\alpha_S = \alpha_s(\mu_S)$. $I^{(2)}(x) = I^{(2)}(1, x, 1; mE)$ and $I^{(3)}(x) = I^{(3)}(1, x, 1, 1, 1; mE)$ are calculated in Appendix D. Using the results given in Equations (D.8) and (D.19) for $I^{(2)}$ and $I^{(3)}$, respectively, the imaginary part of G_c^{NNLL} evaluates to

$$\begin{aligned}
\text{Im}[G_c^{\text{NNLL}}] &= \text{Im} \left\{ G_c^{\text{LL}} + \alpha_S^2 \frac{2}{9\pi} \left[\log(-iv) \left(-23 \log\left(\frac{\mu_S^2}{m^2}\right) - \frac{43}{3} + 46 \log(2) \right) + 23 \log^2(-iv) \right] \right. \\
&\quad + \frac{\alpha_S^3}{v} \frac{4\pi}{27} \left[+ \frac{23i}{3} \log\left(\frac{\mu_S^2}{m^2}\right) + \frac{43i}{9} - \frac{92i \zeta(3)}{\pi^2} - \frac{46i}{3} \log(2) - \frac{46i}{3} \log(-iv) \right] \\
&\quad + \alpha_S^3 \frac{1}{81\pi^2} \left[\log(-iv) \left(-\frac{1587}{2} \log^2\left(\frac{\mu_S^2}{m^2}\right) - 1511 \log\left(\frac{\mu_S^2}{m^2}\right) + 3174 \log\left(\frac{\mu_S^2}{m^2}\right) \log(2) \right. \right. \\
&\quad \left. \left. + 279 \zeta(3) + \frac{243\pi^4}{8} - \frac{2559\pi^2}{2} - \frac{7217}{12} - 3174 \log^2(2) + 3022 \log(2) \right) \right. \\
&\quad \left. \left. + \log^2(-iv) \left(1587 \log\left(\frac{\mu_S^2}{m^2}\right) + 1511 - 3174 \log(2) \right) - 1058 \log^3(-iv) \right] + \mathcal{O}(\alpha_s^4) \right\}. \\
&\quad (5.19)
\end{aligned}$$

Note that $I^{(2)}$ produces a real divergence, which drops out when taking the imaginary part. The logarithms of μ_S are generated only by the running of α_s and Equation (5.19) at the hard scale μ_h therefore has the same form, only with μ_S replaced by μ_h , and α_S replaced by α_h .

Multiplying Equation (5.19) with the Wilson coefficient $c_1(h, \nu)$ and adding the expansions in v of the contributions generated by the higher order potentials and kinetic insertions, we obtain the expansions given in the Tables F.3 and F.4. Note that in the Tables F.3 and F.4 ν is set to one for the fixed-order contributions.

Comparing the expansions of the QCD and vNRQCD cross section in Appendix F up to order $v^3 \left(\frac{\alpha_s}{v}\right)^i$ for $i = 0, 1, 2, 3$, one finds that two terms are different: the contributions of order v^2 and

$\alpha_s v^2$. The difference occurs, because in our use of vNRQCD the top quark is treated as a stable particle in all calculation, and the top width is only introduced at the end with the prescription $E \rightarrow E + i\Gamma_t$. Contributions of the form $(b v^2)$ with $(b \in \mathbb{R})$ are real for stable quarks and therefore do not contribute to the stable cross section. This explains why all terms with a non-zero imaginary part for $\Gamma_t = 0$ are the same and only the terms with a real coefficient are different between the QCD and vNRQCD cross section.

These terms are, however, suppressed by Γ_t/m and their difference is very small. We choose the expanded terms of the vNRQCD cross section for σ_{exp} . The coefficients b_{ij} from Equation (5.14) can then be read off from the tables in Appendix F and are listed in Appendix G.

RGI Matching

For the RGI matching the QCD amplitude stays the same, but the vNRQCD cross section includes the resummed logarithms of v . Some of the higher order logarithms appear in both σ_{vNRQCD} and σ_{QCD} and therefore have to be included in σ_{exp} .

To find the extra logarithms in σ_{vNRQCD} , we expand the vNRQCD cross section in α_h . The logarithms are resummed into the Wilson coefficients, which in turn depend on α_h , α_s , and α_{US} . sing the RG running of α_s , the Wilson coefficients can be expanded in α_h .

As an example, consider the following vNRQCD contribution to the cross section from Section 3.5:

$$\Delta\sigma = \left(\sigma_{\text{pt}} (6 N_c) F(s) \right) 2 c_1^{\text{LL}} c_2^{\text{LL}} \text{Im}[v^2 G_c^{\text{LL}}] \quad (5.20)$$

Expanding the Wilson coefficients in α_h with Equation (3.126) and Equation (D.3), we obtain:

$$c_1^{\text{LL}} = 1 \quad (5.21)$$

$$c_2^{\text{LL}} = -\frac{1}{6} + \frac{16}{9\pi} \alpha_h \log(\nu^2) + \dots \quad (5.22)$$

$$v^2 G_c^{\text{LL}} = \frac{m^2}{4\pi} (i v^3 + \dots) . \quad (5.23)$$

Together, they evaluate to

$$\begin{aligned} \Delta\sigma &= \text{Im} \left[-\frac{2}{3} i v^3 + \frac{128}{9\pi} i v^3 \alpha_s \log \nu \right] \left(\sigma_{\text{pt}} \frac{4m^2}{s} \right) \\ &= \text{Im} [-0.67 i v^3 + 4.53 i v^3 \alpha_s \log \nu] \left(\sigma_{\text{pt}} \frac{4m^2}{s} \right) \end{aligned} \quad (5.24)$$

At the order $v^3 \alpha_h \log \nu$ this already gives the full contribution, cf. Table F.3. Expanding all other Wilson coefficients and couplings in the same way, we obtain the higher order logarithms listed in the Tables F.3 and F.4.

Contributions including logarithms of the form $i \log(v)^i v^j \alpha_s^k$ with $k = 1, 2, 3$ appear in both the vNRQCD and QCD cross section. For $k+j \leq 3$ they are exactly the same, since the fixed-order NNLO vNRQCD cross section was used as input for the construction of the Padé approximations [19]. For $k+j > 3$, however, the expansions are *not* the same. Although the Padé approximations do not incorporate these terms explicitly, some information of them is still included through the low-energy and high-energy expansions that are used to construct the Padé approximation. This becomes apparent when comparing the QCD terms of order $v^3 \alpha_s \log v$ and $v^3 \alpha_s^2 \log^2 v$ in Tables F.1 with the vNRQCD terms in F.3: they are strikingly similar to each other.

Figure 5.2 and 5.3 compare the expanded cross section to the QCD and vNRQCD cross section. For the RGI setting, Figure 5.2 compares additionally the expanded cross section with the RGI logarithms taken from the vNRQCD cross section to the expanded terms that are obtained from the QCD cross section. The QCD expansions approximate the QCD cross section very well below ~ 344 GeV, indicating that corrections beyond NNLL are very small at threshold. The NRQCD expansions on the other hand are practically identical with σ_{vNRQCD} above 360 GeV. This already suggests, that below 344 GeV the vNRQCD cross section can be used instead of the matched cross section, since σ_{QCD} and σ_{exp} cancel in Equation (5.1). Above 360 GeV on the other hand σ_{vNRQCD} and σ_{exp} cancel and therefore the QCD cross section can be used in this region instead of the matched cross section.

Comparing the expansions $\sigma_{\text{exp}}^{\text{vNRQCD}}$ and $\sigma_{\text{exp}}^{\text{QCD}}$, one can see that in the intermediate region their central value is approximately the same, but the error on the vNRQCD expansions is much larger than the one from the QCD expansions. At threshold, on the other hand, their deviation is only small. In order to avoid an artificially large error in the matched cross section coming from the difference of the QCD expansions to the vNRQCD cross section, we choose the vNRQCD expansions for the matching. The explicit expressions of the resulting coefficients c_{ijk} are given in Appendix G.

5.4 Mass Scheme

The mass scheme for the matching has to be chosen carefully, since the pole mass leads to a bad convergence of the perturbative series, the $\overline{\text{MS}}$ mass breaks the power-counting at threshold, and the 1S mass is designed only specifically for applications at threshold (see Chapter 4). The MSR mass, on the other hand, can be used both at threshold and in the continuum, if the free scale R is chosen appropriately.

We use a mixed 1S-MSR mass scheme for the matching. The vNRQCD cross section only contributes at threshold and in the intermediate region. It is not used in the continuum and therefore we take the 1S mass scheme for σ_{vNRQCD} . The QCD cross section, on the other hand, is used in all regions and therefore needs the MSR scheme with $R \sim mv$ (cf. Section 4.5). Accordingly, we also choose the MSR scheme for the double counted terms σ_{exp} . By setting $R = m_{1\text{S}}\nu_*$ with ν_* from Equation (3.172), we ensure that R is at all times of order mv .

The QCD cross section can be easily converted to the MSR mass scheme using Equation (4.19). Plugging the pole mass expressed in the MSRn mass scheme into σ_{QCD} and expanding in α_s , one obtains the QCD cross section in the MSRn mass scheme.

The conversion of the expanded cross section is similar, but the expansion has to be done in α_s , v , and in R , since R is of order mv . For example, v_{pole}^3 generates the terms

$$v_{\text{pole}}^3 = v_{\text{MSRn}}^3 - 3 a_1 \frac{R}{m_{\text{MSRn}}} (\alpha_s v_{\text{MSRn}}) + \frac{3 a_1}{2} \frac{R^2}{m_{\text{MSRn}}^2} \frac{\alpha_s^2}{v_{\text{MSRn}}} + \frac{a_1}{2} \frac{R^3}{m_{\text{MSRn}}^3} \frac{\alpha_s^3}{v_{\text{MSRn}}^3} + \mathcal{O}(\alpha_s^4), \quad (5.25)$$

where a_1 is the coefficient in the conversion formula between the pole and MSRn mass (see Equation (4.19)). Counting only α_s and v , the terms above would be NNLO, NLO, LO, and even beyond LO. However, when counting also R as mv , one can see that all terms actually belong to NNLO. The coefficient b_{ij} and c_{ijk} from Equation (5.14) and Equation (5.15) in the MSRn scheme then take the form given in Appendix G.

We choose as input for the matching the $\overline{\text{MS}}$ mass

$$\overline{m} = m_{\overline{\text{MS}}}(m_{\overline{\text{MS}}}) = 163 \text{ GeV} \quad (5.26)$$

and calculate all other masses from \overline{m} :

$$\begin{aligned}
m_{\text{MSRn}}(\overline{m}) &= 163.032 \text{ GeV} \\
m_{1\text{S}} &= 171.557 \text{ GeV} \\
m_{\text{pole}} &= 172.6 \text{ GeV} .
\end{aligned} \tag{5.27}$$

In order to have a good convergence between \overline{m} and m_{MSRn} , the MSR mass is first calculated at $R = \overline{m}$ from the $\overline{\text{MS}}$ mass and subsequently run down from \overline{m} to $R \sim mv$ with Equation (4.21), which resums logarithms of \overline{m}/R to all orders in α_s . To calculate $m_{\text{MSRn}}(R = \overline{m})$ from \overline{m} , we subtract Equation (4.19) from Equation (4.9) and use the three loop conversion (a_i , $i = 0, 1, 2$), since the highest power of α_s in the QCD cross section is α_s^3 .

For the 1S mass, we first calculate $m_{\text{MSRn}}(R)$ at $R = \overline{m}$ and use the R evolution equation to run it down to $R = 35 \text{ GeV}$. Then we can obtain $m_{1\text{S}}$ from $m_{\text{MSRn}}(R = 35 \text{ GeV})$ by subtracting Equation (4.17) from Equation (4.19). Since $R \sim mv$ for $R = 35 \text{ GeV}$, R has to be counted as an $m\alpha_s$ term in the conversion.

Note that instead of converting from $\overline{\text{MS}}$ to $m_{\text{MSRn}}(\overline{m})$, running down to $m_{\text{MSRn}}(35 \text{ GeV})$, and then converting to the 1S mass, one could also calculate the 1S mass directly from the $\overline{\text{MS}}$ mass using Equation (4.9) and Equation (4.17). However, this method is inferior in terms of accuracy, because the MSR mass with R evolution resums logarithms of $R/\overline{m} = 35 \text{ GeV}/\overline{m}$ to all orders in α_s , which is not possible in the direct conversion. The resummation improves the theoretical error from scale variation by about a factor 2 as compared to the direct conversion [89].

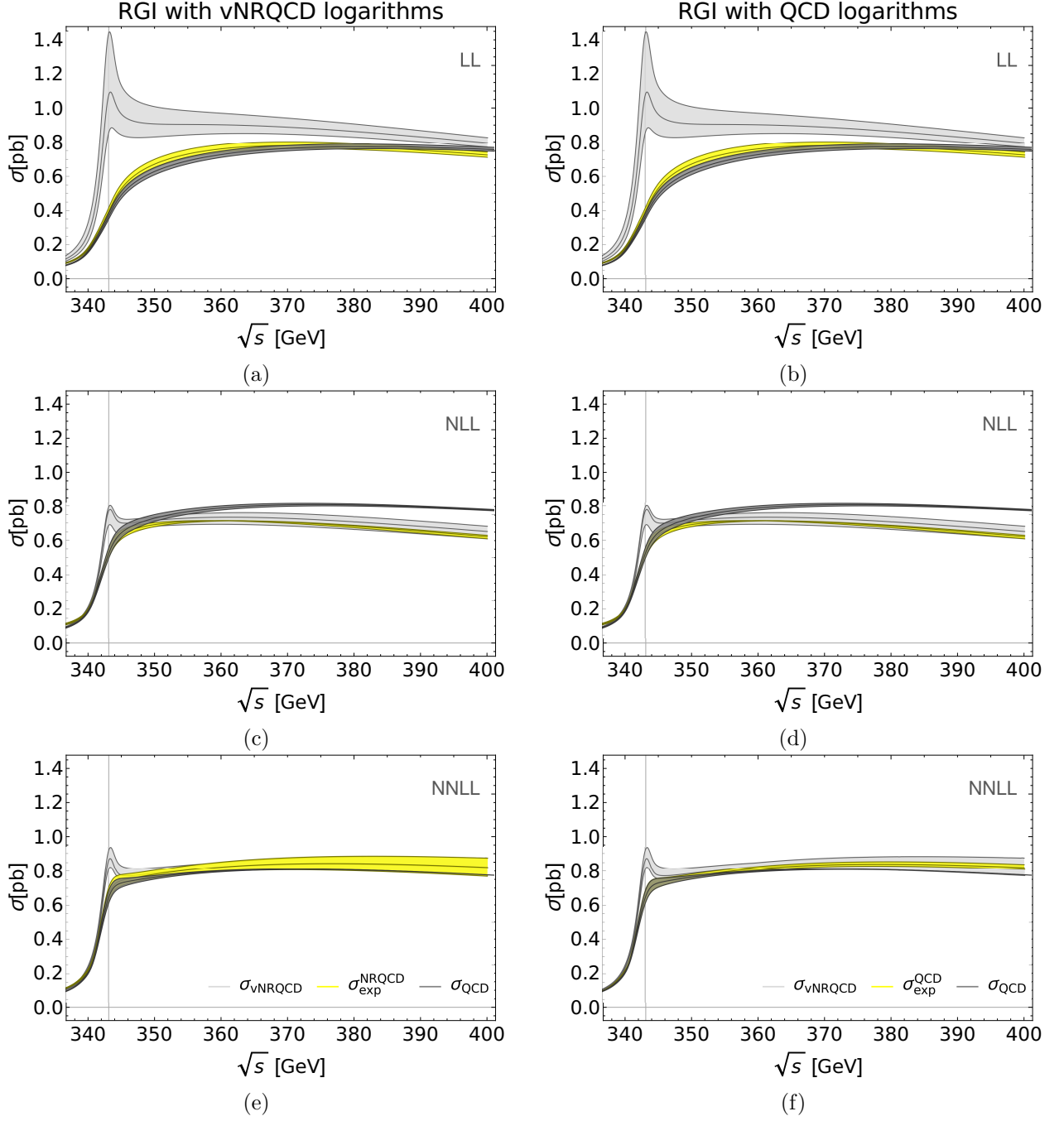


Figure 5.2: Comparison of the expanded cross section (yellow) to the QCD cross section (dark gray) and the vNRQCD cross section (light gray) at LL, NLL, and NNLL for the RGI setting. The expanded cross section can be constructed with higher order logarithms from either the vNRQCD cross section (left) or the QCD cross section (right). The QCD and expanded cross section are in the natural MSR mass scheme, and the vNRQCD cross section in the 1S mass scheme.

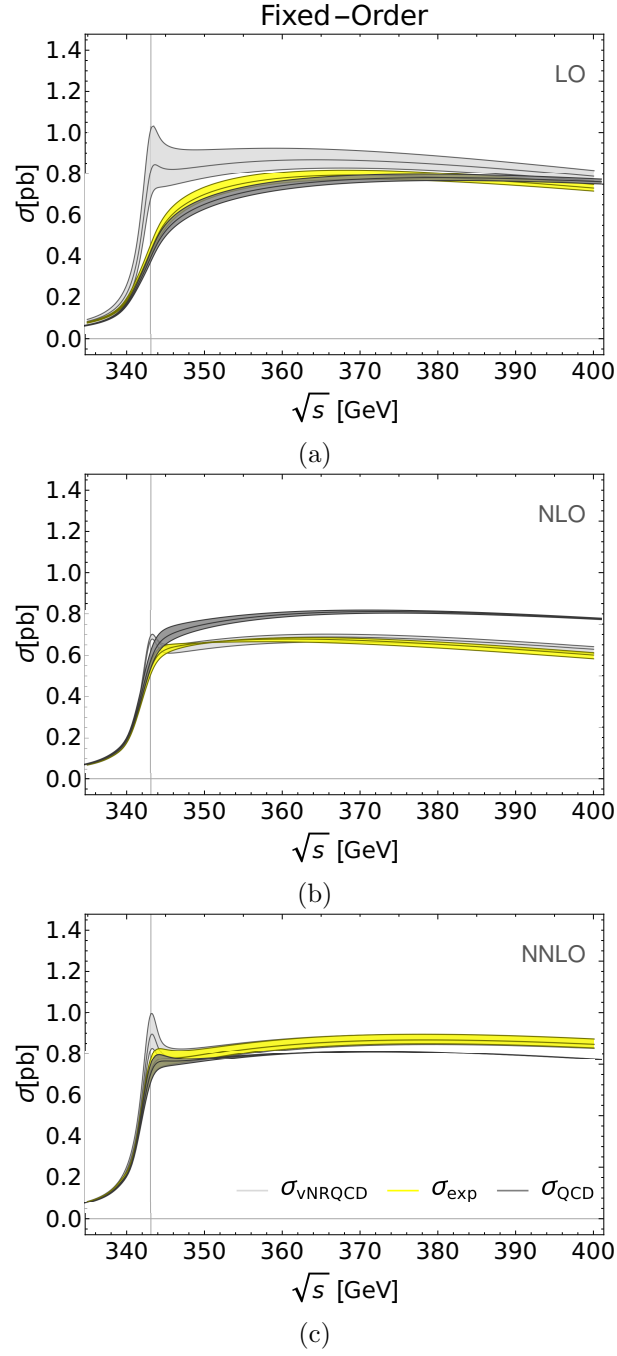


Figure 5.3: Comparison of the expanded cross section (yellow) to the QCD cross section (dark gray) and the vNRQCD cross section (light gray) at LO, NLO, and NNLO for the fixed-order setting. The QCD and expanded cross section are in the natural MSR mass scheme, and the vNRQCD cross section in the 1S mass scheme.

Chapter 6

Results and Discussion

Figures 6.1-6.3 show the results for the matched cross section in the fixed-order and the RGI setting. Figure 6.1 compares the matched cross section at different orders. It includes both the error coming from the switch-off function and the error from the renormalization scales and shows that the error decreases when going to higher orders in the matching. It can also be seen that the cross section has two increases in error. The first increase is directly at threshold and comes from the variation of the renormalization scales. The second increase above threshold is caused by the switch-off function.

The sources of the theoretical error can be seen in Figure 6.2 and Figure 6.3, where the dark colored area corresponds to the variation of the switch-off function with the renormalization scales fixed to the default values $f = 1$ and $h = 1$. The light colored area is obtained by including additionally the variation of the renormalization scales. The dark colored line is our default curve, which is the mean of the maximum and minimum values of the dark colored area.

The curves in Figure 6.2 and 6.3 show that at leading order the error coming from the switch-off function is large, but at next-to-leading order it is already much smaller. At the highest order, the dependence on the switch-off function is barely visible and much smaller than the error coming from the renormalization scales. The small error can be traced back to the expanded cross section shown in Figure 5.2 and 5.3: In the intermediate region, the vNRQCD cross section at NNLO and NNLL is very well approximated by the expanded cross section. Therefore, their contributions cancel in the matching formula (5.1) and the dependence on the switch-off function becomes small.

Comparing the matched cross section to the QCD and the vNRQCD cross section, respectively, (see Figure 6.2) the region where the matched cross section differs from both the QCD and the vNRQCD can be identified. In the intermediate region from $v = 0.1$ to $v = 0.5$, the leading order cross section has a strong dependence on the switch-off function and therefore differs in the whole region from the QCD and the vNRQCD cross section. At NLO and NLL, the expanded cross section converges more quickly to the QCD cross section and therefore the matched and the QCD cross section overlap already at 360 GeV, far below the end of the switch-off. At the highest order, they are nearly identical already at 355 GeV.

At threshold, the vNRQCD and the matched cross section overlap, but they have a small vertical offset. For the fixed-order matching at LO, NLO, and NNLO, and for the RGI matching at LL and NLL, the offset arises, because the expansions do not approximate the QCD cross section at threshold exactly. They have a small offset (see Figures 5.2 and 5.3) which is passed on to the matched cross section. Also the NNLL RGI matched cross section has a small offset to the vNRQCD cross section, but it originates from using the vNRQCD expansions instead of the QCD expansions in the expanded cross section: The QCD expansions in Figure 5.2f show that the matched cross section and the QCD expanded cross section overlap exactly at threshold, while the vNRQCD expanded cross section in Figure 5.2e has a small vertical offset to the QCD cross section.

The matched cross section starts to differ significantly from the vNRQCD cross section already directly after the peak region. At lowest order, the starting point of the deviation depends strongly on the starting point of the switch-off function, since the expanded cross section does not approximate

the vNRQCD in the intermediate region well. This also causes an increase of the theoretical error. At the highest order, however, the deviation of the matched cross section from the vNRQCD cross section is almost independent of the exact starting point of the switch-off function. In addition, the theoretical error decreases in the intermediate region. In particular it is much smaller than the error of the vNRQCD cross section already directly after the peak region. From the points, where the matched cross section starts to deviate from the QCD and the vNRQCD cross section, respectively, we can conclude that at NLO, NNLO, and NLL, NNLL, the matched cross section should be used in a region starting from directly after the peak region to about 360 GeV. Below and above this region the vNRQCD and the QCD cross section, respectively, can be used instead of the matched cross section.

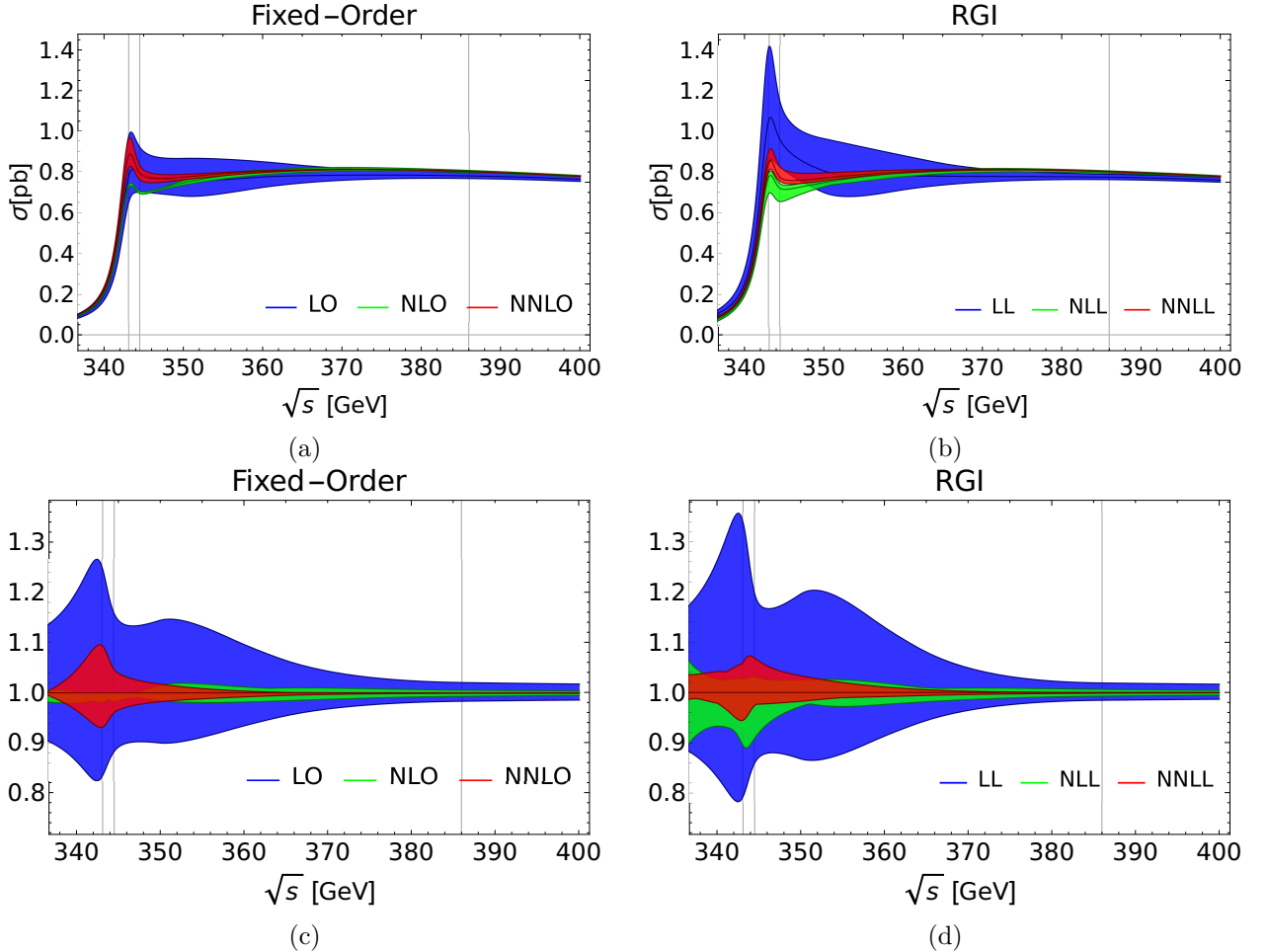


Figure 6.1: Matched cross section at different orders including errors from the variation of both the switch-off function and the renormalization scales. The top row shows the absolute theoretical error of the matched cross section for (a) the fixed-order and (b) the RGI setting. In the bottom row the relative errors for the fixed-order (c) and the RGI (d) setting are shown. The dark lines correspond to the default curves and the vertical lines denote the threshold at $\sqrt{s} = 2m_{1s}$, the lowest starting point of the switch-off function at $v = 0.1$, and its highest end point at $v = 0.5$.

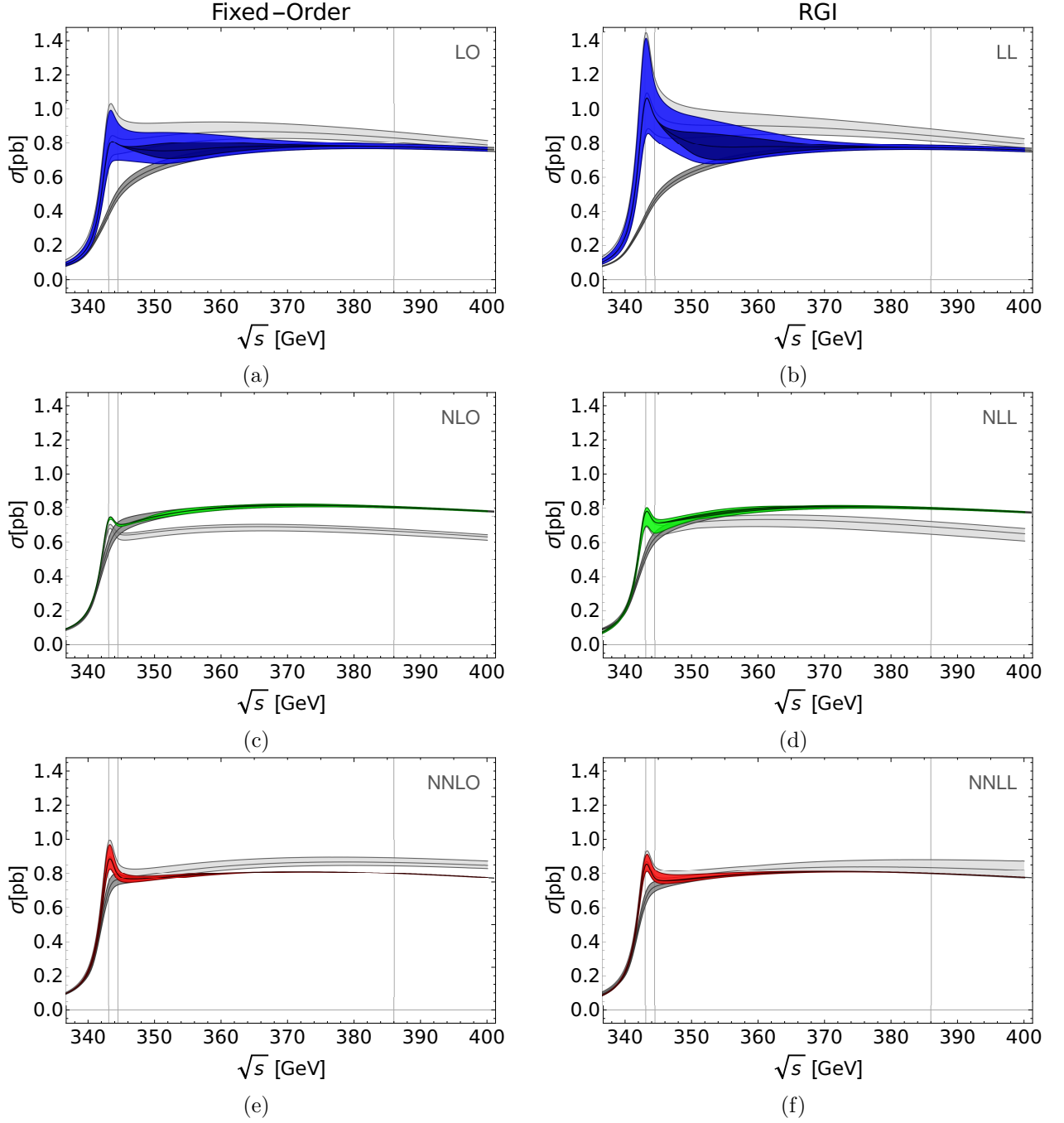


Figure 6.2: Comparison of the matched cross section (colored) to the vNRQCD cross section (light gray) and the QCD cross section (dark gray) for the fixed-order setting (left column) and the RGI setting (right column). For the matched cross section the error caused by the switch-off function from variations around default curve ($f = 1, h = 1$) is shown as the dark colored area.

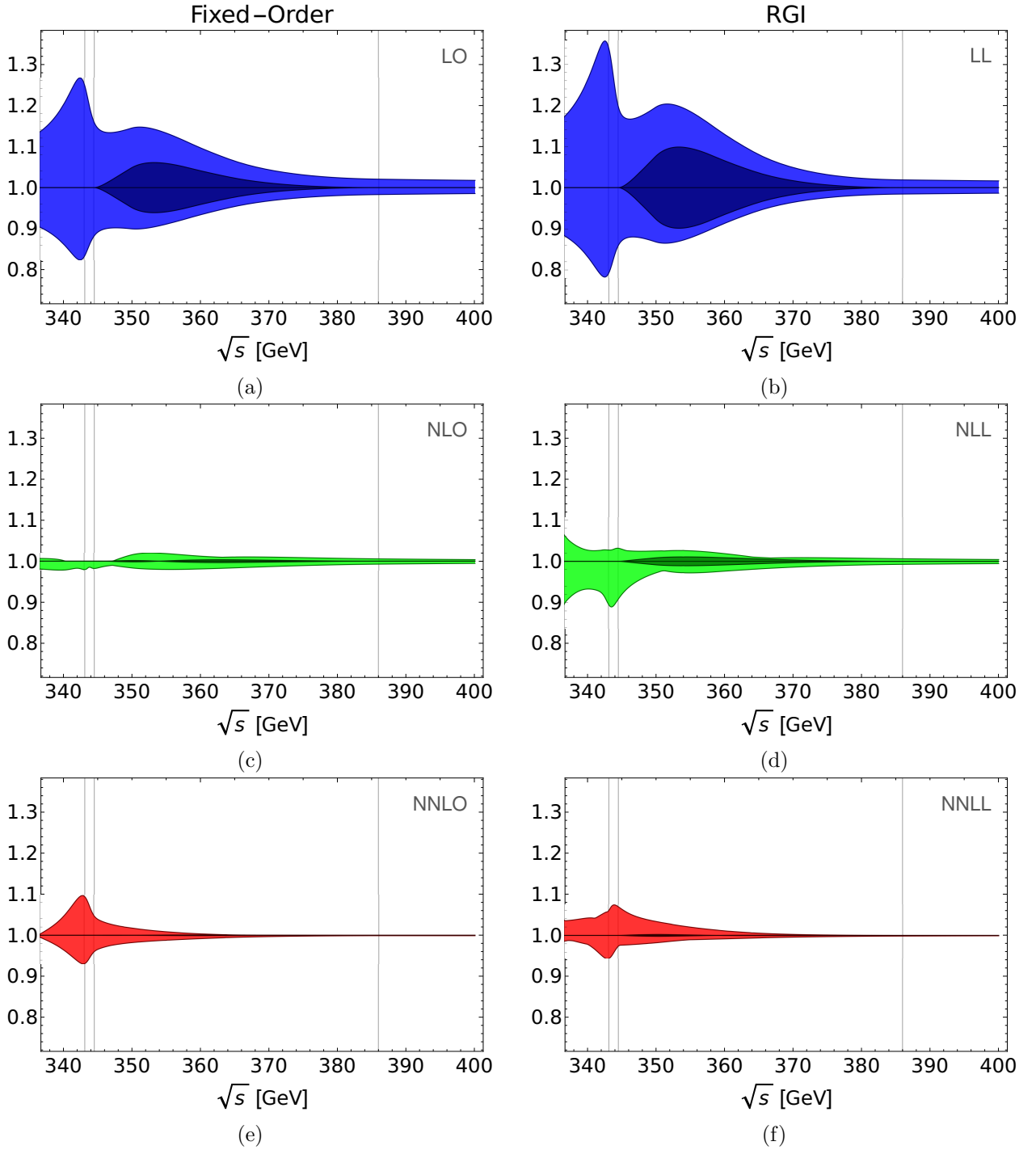


Figure 6.3: Comparison of the relative errors coming from the switch-off function (dark colored area) to the errors from the combined variations of the switch-off function and the renormalization scales (light colored area). The curves are shown for the fixed-order setting (left column) as well as the RGI setting (right column).

Chapter 7

Conclusions

In this thesis we performed a study on the matching of the inclusive, photon induced top quark pair production cross section $\sigma(e^+e^- \rightarrow \gamma^* \rightarrow t\bar{t})$ between threshold and continuum. $t\bar{t}$ production at and near threshold is one of the main goals of a future linear collider and will provide high precision measurements of the top quark mass and width.

The main contributions at and near threshold come from QCD, together with leading order top decay. Therefore we included QCD effects up to N³LO for the QCD cross section, and effects up to NNLL in the RGI setting and NNLO in the fixed order setting for the vNRQCD cross section. Additionally, we shifted the center-of-mass energy \sqrt{s} into the complex plane by an amount of the top decay width Γ_t to include leading order electroweak effects at threshold. We leave higher order electroweak effects and non-resonant contributions for further studies.

For the matching we used a mixed 1S-MSR mass scheme to have a consistent mass scheme in the matching without the renormalon ambiguity from the pole mass and the power counting breaking effects from the $\overline{\text{MS}}$ mass. We studied the matching for both the fixed-order and the renormalization group improved threshold cross section. For both cases we found good convergence of the matched cross section from order to order. In particular, the dependence on the switch-off function, which quantifies the theoretical error in our matching, nearly vanishes at the highest order, showing the consistency of our matching procedure.

At threshold, we used a computation of the cross section with the effective field theory vNRQCD, which resums logarithms of the velocity to all orders. We gave an overview of vNRQCD and the calculation of the threshold cross section in Chapter 3 and showed how the logarithms and the Coulomb singularity contributions are resummed to all orders.

Using the matched cross section, we determined in which region the threshold and continuum cross section are valid. We found that the matched cross section starts to differ from the threshold cross section already directly after the peak region, indicating that higher order relativistic corrections become important. On the other hand, the continuum cross section differs from the matched cross section below ~ 360 GeV, indicating that higher order corrections from the Coulomb singularity and the threshold logarithms become large. Thus we conclude that the matched cross section is needed to interpolate between the vNRQCD and QCD cross section in a region starting from directly above the threshold peak up to about 360 GeV .

Appendix A

Optical Theorem

The optical theorem is based on the principle of probability conservation. Suppose we have a state $|i\rangle$, whose time evolution into the state $|b\rangle$ is described by the S matrix, such that $\langle b| = S \langle i|$. If the probability for the initial state state was $\langle i|i\rangle^2 = p$, then the probability after time evolution should remain the same $\langle b|b\rangle^2 = \langle i|S^\dagger S|i\rangle^2 = p$. This is only possible, if S is unitary:

$$S^\dagger S = \mathbb{1} . \quad (\text{A.1})$$

The S matrix can be divided into two parts:

$$S = \mathbb{1} + iT . \quad (\text{A.2})$$

$\mathbb{1}$ means there is no change in the state over time, only T contains the changes of state. T includes an overall δ -function, which is pulled out when relating T to the transition amplitude \mathcal{M} :

$$\langle i|T|b\rangle = (2\pi)^4 \delta^{(4)}(p_i - p_b) \mathcal{M}(i \rightarrow b) . \quad (\text{A.3})$$

Note that we pulled out also an overall factor of i . This corresponds to the usual convention, where the quantity calculated with Feynman rules is $i\mathcal{M}$. Using the unitarity of the S matrix, we can derive a relation for T :

$$\begin{aligned} S^\dagger S &= \mathbb{1} \\ i(T^\dagger - T) &= T^\dagger T \\ \langle b|T^\dagger - T|i\rangle &= \langle b|T^\dagger T|i\rangle . \end{aligned} \quad (\text{A.4})$$

Inserting a complete set of intermediate states we obtain a relation for the imaginary part of \mathcal{M}

$$\begin{aligned} \langle i|T|b\rangle^* - \langle i|T|b\rangle &= \sum_f \int d\Pi_f \langle b|T^\dagger|f\rangle \langle f|T|i\rangle \\ i\mathcal{M}^*(i \rightarrow b) - i\mathcal{M}(i \rightarrow b) &= - \sum_f \int d\Pi_f (2\pi)^4 \delta^{(4)}(p_i - p_f) \mathcal{M}(i \rightarrow f) \mathcal{M}^*(b \rightarrow f) , \end{aligned} \quad (\text{A.5})$$

where $\sum_f \int d\Pi_f |f\rangle \langle f| = \mathbb{1}$ is the set of intermediate states and $d\Pi_f = \prod_{j \in \{f\}} \frac{d^3 \mathbf{k}_j}{(2\pi)^3} \frac{1}{2E_j}$ is the phase space of j intermediate particles. If the initial and final state are the same, the imaginary part of \mathcal{M} can be related to the sum over the intermediate states and we obtain the optical theorem:

$$2i \operatorname{Im} \mathcal{M}(i \rightarrow i) = i \sum_f \int d\Pi_f (2\pi)^4 \delta^{(4)}(p_i - p_f) |\mathcal{M}(i \rightarrow f)|^2. \quad (\text{A.6})$$

Looking at the right-hand side of A.6, we can see that it is very similar to the total cross section σ_{tot} or the total decay width Γ_{tot} , which have the form

$$\begin{aligned} \sigma_{\text{tot}}(i \rightarrow f) &= \frac{1}{4 E_{\text{CM}} |\mathbf{p}_{\text{CM}}|} \int d\Pi_f (2\pi)^4 \delta^{(4)}(p_i - p_f) |\mathcal{M}(i \rightarrow f)|^2 \\ \Gamma_{\text{tot}} = \sum_f \Gamma(i \rightarrow f) &= \frac{1}{2 m_i} \sum_f \int d\Pi_f (2\pi)^4 \delta^{(4)}(p_i - p_f) |\mathcal{M}(i \rightarrow f)|^2, \end{aligned} \quad (\text{A.7})$$

where the initial state i for the decay width is a one-particle state and for the cross section it is a two particle state. E_{CM} is the total energy in the center-of-mass frame and \mathbf{p}_{CM} is the 3-momentum of either of the initial particles for σ_{tot} in the CM frame.

If i in Equation (A.6) is a one-particle state, the optical theorem relates the imaginary part of the full propagator to the total decay width:

$$\Gamma_{\text{tot}} = \frac{1}{m_i} \operatorname{Im} \mathcal{M}(i \rightarrow i). \quad (\text{A.8})$$

On the other hand, if i is a two-particle state, it relates the total cross section to the imaginary part of the forward scattering amplitude:

$$\sigma_{\text{tot}}(i \rightarrow f) = \frac{1}{2 E_{\text{CM}} |\mathbf{p}_{\text{CM}}|} \operatorname{Im} \mathcal{M}(i \rightarrow i). \quad (\text{A.9})$$

Cutting rules

The optical theorem only holds for the total cross section and does not apply to individual Feynman diagrams. However, also for Feynman diagrams a similar relation for the imaginary part was derived in 1960 by Cutkolsky [93] and goes by the name cutting rules. They give the same result as the optical theorem for unitary theories, but they are also applicable to more general matrix elements, because their derivation does not rely on unitarity [94]. To calculate the imaginary part of a diagram, it is "cut" in all possible ways and the cut propagators are put on-shell.

Appendix B

Method of regions

Feynman diagrams with external momenta q_1, \dots, q_n , masses m_1, \dots, m_k and loop momenta k_1, \dots, k_m have integrals of the general form

$$\int d^d k_1 \dots d^d k_n f(k_1, \dots, k_m; q_1, \dots, q_n; m_1, \dots, m_k), \quad (\text{B.1})$$

where f is a function of the momenta and masses. For multi-loop diagrams, these integrals may be hard or even impossible to solve. The integral may simplify, however, if the external momenta and the masses have values in certain regions, for example large external momenta $q_i \rightarrow \infty$. The integrand f can then be expanded under the integral sign, the expression simplifies and the integration may become possible. This method was first investigated by Smirnov [32] and is called the method of regions.

To illustrate the principle, consider the following one-dimensional integral [95]

$$I = \int_0^\infty dk \frac{1}{k+m} \frac{1}{k+q} = \frac{\log(m/q)}{m-q}. \quad (\text{B.2})$$

This integral can be solved exactly and we will therefore be able to check if the result obtained with the method of regions is correct. Let's assume q is much larger than m and expand the result in m/q :

$$I = \frac{\log(m/q)}{m-q} = -\frac{\log(m/q)}{q} + \mathcal{O}(m/q). \quad (\text{B.3})$$

Now we will switch the order and expand under the integral sign. Looking at Equation (B.2), we see that expanding under the integral sign is not possible in this form, because k goes over the whole integration range from 0 to ∞ .

For expanding we first have to divide the integration range into different regions:

$$\begin{aligned} I &= \int_0^\infty dk \frac{1}{k+m} \frac{1}{k+q} \\ &= \int_0^\Lambda dk \frac{1}{k+m} \frac{1}{k+q} + \int_\Lambda^\infty dk \frac{1}{k+m} \frac{1}{k+q} \\ &= I_1 + I_2, \end{aligned} \quad (\text{B.4})$$

where Λ is chosen such that $m \ll \Lambda \ll q$. Λ is an artificial parameter and since I does not depend on Λ , it should vanish in the endresult.

Since $k \ll q$ in the whole integration range of I_1 and $k \gg m$ in I_2 , we can now expand under the

integral and subsequently do the integration:

$$\begin{aligned} I_1 &= \int_0^\Lambda dk \left[\frac{1}{q} \frac{1}{k+m} + \mathcal{O}(k/q) \right] = \frac{\log(\Lambda/m)}{q} + \mathcal{O}(m/\Lambda) + \mathcal{O}(m/q) \\ I_2 &= \int_\Lambda^\infty dk \left[\frac{1}{k} \frac{1}{k+q} + \mathcal{O}(m/k) \right] = \frac{\log(q/\Lambda)}{q} + \mathcal{O}(\Lambda/q) + \mathcal{O}(m/q) . \end{aligned} \quad (\text{B.5})$$

Adding I_1 and I_2 , the dependence on Λ vanishes and we obtain the first term of the expansion of I from Equation (B.3):

$$I = I_1 + I_2 = \frac{\log(q/m)}{q} + \mathcal{O}(m/q) + \mathcal{O}(m/\Lambda) + \mathcal{O}(\Lambda/q) . \quad (\text{B.6})$$

Expanding before the integration can simplify integrals enormously. However, note that we introduced the scale Λ as a cutoff in the process. Feynman integrals with a cutoff are in general much more complicated to solve than integrals in dimensional regularization.

Let's see how this procedure can be translated to dimensional regularization. First, we continue to $D = 1 - 2\varepsilon$ dimensions, which give

$$I = \mu^{2\varepsilon} \int_0^\infty dk k^{-2\varepsilon} \frac{1}{k+m} \frac{1}{k+q} . \quad (\text{B.7})$$

I_1 and I_2 can be rewritten in the form

$$\begin{aligned} I_1 &= \int_0^\infty dk \frac{1}{q} \frac{1}{k+m} - \int_\Lambda^\infty dk \frac{1}{q} \frac{1}{k+m} + \dots \\ I_2 &= \int_0^\infty dk \frac{1}{k} \frac{1}{k+q} - \int_0^\Lambda dk \frac{1}{k} \frac{1}{k+q} + \dots , \end{aligned} \quad (\text{B.8})$$

where the dots represent higher order terms. The second integral in both lines can be expanded again, giving

$$\begin{aligned} I_1 &= \int_0^\infty dk \frac{1}{q} \frac{1}{k+m} - \int_\Lambda^\infty dk \frac{1}{q} \frac{1}{k} + \dots \\ I_2 &= \int_0^\infty dk \frac{1}{k} \frac{1}{k+q} - \int_0^\infty dk \frac{1}{q} \frac{1}{k} + \dots . \end{aligned} \quad (\text{B.9})$$

Adding I_1 and I_2 , and continuing to D dimensions gives

$$\begin{aligned} I &= I_1 + I_2 \\ &= \mu^{2\varepsilon} \int_0^\infty k^{-2\varepsilon} \left(\frac{1}{q} \frac{1}{k+m} + \frac{1}{k} \frac{1}{k+q} \right) + \mu^{2\varepsilon} \int_0^\infty \frac{1}{q} \frac{1}{k^{1+2\varepsilon}} + \dots . \end{aligned} \quad (\text{B.10})$$

The second integral is scaleless and therefore zero in dimensional regularization. The remaining integral is independent of the cutoff and can be solved in dimensional regularization. Integrating and taking the limit $\varepsilon \rightarrow 0$ gives

$$\begin{aligned}
I &= \left(\frac{1}{2\varepsilon q} + \frac{\log(\mu/m)}{q} \right) + \left(-\frac{1}{2\varepsilon q} + \frac{\log(q/\mu)}{q} \right) + \mathcal{O}(\varepsilon) + \mathcal{O}(m/q) \\
&= \frac{\log(q/m)}{q} + \mathcal{O}(\varepsilon) + \mathcal{O}(m/q) .
\end{aligned} \tag{B.11}$$

Both I_1 and I_2 have a divergence, coming from taking the cutoff to infinity and 0, respectively, but they cancel in the final result along with the μ -dependence.

This example illustrated the general principle of the method of regions. It can be summarized as follows:

- Identify all relevant regions (= scales) of the integrand.
(in the example above: m and q)
- Divide the integral domain into different regions such that each loop momentum is of order of one of the scales.
(Equation (B.4))
- Taylor expand in each region in the parameters which are small in this region.
(Equation (B.5))
- Integrate *over the whole* integration range.
(Equation (B.10))

Determining the relevant regions can be a non-trivial task. A good indicator for the correct regions are the locations of the propagator poles [96].

The method of region is a powerful tool, but a mathematical proof for it only exists for special cases [95]. It has been proven, for example, for diagrams with off-shell external particles with large momenta or masses [97]. For other regions, no general proof exists, but no counterexamples have been found when comparing known full diagrams with their expansions computed with the method of regions [95].

Appendix C

Derivation of the Schrödinger Green's Function

In this appendix we derive the solution for the Green's function G of the leading order non-relativistic Schrödinger equation

$$(H_0 + V(\mathbf{x}) - E) G(\mathbf{x}, \mathbf{y}) = \delta^{(3)}(\mathbf{x} - \mathbf{y}) , \quad (\text{C.1})$$

where $H_0 = -\nabla_x^2/m$ is the free Hamiltonian and $V(\mathbf{x})$ is the leading order Coulomb potential in position space. Perturbatively, G can be calculated from G_0 , the Green's function of the free Schrödinger equation

$$(H_0 - E) G_0(\mathbf{x}, \mathbf{y}) = \delta^{(3)}(\mathbf{x} - \mathbf{y}) . \quad (\text{C.2})$$

To find the perturbative solution, we rewrite Equation (C.1) with G_0

$$G(\mathbf{x}, \mathbf{y}) = G_0(\mathbf{x}, \mathbf{y}) - \int d^3\mathbf{x}_1 G_0(\mathbf{x}, \mathbf{x}_1) V(\mathbf{x}_1) G(\mathbf{x}_1, \mathbf{y}) , \quad (\text{C.3})$$

This equation can be proven by applying $(H_0 - E)$ to both sides and using Equation (C.2):

$$\begin{aligned} (H_0 - E) G(\mathbf{x}, \mathbf{y}) &= (H_0 - E) G_0(\mathbf{x}, \mathbf{y}) - \int d^3\mathbf{x}_1 \left[(H_0 - E) G_0(\mathbf{x}, \mathbf{x}_1) \right] V(\mathbf{x}_1) G(\mathbf{x}_1, \mathbf{y}) \\ (H_0 - E) G(\mathbf{x}, \mathbf{y}) &= \delta^{(3)}(\mathbf{x} - \mathbf{y}) - V(\mathbf{x}) G(\mathbf{x}, \mathbf{y}) \\ (H_0 + V(\mathbf{x}) - E) G(\mathbf{x}, \mathbf{y}) &= \delta^{(3)}(\mathbf{x} - \mathbf{y}) . \end{aligned} \quad (\text{C.4})$$

Solving Equation (C.3) perturbatively gives

$$\begin{aligned} G(\mathbf{x}, \mathbf{0}) &= G_0(\mathbf{x}, \mathbf{0}) - \int d^3\mathbf{x}_1 G_0(\mathbf{x}, \mathbf{x}_1) V(\mathbf{x}_1) G_0(\mathbf{x}_1, \mathbf{0}) \\ &\quad + \int d^3\mathbf{x}_1 d^3\mathbf{x}_2 G_0(\mathbf{x}, \mathbf{x}_1) V(\mathbf{x}_1) G_0(\mathbf{x}_1, \mathbf{x}_2) V(\mathbf{x}_2) G_0(\mathbf{x}_2, \mathbf{0}) - \dots \\ &= G_0(\mathbf{x}, \mathbf{0}) + G_1(\mathbf{x}, \mathbf{0}) + G_2(\mathbf{x}, \mathbf{0}) + \dots , \end{aligned} \quad (\text{C.5})$$

where G_0, G_1, \dots can be written in the form

$$\begin{aligned}
G_1(\mathbf{x}, \mathbf{0}) &= - \int d^3 \mathbf{x}_1 G_0(\mathbf{x}, \mathbf{x}_1) V(\mathbf{x}_1) G_0(\mathbf{x}_1, \mathbf{0}) \\
G_2(\mathbf{x}, \mathbf{0}) &= - \int d^3 \mathbf{x}_1 G_0(\mathbf{x}, \mathbf{x}_1) V(\mathbf{x}_1) G_1(\mathbf{x}_1, \mathbf{0}) \\
G_3(\mathbf{x}, \mathbf{0}) &= \dots
\end{aligned} \tag{C.6}$$

To find the solution of $G(\mathbf{x}, \mathbf{y})$ to all orders, we will first derive G_0, G_1, \dots separately and then show how the sum of all terms exponentiates. The solution for G_0 is

$$G_0(\mathbf{x}, \mathbf{0}) = \frac{m e^{imv|\mathbf{x}|}}{4\pi|\mathbf{x}|}, \tag{C.7}$$

where $v = \sqrt{E/m}$. It can be easily checked by plugging the result into Equation (C.2). For G_1 we need the Fourier transformation of the leading order Coulomb potential from Equation (3.140) to position space

$$V(\mathbf{x}) = -\frac{\alpha_s C_F}{|\mathbf{x}|}. \tag{C.8}$$

G_1 then takes the form

$$\begin{aligned}
G_1(\mathbf{x}, \mathbf{0}) &= - \int d^3 \mathbf{x}_1 G_0(\mathbf{x}, \mathbf{x}_1) V(\mathbf{x}_1) G_0(\mathbf{x}_1, \mathbf{0}) \\
&= \int d^3 \mathbf{x}_1 \frac{m e^{imv|\mathbf{x}-\mathbf{x}_1|}}{4\pi|\mathbf{x}-\mathbf{x}_1|} \frac{\alpha_s C_F}{|\mathbf{x}_1|} \frac{m e^{imv|\mathbf{x}_1|}}{4\pi|\mathbf{x}_1|} \\
&= \frac{i\alpha_s C_F}{2v} \frac{1}{x} \int_0^\infty dx_1 \left(e^{imv|x-x_1|} - e^{imv|x+x_1|} \right) \frac{m e^{imvx_1}}{4\pi x_1},
\end{aligned} \tag{C.9}$$

where in the last step the integration over the radial components of \mathbf{x}_1 was performed. The remaining integrand diverges for $x_1 \rightarrow 0$. To make it well-defined, $1/x_1$ can be expressed as

$$\frac{1}{4\pi x_1} = -i \frac{mv}{2\pi} \int_0^\infty dt e^{2imvx_1 t}, \tag{C.10}$$

where v has an infinitesimal positive imaginary part. Using Equation (C.10), Equation (C.9) takes the form

$$\begin{aligned}
G_1(\mathbf{x}, \mathbf{0}) &= -i \left(\frac{m^2 v}{2\pi} \right) \left(\frac{i\alpha_s C_F}{2v} \right) \frac{1}{x} \int_0^\infty dt \int_0^\infty dx_1 \left(e^{imv|x-x_1|} - e^{imv|x+x_1|} \right) e^{imvx_1(1+2t)} \\
&= -i \left(\frac{m^2 v}{2\pi} \right) \left(\frac{i\alpha_s C_F}{2v} \right) \frac{1}{2imvx} \int_0^\infty dt \frac{1}{t(1+t)} \left(e^{imvx(1+2t)} - e^{imvx} \right) \\
&= -i \left(\frac{m^2 v}{2\pi} \right) \int_0^\infty dt \left(\frac{i\alpha_s C_F}{2v} \right) \log \left(\frac{1+t}{t} \right) e^{imvx(1+2t)},
\end{aligned} \tag{C.11}$$

where in the last step a partial integration was performed. Using this result, G_2 can be calculated from G_1 by Equation (C.6). Since $G_1(\mathbf{x}, \mathbf{0})$ only depends on the norm of \mathbf{x} , the radial integration

is analogous to Equation (C.9). Taking the result from Equation (C.9), G_2 becomes

$$\begin{aligned}
G_2(\mathbf{x}, \mathbf{0}) &= \\
&= -i \left(\frac{m^2 v}{2\pi} \right) \left(\frac{i\alpha_s C_F}{2v} \right)^2 \frac{1}{x} \int_0^\infty dt \int_0^\infty dx_1 \log \left(\frac{1+t}{t} \right) \left(e^{imv|x-x_1|} - e^{imv|x+x_1|} \right) e^{imv x_1(1+2t)} \\
&= -i \left(\frac{m^2 v}{2\pi} \right) \left(\frac{i\alpha_s C_F}{2v} \right)^2 \frac{1}{2imvx} \int_0^\infty dt \frac{\log \left(\frac{1+t}{t} \right)}{t(1+t)} \left(e^{imvx(1+2t)} - e^{imvx} \right) \\
&= -i \left(\frac{m^2 v}{2\pi} \right) \int_0^\infty dt \frac{1}{2!} \left(\frac{i\alpha_s C_F}{2v} \right)^2 \log \left(\frac{1+t}{t} \right)^2 e^{imvx(1+2t)} . \tag{C.12}
\end{aligned}$$

The calculation is analogous to (C.11): first the x_1 integration was performed and then integration by parts was used.

The results for G_0 , G_1 , and G_2 from Equation (C.7), (C.11), and (C.12) follow the pattern

$$G_n(\mathbf{x}, \mathbf{0}) = -i \left(\frac{m^2 v}{2\pi} \right) \int_0^\infty dt \frac{1}{n!} \left(\frac{i\alpha_s C_F}{2v} \right)^n \log \left(\frac{1+t}{t} \right)^n e^{imvx(1+2t)} . \tag{C.13}$$

This pattern holds to all orders, as can be easily proven by induction. The result for the full Green's function therefore reads

$$\begin{aligned}
G(\mathbf{x}, \mathbf{0}) &= -i \left(\frac{m^2 v}{2\pi} \right) \int_0^\infty dt e^{imvx(1+2t)} \times \\
&\times \left[1 + \left(\frac{i\alpha_s C_F}{2v} \right) \log \left(\frac{1+t}{t} \right) + \frac{1}{2!} \left(\frac{i\alpha_s C_F}{2v} \right)^2 \log \left(\frac{1+t}{t} \right)^2 + \dots \right] \tag{C.14}
\end{aligned}$$

and exponentiates into the form

$$G(\mathbf{x}, \mathbf{0}) = -i \left(\frac{m^2 v}{2\pi} \right) \int_0^\infty dt \left(\frac{1+t}{t} \right)^{\frac{i\alpha_s C_F}{2v}} e^{imvx(1+2t)} . \tag{C.15}$$

Appendix D

Multiloop Integrals

$$I^{(2)}(\alpha, \beta, \gamma; m^2)$$

The integral

$$I^{(2)}(\alpha, \beta, \gamma; m^2) = \tilde{\mu}^{4\varepsilon} \int \frac{d^n k}{(2\pi)^n} \frac{d^n q}{(2\pi)^n} \frac{1}{(\mathbf{k}^2 - m^2 - i\varepsilon)^\alpha [(\mathbf{k} - \mathbf{q})^2 - i\varepsilon]^\beta (\mathbf{q}^2 - m^2 - i\varepsilon)^\gamma} \quad (D.1)$$

can be solved with Feynman parameters. Performing first the integral over \mathbf{q} gives:

$$\begin{aligned} I^{(2)} &= \tilde{\mu}^{4\varepsilon} \int \frac{d^n k}{(2\pi)^n} \frac{d^n q}{(2\pi)^n} \frac{1}{(\mathbf{k}^2 - m^2)^\alpha} \frac{\Gamma(\beta + \gamma)}{\Gamma(\beta) \Gamma(\gamma)} \int_0^1 dx \frac{x^{\beta-1} (1-x)^{\gamma-1}}{[\mathbf{q}^2 + \mathbf{k}^2 x(1-x) - m^2(1-x)]^{\beta+\gamma}} \\ &= \tilde{\mu}^{4\varepsilon} \int \frac{d^n k}{(2\pi)^n} \int_0^1 dx \frac{x^{\beta-1} (1-x)^{\gamma-1} x^{n/2-\beta-\gamma} (1-x)^{n/2-\beta-\gamma}}{(\mathbf{k}^2 - m^2/x)^{\beta+\gamma-n/2} (\mathbf{k}^2 - m^2)^\alpha}, \end{aligned} \quad (D.2)$$

where the $(-i\varepsilon)$ terms have been omitted for better readability. In the first line the second and third denominator were combined using the Feynman trick

$$\frac{1}{A^n B^m} = \frac{\Gamma(n+m)}{\Gamma(n) \Gamma(m)} \int_0^1 dx \frac{x^{n-1} (1-x)^{m-1}}{[Ax + B(1-x)]^{n+m}} \quad (D.3)$$

and subsequently changing the integration variable $q \rightarrow q + kx$. The integration variable \mathbf{k} then only appears once in the denominator and the integral over \mathbf{q} can be solved with the standard relation (see e.g. [14])

$$\begin{aligned} I^{(1)}(\alpha; m^2) &= \tilde{\mu}^{2\varepsilon} \int \frac{d^n k}{(2\pi)^n} \frac{1}{(\mathbf{k}^2 - m^2 - i\varepsilon)^\alpha} \\ &= \tilde{\mu}^{2\varepsilon} \frac{1}{(4\pi)^{n/2}} \frac{\Gamma(\alpha - n/2)}{\Gamma(\alpha)} \frac{1}{(-m^2 - i\varepsilon)^{\alpha-n/2}} \end{aligned} \quad (D.4)$$

Repeating the same procedure for the \mathbf{k} integration, one obtains after combining the denominators and performing the \mathbf{k} integration with Equation (D.4)

$$\begin{aligned} I^{(2)} &= \tilde{\mu}^{4\varepsilon} \frac{\Gamma(\alpha + \beta + \gamma - n)}{(4\pi)^n \Gamma(\alpha) \Gamma(\beta) \Gamma(\gamma)} \times \\ &\times \int_0^1 dx \int_0^1 dy \frac{x^{n/2-\gamma-1} (1-x)^{n/2-\beta-1} y^{\beta+\gamma-n/2-1} (1-y)^{\alpha-1}}{[-m^2/x(y+x(1-y))]^{\alpha+\beta+\gamma-n}}. \end{aligned} \quad (D.5)$$

Changing the integration variables to $x \rightarrow (1 - x)$ and $y \rightarrow (1 - y)$, Equation (D.5) becomes

$$\begin{aligned} I^{(2)} = & \tilde{\mu}^{4\varepsilon} (-m^2)^{n-\alpha-\beta-\gamma} \frac{\Gamma(\alpha + \beta + \gamma - n)}{(4\pi)^n \Gamma(\alpha) \Gamma(\beta) \Gamma(\gamma)} \int_0^1 dy (1 - y)^{\beta+\gamma-n/2-1} y^{\alpha-1} \times \\ & \times {}_2F_1(n - \alpha - \beta - \gamma, n/2 - \beta; \alpha; y) \frac{\Gamma(n/2 - \beta) \Gamma(\alpha + \beta - n/2)}{\Gamma(\alpha)}, \end{aligned} \quad (D.6)$$

where ${}_2F_1$ is the ordinary hypergeometric function defined as

$$\frac{\Gamma(b) \Gamma(c - b)}{\Gamma(c)} {}_2F_1(a, b; c; z) = \int_0^1 dx x^{b-1} (1 - x)^{c-b-1} (1 - zx)^{-a}. \quad (D.7)$$

Performing the remaining integral of Equation (D.6) with Mathematica finally gives

$$\begin{aligned} I^{(2)}(\alpha, \beta, \gamma; m^2) = & \tilde{\mu}^{4\varepsilon} \frac{(-m^2 - i\varepsilon)^{n-\alpha-\beta-\gamma}}{(4\pi)^n} \times \\ & \times \frac{\Gamma(n - \alpha - \beta - \gamma) \Gamma(\alpha + \beta - n/2) \Gamma(\beta + \gamma - n/2) \Gamma(n/2 - \beta)}{\Gamma(\alpha + 2\beta + \gamma - n) \Gamma(n/2) \Gamma(\alpha) \Gamma(\gamma)}, \end{aligned} \quad (D.8)$$

where the $(-i\varepsilon)$ term has been restored.

For $\alpha = \beta = \gamma = 0$, this integral arises when calculating the vacuum polarization with one insertion of the leading order Coulomb potential. Its expansion for $n = 3 - 2\varepsilon$ dimensions is

$$I^{(2)}(1, 1, 1; Em) = \frac{1}{32\pi^2} \left[\frac{1}{2\varepsilon} + 1 + \log\left(\frac{\mu^2}{m^2}\right) - 2\log(-iv) - 2\log 2 \right] + \mathcal{O}(\varepsilon), \quad (D.9)$$

where $v^2 = E/m$.

For $\alpha = 1$, $\gamma = 1$, and general β it can be used to compute insertions of the higher order effective Coulomb potential $V_{c,\text{eff}}$, see section 5.3.

$$I^{(3)}(1, \beta, 1, 1, 1; m^2)$$

The three-loop integral

$$I^{(3)}(1, \beta, 1, 1, 1; m^2) = \tilde{\mu}^{6\varepsilon} \int \frac{d^n k}{(2\pi)^n} \frac{d^n l}{(2\pi)^n} \frac{d^n q}{(2\pi)^n} \times \frac{1}{(\mathbf{k}^2 - m^2 - i\varepsilon)[(\mathbf{k} - \mathbf{l})^2 - i\varepsilon]^\beta (\mathbf{l}^2 - m^2 - i\varepsilon)[(\mathbf{k} - \mathbf{q})^2 - i\varepsilon](\mathbf{q}^2 - m^2 - i\varepsilon)} \quad (D.10)$$

can be solved by reducing it to simpler integrals with integration by parts (IBP). IBP in the context of Feynman integrals refers to the fact, that in dimensional regularization the integral over the derivative of a function is zero:

$$\int \frac{d^d q}{(2\pi)^d} \frac{\partial}{\partial q^\mu} f(q) = 0, \quad (D.11)$$

i.e. that the surface terms are zero [98, 99].

Using IBP we obtain the relation

$$\begin{aligned} 0 &= \int \frac{d^n q}{(2\pi)^n} \frac{\partial}{\partial q^\mu} \left[\frac{(\mathbf{l} - \mathbf{q})^\mu}{(\mathbf{k}^2 - m^2)(\mathbf{k} - \mathbf{l})^{2\beta}(\mathbf{l}^2 - m^2)(\mathbf{l} - \mathbf{q})^2(\mathbf{q}^2 - m^2)} \right] \\ &= \int \frac{d^n q}{(2\pi)^n} \left[\frac{-n}{(\mathbf{k}^2 - m^2)(\mathbf{k} - \mathbf{l})^{2\beta}(\mathbf{l}^2 - m^2)(\mathbf{l} - \mathbf{q})^2(\mathbf{q}^2 - m^2)} \right. \\ &\quad \left. + \frac{2(\mathbf{l} - \mathbf{q})^2}{(\mathbf{k}^2 - m^2)(\mathbf{k} - \mathbf{l})^{2\beta}(\mathbf{l}^2 - m^2)(\mathbf{l} - \mathbf{q})^4(\mathbf{q}^2 - m^2)} \right. \\ &\quad \left. + \frac{-2\mathbf{q} \cdot (\mathbf{l} - \mathbf{q})}{(\mathbf{k}^2 - m^2)(\mathbf{k} - \mathbf{l})^{2\beta}(\mathbf{l}^2 - m^2)(\mathbf{l} - \mathbf{q})^2(\mathbf{q}^2 - m^2)^2} \right] \\ &= (3 - n) I^{(3)}(1, \beta, 1, 1, 1) + I^{(3)}(1, \beta, 1, 0, 2) - I^{(3)}(1, \beta, 0, 1, 2), \end{aligned} \quad (D.12)$$

where the relation

$$2\mathbf{q} \cdot (\mathbf{l} - \mathbf{q}) = -(\mathbf{l} - \mathbf{q})^2 + (\mathbf{l}^2 - m^2) - (\mathbf{q}^2 - m^2) \quad (D.13)$$

was used in the last step.

The full integral now reduces to

$$I^{(3)}(1, \beta, 1, 1, 1) = \frac{1}{n-3} \left[I^{(3)}(1, \beta, 1, 0, 2) - I^{(3)}(1, \beta, 0, 1, 2) \right]. \quad (D.14)$$

The first integral decomposes into two independent integrals, which we already know:

$$\begin{aligned} I^{(3)}(1, \beta, 1, 0, 2) &= \tilde{\mu}^{6\varepsilon} \int \frac{d^n k}{(2\pi)^n} \frac{d^n l}{(2\pi)^n} \frac{d^n q}{(2\pi)^n} \frac{1}{(\mathbf{k}^2 - m^2)(\mathbf{k} - \mathbf{l})^{2\beta}(\mathbf{l}^2 - m^2)(\mathbf{q}^2 - m^2)^2} \\ &= I^{(2)}(1, \beta, 1; m^2) \cdot I^{(1)}(2). \end{aligned} \quad (D.15)$$

$I^{(1)}$ and $I^{(2)}$ were calculated in Equation (D.8) and (D.4), respectively.

The second integral from Equation (D.14) has the form

$$I^{(3)}(1, \beta, 0, 1, 2) = \tilde{\mu}^{6\varepsilon} \int \frac{d^n k}{(2\pi)^n} \frac{d^n q}{(2\pi)^n} \frac{1}{(\mathbf{k}^2 - m^2)(\mathbf{q}^2 - m^2)^2} \int \frac{d^n l}{(2\pi)^n} \frac{1}{(\mathbf{k} - \mathbf{l})^2(\mathbf{l} - \mathbf{q})^2}. \quad (\text{D.16})$$

The last integral can be solved by first shifting $\mathbf{l} \rightarrow \mathbf{l} + \mathbf{q}$. Then the standard procedure is used: the denominators are combined using Feynman parameters (Equation (D.3)) and the integral over \mathbf{l} is solved with Equation (D.4). The result is

$$\int \frac{d^n l}{(2\pi)^n} \frac{1}{(\mathbf{k} - \mathbf{l})^2(\mathbf{l} - \mathbf{q})^2} = \frac{1}{(\mathbf{k} - \mathbf{q})^{2(1+\beta-n/2)}} \frac{\Gamma(1+\beta-n/2) \Gamma(n/2-1) \Gamma(n/2-\beta)}{\Gamma(\beta) \Gamma(n-\beta-1) (4\pi)^{n/2}}. \quad (\text{D.17})$$

Plugging this result into Equation (D.16), we see that the remaining integral is of the form

$$\begin{aligned} I^{(3)}(1, \beta, 0, 1, 2) &= \tilde{\mu}^{6\varepsilon} \frac{\Gamma(1+\beta-n/2) \Gamma(n/2-1) \Gamma(n/2-\beta)}{\Gamma(\beta) \Gamma(n-\beta-1) (4\pi)^{n/2}} \times \\ &\quad \times \int \frac{d^n k}{(2\pi)^n} \frac{d^n q}{(2\pi)^n} \frac{1}{(\mathbf{k}^2 - m^2) (\mathbf{k} - \mathbf{q})^{2(1+\beta-n/2)} (\mathbf{q}^2 - m^2)^2} \\ &= \tilde{\mu}^{2\varepsilon} \frac{\Gamma(1+\beta-n/2) \Gamma(n/2-1) \Gamma(n/2-\beta)}{\Gamma(\beta) \Gamma(n-\beta-1) (4\pi)^{n/2}} I^{(2)}(1, 1+\beta-n/2, 2; m^2). \end{aligned} \quad (\text{D.18})$$

Combining Equation (D.15) and (D.18) in Equation (D.14), and using the previous results for $I^{(1)}$ and $I^{(2)}$, the final result reads

$$\begin{aligned} I^{(3)}(1, \beta, 1, 1, 1; m^2) &= \tilde{\mu}^{6\varepsilon} \frac{(-m^2 - i\varepsilon)^{3n/2-4-\beta}}{(4\pi)^{3n/2}} \frac{\Gamma(1+\beta-\frac{n}{2}) \Gamma(\frac{n}{2}-\beta)}{(n-3) \Gamma(\frac{n}{2})} \times \\ &\quad \left[\frac{\Gamma(2+\beta-n) \Gamma(1+\beta-\frac{n}{2}) \Gamma(2-\frac{n}{2})}{\Gamma(2+2\beta-n)} - \frac{\Gamma(\frac{n}{2}-1) \Gamma(4+\beta-\frac{3n}{2}) \Gamma(3+\beta-n) \Gamma(2+\beta-n)}{\Gamma(5+2\beta-2n) \Gamma(\beta)} \right]. \end{aligned} \quad (\text{D.19})$$

For $\beta = 1$, this integral appears when calculating the vacuum polarization with two insertions of the lowest order Coulomb potential. Expanding in $n = 3 - 2\varepsilon$ gives

$$I^{(3)}(1, 1, 1, 1, 1; Em) = \frac{1}{3 \cdot 4^4 \cdot \pi \sqrt{-Em}} + \mathcal{O}(\varepsilon). \quad (\text{D.20})$$

In contrast to $I^{(2)}$ in Equation (D.9), $I^{(3)}$ has no divergent term.

For $\beta \neq 1$, Equation (D.20) can be used to calculate diagrams with two potential insertions: one Coulomb insertion of order α_s/v , and one higher order potential insertion of order $\alpha_s v$, see section 5.3.

Appendix E

Running of the Strong Coupling α_s

In the $\overline{\text{MS}}$ scheme, the strong coupling constant α_s is renormalized by absorbing only the divergent terms of vacuum polarization, self-energy and vertex diagrams. From the μ -independence of the bare coupling α_s^0 , the RGE for α_s in the $\overline{\text{MS}}$ scheme can be derived. Using dimensional regularization with $d = 4 - 2\varepsilon$ the RGE in the limit $\varepsilon \rightarrow 0$ has the form [1]:

$$\mu \frac{d}{d\mu} \alpha_s^{(n_f)}(\mu) = -\varepsilon \alpha_s^{(n_f)} - 2 \alpha_s^{(n_f)} \left[\left(\frac{\alpha_s^{(n_f)}}{4\pi} \right) \beta_0^{(n_f)} + \left(\frac{\alpha_s^{(n_f)}}{4\pi} \right)^2 \beta_1^{(n_f)} + \left(\frac{\alpha_s^{(n_f)}}{4\pi} \right)^3 \beta_2^{(n_f)} + \dots \right], \quad (\text{D.1})$$

where $\beta_0^{(n_f)} = 11 - \frac{2}{3}n_f$ and n_f is the number of active flavors. The other β -coefficients up to $\beta_4^{(n_f)}$ can be found in [100]. The term $\varepsilon \alpha_s$ is set to zero when calculating the running for α_s , but it has to be included when the RGE of α_s is used to calculate the running of other quantities, as for example the running of the $\overline{\text{MS}}$ mass or the Wilson coefficients of the potentials in Section 3.3.4. In this thesis we use the four-loop running of α_s with the β -coefficients up to $\beta_3^{(n_f)}$.

Equation (D.1) can be solved by separation of variables, subsequent integration and finally expanding the result perturbatively in α_s . The solution reads

$$\begin{aligned} \frac{1}{\alpha_1} = \frac{x}{\alpha_0} + \frac{\beta_1}{4\pi\beta_0} \log x + \frac{\alpha_0}{16\pi^2} \left[\frac{\beta_1^2}{\beta_0^2} \left(\frac{\log x}{x} + \frac{1}{x} - 1 \right) + \frac{\beta_2}{\beta_0} \left(1 - \frac{1}{x} \right) \right] \\ + \frac{\alpha_0^2}{128\pi^3 x^2} \left[\frac{\beta_1^3}{\beta_0^3} ((x-1)^2 - \log^2 x) + \frac{2\beta_1\beta_2}{\beta_0^2} (x - x^2 + \log x) - \frac{\beta_3}{\beta_0} (1 - x^2) \right], \quad (\text{D.2}) \end{aligned}$$

where $\alpha_0 = \alpha_s^{(n_f)}(\mu_0)$, $\alpha_1 = \alpha_s^{(n_f)}(\mu_1)$, $x = 1 + \alpha_0 \frac{\beta_0}{2\pi} \log\left(\frac{\mu_1}{\mu_0}\right)$, and the n_f superscripts on the β -coefficients have been suppressed. This solution resums logarithms of μ_1/μ_0 to all orders in α_s , as can be seen from the expansion in α_0 of the leading order term x/α_0 from Equation (D.2):

$$\alpha_1 = \alpha_0 \left[1 + \frac{\beta_0}{2\pi} \alpha_0 \log\left(\frac{\mu_0}{\mu_1}\right) + \left(\frac{\beta_0}{2\pi} \alpha_0 \log\left(\frac{\mu_0}{\mu_1}\right) \right)^2 + \dots \right]. \quad (\text{D.3})$$

This equation includes the leading logarithmic contributions of the form $\alpha_s \sum_{n=0}^{\infty} (\alpha_s \log(\mu_0/\mu_1))^n$. To resum subleading logarithmic terms, higher loop orders in the running have to be used. For example, the next-to-leading order logarithmic contributions are of the form $\alpha_s^2 \sum_{n=0}^{\infty} (\alpha_s \log(\mu_0/\mu_1))^n$ and need the two-loop running.

In perturbative calculations, μ is usually set to the typical energy scale of the problem to avoid large logarithms of the form shown in Equation (D.3).

Flavor Thresholds

When a perturbative calculation in $\alpha_s^{(n_f)}(\mu)$ only involves energy scales larger than the top mass, μ

When a perturbative calculation only involves energy scales far below a heavy quark with mass m_h , the coupling has to be evolved to this scale and one would expect that the running of the coupling becomes independent of m_h . This is indeed the case in other renormalization schemes, as for example the momentum subtraction scheme, but in the $\overline{\text{MS}}$ scheme the dependence does not vanish. Instead, the heavy quark flavor is integrated out by hand and the running coupling is then calculated in an effective theory without the heavy quark. $\alpha_s^{(n_f)}$ therefore depends on the number of active flavors n_f , which in turn is determined by μ . The connection between $\alpha_s^{(n_f)}$ and $\alpha_s^{(n_f-1)}$ at the scale $\mu = m_h$ can be calculated through their relations to the bare coupling α_s^0 and gives [101]:

$$\alpha_s^{(n_f)}(m_h) = \alpha_s^{(n_f-1)}(m_h) + \frac{7\pi}{24} \left(\frac{\alpha_s^{(n_f-1)}(m_h)}{\pi} \right)^3 + \mathcal{O} \left[\left(\alpha_s^{(n_f-1)} \right)^4 \right]. \quad (\text{D.4})$$

In this thesis we only need the relation with corrections up to α_s^3 as given here. Higher order corrections up to α_s^5 and can be found in [101, 102].

Appendix F

Expansions of the QCD and the vNRQCD Cross Section

In this appendix we summarize the expansions of the QCD cross section described in Chapter 2 and the vNRQCD as presented in Chapter 3. We use the pole mass scheme for both cross sections, the expanded terms in the MSR mass scheme can be found in Chapter 5. The QCD cross section at N³LO (i.e. at $\mathcal{O}(\alpha_h^3)$) is expanded in $v = \sqrt{(q - 2m + i\varepsilon)/m}$ and the vNRQCD cross section up to NNLL is expanded in α_h/v and $\alpha_h \log v$. The following tables summarize the overlapping contributions of the two cross sections. We use the following abbreviations

$$\alpha_h = \alpha_s(\mu_h) , \quad L_V = \log v , \quad L_\nu = \log \nu , \quad L_{\mu m} = \log \left(\frac{\mu}{m_{\text{pole}}} \right) , \quad (\text{D.1})$$

where $\mu_h = hm_{\text{pole}}$ is the hard scale and we expand all Wilson coefficients of the vNRQCD cross section in α_h . The vNRQCD cross section also contains two types of terms beyond NNLL, which are suppressed at threshold. These are on the one hand logarithms generated by the running of the Wilson coefficients, as for example $(-0.43 - 5.6i) \alpha_h^3 v^2 L_\nu$ (see Table F.4), which is of N³LL order. On the other hand, the Wilson coefficients also generate off-shell terms, which are real for stable top quarks and would drop out of the final cross section for $\Gamma_t = 0$. An example would be the term $(-3.2) \alpha_h^2 v^2 L_\nu$ from Table F.3. For $\Gamma_t \neq 0$ these contributions are suppressed by about a factor Γ_t/m compared to the on-shell NNLL terms. Only the on-shell NNLL give the correct contributions at threshold and the off-shell terms as well as the terms beyond NNLL are therefore not considered when comparing the vNRQCD and QCD cross section. In Tables F.3 and F.4 we wrote all on-shell NNLL terms in black and the off-shell as well as higher order terms in gray. For the QCD cross section in Tables F.1 and F.2 we wrote all orders in black that also appear in the vNRQCD NNLL cross section.

	α_h^0	α_h^1	α_h^2
$v^1 \left(\frac{\alpha_h}{v} \right)^i$	$v (2.i)$	$\alpha_h [4.18879i - 2.66667 L_V]$	$\alpha_h^2/v (2.92433i)$
$v^2 \left(\frac{\alpha_h}{v} \right)^i$	$v^2 (-0.565884)$	$\alpha_h v (-3.39531i)$	$\alpha_h^2 \left[(-9.06127i) + (-5.11111i) L_{\mu m} \right. \\ \left. + ((5.76858 - 5.11111i) - 3.25383 L_{\mu m}) L_V + 1.62692 L_V^2 \right]$
$v^3 \left(\frac{\alpha_h}{v} \right)^i$	$v^3 (0.583333i)$	$\alpha_h v^2 [(-5.09206 + 6.98132i) - 4.44444 L_V]$	$\alpha_h^2 v [(-16.2897 + 4.60874i) - (4.14291i) L_{\mu m} - (10.3704i) L_V]$
$v^4 \left(\frac{\alpha_h}{v} \right)^i$	$v^4 (-0.141471)$	$\alpha_h v^3 [(7.11111 - 4.39441i) + (4.52707i) L_V]$	$\alpha_h^2 v^2 \left[(36.2564 - 30.792i) - (6.21327 - 8.51852i) L_{\mu m} \right. \\ \left. + (-5.42306 L_{\mu m} + (19.6028 - 6.81481i)) L_V + 2.16922 L_V^2 \right]$
$v^5 \left(\frac{\alpha_h}{v} \right)^i$	$v^5 (0.192708i)$	$\alpha_h v^4 [(-2.23327 + 0.349066i) - 0.222222 L_V]$	$\alpha_h^2 v^3 \left[(-38.5761 + 69.8969i) + (8.67689 - 5.36201i) L_{\mu m} \right. \\ \left. + ((-17.3538 - 24.5583i) + (5.52388i) L_{\mu m}) L_V + (-5.52388i) L_V^2 \right]$
$v^6 \left(\frac{\alpha_h}{v} \right)^i$	$v^6 (-0.113177)$	$\alpha_h v^5 [(-0.414815 - 0.890636i) - (0.264079i) L_V]$	$\alpha_h^2 v^4 \left[(-172.076 + 11.3068i) - (2.72501 - 0.425926i) L_{\mu m} \right. \\ \left. + ((-7.1981 + 6.24691i) - 0.271153 L_{\mu m}) L_V - 1.98845 L_V^2 \right]$

Table F.1: ϱ_{QCD} expanded in v up to order α_h^2 . The abbreviations and colorings are explained in the text.

	α_h^3
$v^1 \left(\frac{\alpha_h}{v}\right)^i$	$\alpha_h^3/v^2 (-1.42466)$
$v^2 \left(\frac{\alpha_h}{v}\right)^i$	$\alpha_h^3/v \left[(-11.2099 - 12.9025i) + (7.13646i) L_{\mu m} - (7.13646i) L_V\right]$
$v^3 \left(\frac{\alpha_h}{v}\right)^i$	$\alpha_h^3 \left[(7.60697i) + (-20.0616i) L_{\mu m} + (6.23652i) L_{\mu m}^2 \right. \\ \left. + ((1.68812 - 10.335i) + (12.7716 - 12.473i) L_{\mu m} - 3.97029 L_{\mu m}^2) L_V + ((3.28972 + 6.23652i) + 3.97029 L_{\mu m}) L_V^2 - 1.32343 L_V^3 \right]$
$v^4 \left(\frac{\alpha_h}{v}\right)^i$	$\alpha_h^3 v \left[(12.6918 + 45.569i) - (39.7531 - 9.5843i) L_{\mu m} - (5.05513i) L_{\mu m}^2 + ((-15.8812 + 8.07986i) - (25.3076i) L_{\mu m}) L_V - (5.05513i) L_V^2 \right]$
$v^5 \left(\frac{\alpha_h}{v}\right)^i$	$\alpha_h^3 v^2 \left[(-310.311 + 16.329i) + (85.9855 - 71.7252i) L_{\mu m} - (7.58136 - 10.3942i) L_{\mu m}^2 \right. \\ \left. + ((2.66638 - 21.2435i) + (45.6617 - 16.6307i) L_{\mu m} - 6.61715 L_{\mu m}^2) L_V + (5.29372 L_{\mu m} + (6.76202 + 12.473i)) L_V^2 - 2.64686 L_V^3 \right]$
$v^6 \left(\frac{\alpha_h}{v}\right)^i$	$\alpha_h^3 v^3 \left[(27.8926 - 837.298i) - (90.6578 - 168.423i) L_{\mu m} + (10.5874 - 6.54266i) L_{\mu m}^2 \right. \\ \left. + ((-60.9385 - 15.5045i) - (42.3498 + 57.7146i) L_{\mu m} + (6.74017i) L_{\mu m}^2) L_V + ((31.7623 - 19.3973i) - (13.4803i) L_{\mu m}) L_V^2 + (6.74017i) L_V^3 \right]$

Table F.2: ϱ_{QCD} expanded in v at order α_h^3 . The abbreviations and colorings are explained in the text.

	α_h^0	α_h^1	α_h^2
$v^1 \left(\frac{\alpha_h}{v}\right)^i$	$v(2.i)$	$\alpha_h[4.18879i - 2.66667 L_V]$	$\alpha_h^2/v(2.92433i)$
$v^2 \left(\frac{\alpha_h}{v}\right)^i$	0	$\alpha_h v(-3.39531i)$	$\alpha_h^2[(-9.06127i) + (5.11111i) L_{\mu m}$ $+ ((5.76858 - 5.11111i) - 3.25383 L_{\mu m}) L_V + 1.62692 L_V^2]$
$v^3 \left(\frac{\alpha_h}{v}\right)^i$	$v^3(0.583333i)$	$\alpha_h v^2[(0.586013 + 6.98132i) - 4.44444(L_V - L_\nu - L_{\mu m})]$	$\alpha_h^2 v[(-16.2897 + 4.60874i) - (4.14291i) L_{\mu m} - (10.3704i) L_V]$
$v^4 \left(\frac{\alpha_h}{v}\right)^i$	0	$\alpha_h v^3(4.52707i) L_\nu$	$\alpha_h^2 v^2[(4.00835 L_{\mu m} + (-3.17331 + 6.2963i)) L_\nu$ $+ (4.00835 L_\nu^2 - 4.00835 L_\nu L_V)]$
$v^5 \left(\frac{\alpha_h}{v}\right)^i$	0	0	$\alpha_h^2 v^3(-5.52388i) L_\nu^2$
$v^6 \left(\frac{\alpha_h}{v}\right)^i$	0	0	0

Table F.3: ϱ_{vNRQCD} expanded in α_h/v : terms of order α_h^0 , α_h^1 , α_h^2 . The abbreviations and colorings are explained in the text.

	α_h^3
$v^1 \left(\frac{\alpha_h}{v}\right)^i$	$\alpha_h^3/v^2 (-1.42466)$
$v^2 \left(\frac{\alpha_h}{v}\right)^i$	$\alpha_h^3/v \left[(-11.2099 - 12.9025i) + (7.13646i) L_{\mu m} - (7.13646i) L_V\right]$
$v^3 \left(\frac{\alpha_h}{v}\right)^i$	$\alpha_h^3 \left[(7.60697i) - (20.0616i) L_{\mu m} + (6.23652i) L_{\mu m}^2 \right. \\ \left. + ((1.68812 - 10.335i) + (12.7716 - 12.473i) L_{\mu m} - 3.97029 L_{\mu m}^2) L_V + ((3.28972 + 6.23652i) + 3.97029 L_{\mu m}) L_V^2 - 1.32343 L_V^3 \right]$
$v^4 \left(\frac{\alpha_h}{v}\right)^i$	$\alpha_h^3 v \left[((-7.35802 - 49.9713i) - (25.3076i) L_{\mu m}) L_\nu + ((2.34213i) L_\nu^2 - (4.68426i) L_\nu L_V) \right]$
$v^5 \left(\frac{\alpha_h}{v}\right)^i$	$\alpha_h^3 v^2 \left[((-0.430697 - 5.5594i) - 3.53923 L_{\mu m}) L_\nu \right. \\ \left. + ((2.14009 - 29.0134i) L_\nu^2 - 18.4705 L_{\mu m} L_\nu^2 + 3.53923 L_\nu L_V) + (-18.4705 L_\nu^3 + 18.4705 L_\nu^2 L_V) \right]$
$v^6 \left(\frac{\alpha_h}{v}\right)^i$	$\alpha_h^3 v^3 (8.9869i) L_\nu^3$

Table F.4: ϱ_{vNRQCD} expanded in α_h/v : terms of order α_h^3 . The abbreviations and colorings are explained in the text.

Appendix G

Coefficients of the Expanded Cross Section

As described in Section 5.3, the contributions to the fixed-order expanded cross section can be written in the form

$$\varrho_{\text{exp}}^{\text{FO}} = \sum_{i=1}^{n_{\text{max}}} \sum_{j=0}^{n_{\text{max}}} v^i \left(\frac{\alpha_h}{v} \right)^j b_{ij}(m, \mu_h, v) . \quad (\text{D.1})$$

and for the RGI expanded cross section in the form

$$\begin{aligned} \varrho_{\text{exp}}^{\text{LL}} &= \varrho_{\text{exp}}^{\text{LO}} \\ \varrho_{\text{exp}}^{\text{NLL}} &= \varrho_{\text{exp}}^{\text{NLO}} + v^2 \left(\frac{\alpha_h}{v} \right) c_{211}(L) \alpha_h \\ \varrho_{\text{exp}}^{\text{NNLL}} &= \varrho_{\text{exp}}^{\text{NNLO}} + v^2 \left(\frac{\alpha_h}{v} \right) c_{212}(L) \alpha_h^2 + v^3 \sum_{j=0}^2 \sum_{k=1}^{3-j} \left(\frac{\alpha_h}{v} \right)^j c_{3jk}(L) \alpha_h^k . \end{aligned} \quad (\text{D.2})$$

In the pole mass scheme, the coefficients for the fixed-order expanded cross section are

$$\begin{aligned} b_{10}^{\text{pole}} &= 2.i \\ b_{20}^{\text{pole}} &= 0 \\ b_{30}^{\text{pole}} &= 0.583333i \\ b_{11}^{\text{pole}} &= 4.18879i - 2.66667 L_V \\ b_{21}^{\text{pole}} &= -3.39531i \\ b_{31}^{\text{pole}} &= [(0.586013 + 6.98132i) + 4.44444 L_{\mu m}^{\text{pole}}] - 4.44444 L_V \\ b_{12}^{\text{pole}} &= 2.92433i \\ b_{22}^{\text{pole}} &= [-9.06127i + (5.11111i) L_{\mu m}^{\text{pole}}] \\ &\quad + [(5.76858 - 5.11111i) - 3.25383 L_{\mu m}^{\text{pole}}] L_V + 1.62692 L_V^2 \\ b_{32}^{\text{pole}} &= [(-16.2897 + 4.60874i) - (4.14291i) L_{\mu m}^{\text{pole}}] - (10.3704i) L_V \\ b_{13}^{\text{pole}} &= -1.42466 \\ b_{23}^{\text{pole}} &= [(-11.2099 - 12.9025i) + (7.13646i) L_{\mu m}^{\text{pole}}] - (7.13646i) L_V \\ b_{33}^{\text{pole}} &= [7.60697i - (20.0616i) L_{\mu m}^{\text{pole}} + (6.23652i) (L_{\mu m}^{\text{pole}})^2 + 1.32343 (L_{\mu m}^{\text{pole}})^3] \\ &\quad + [(1.68812 - 10.335i) + (12.7716 - 12.473i) L_{\mu m}^{\text{pole}} - 3.97029 (L_{\mu m}^{\text{pole}})^2] L_V \\ &\quad + [(3.28972 + 6.23652i) + 3.97029 L_{\mu m}^{\text{pole}}] L_V^2 - 1.32343 L_V^3 \end{aligned}$$

where $L_V = \log v$, $L_\nu = \log \nu$, and $L_{\mu m}^{\text{pole}} = \log \left(\frac{\mu}{m_{\text{pole}}} \right)$. The terms for the RGI cross section read as follows:

$$\begin{aligned}
c_{211}^{\text{pole}} &= (-10.3704i) L_V \\
c_{212}^{\text{pole}} &= (2.34213i) L_\nu^2 - (4.68426i) L_\nu L_V \\
c_{301}^{\text{pole}} &= (4.52707i) L_\nu \\
c_{302}^{\text{pole}} &= (-5.52388i) L_\nu^2 \\
c_{303}^{\text{pole}} &= (8.9869i) L_\nu^3 \\
c_{311}^{\text{pole}} &= (6.2963i) L_\nu \\
c_{312}^{\text{pole}} &= (-29.0134i) L_\nu^2 \\
c_{321}^{\text{pole}} &= \left[(-49.9713i) - (25.3076i) L_{\mu m}^{\text{pole}} \right] L_\nu.
\end{aligned} \tag{D.3}$$

In the MSRn mass scheme, the fixed-order coefficients are

$$\begin{aligned}
b_{10}^{\text{MSRn}} &= 2.i \\
b_{20}^{\text{MSRn}} &= 0 \\
b_{30}^{\text{MSRn}} &= 0.583333i \\
b_{11}^{\text{MSRn}} &= (4.18879i - 2.66667 L_V) - 0.848826i \left(\frac{R}{m_{\text{MSRn}} v} \right) \\
b_{21}^{\text{MSRn}} &= -3.39531i \\
b_{31}^{\text{MSRn}} &= \left[(0.586013 + 6.98132i) + 4.44444 L_{Rm} - 4.44444 L_V \right] + 0.530516i \left(\frac{R}{m_{\text{MSRn}} v} \right) \\
b_{12}^{\text{MSRn}} &= 2.92433i + 1.13177 \left(\frac{R}{m_{\text{MSRn}} v} \right) - 0.180127i \left(\frac{R}{m_{\text{MSRn}} v} \right)^2 \\
b_{22}^{\text{MSRn}} &= \left[-9.06127i + 5.11111i L_{\mu m}^{\text{MSRn}} + ((5.76858 - 5.11111i) - 3.25383 L_{\mu m}^{\text{MSRn}}) L_V + 1.62692 L_V^2 \right] \\
&\quad - \left[0.207077i + 1.03573i L_{\mu R} \right] \left(\frac{R}{m_{\text{MSRn}} v} \right) \\
b_{32}^{\text{MSRn}} &= \left[((-16.2897 + 4.60874i) - 4.14291i L_{\mu m}^{\text{MSRn}}) - 10.3704i L_V \right] \\
&\quad + \left[((0.822974 - 2.37037i) - 1.50902 L_{Rm}) + 1.50902 L_V \right] \left(\frac{R}{m_{\text{MSRn}} v} \right) \\
&\quad - (0.382769i) \left(\frac{R}{m_{\text{MSRn}} v} \right)^2 \\
b_{13}^{\text{MSRn}} &= -1.42466 + 1.24112i \left(\frac{R}{m_{\text{MSRn}} v} \right) + 0.480337 \left(\frac{R}{m_{\text{MSRn}} v} \right)^2 - 0.0764481i \left(\frac{R}{m_{\text{MSRn}} v} \right)^3 \\
b_{23}^{\text{MSRn}} &= \left[((-11.2099 - 12.9025i) + 7.13646i L_{\mu m}^{\text{MSRn}}) - 7.13646i L_V \right] \\
&\quad + \left[((-0.250811 + 2.16922i) + 2.76194 L_{\mu R} + 1.38097 L_{Rm}) - 1.38097 L_V \right] \left(\frac{R}{m_{\text{MSRn}} v} \right) \\
&\quad + \left[-0.393678i - 0.439576i L_{\mu R} \right] \left(\frac{R}{m_{\text{MSRn}} v} \right)^2
\end{aligned}$$

$$\begin{aligned}
b_{33}^{\text{MSRn}} = & \left[(7.60697i - 20.0616i L_{\mu m}^{\text{MSRn}} + 6.23652i (L_{\mu m}^{\text{MSRn}})^2) \right. \\
& + ((1.68812 - 10.335i) + (12.7716 - 12.473i) L_{\mu m}^{\text{MSRn}} - 3.97029 (L_{\mu m}^{\text{MSRn}})^2) L_V \\
& \left. + ((3.28972 + 6.23652i) + 3.97029 L_{\mu m}^{\text{MSRn}}) L_V^2 - 1.32343 L_V^3 \right] \\
& + \left[((6.91358 + 3.72745i) - 0.921032i L_{\mu R} - 1.26378i L_{\mu R}^2 + 1.75831i L_{Rm}) \right. \\
& \left. + 4.40132i L_V \right] \left(\frac{R}{m_{\text{MSRn}} v} \right) \\
& + 0.160112 \left(\frac{R}{m_{\text{MSRn}} v} \right)^2 - 0.0923748i \left(\frac{R}{m_{\text{MSRn}} v} \right)^3
\end{aligned}$$

where $L_{\mu m}^{\text{MSRn}} = \log \left(\frac{\mu}{m_{\text{MSRn}}} \right)$, $L_{\mu R} = \log \left(\frac{\mu}{R} \right)$, and $L_{Rm} = \log \left(\frac{R}{m_{\text{MSRn}}} \right)$. The RGI coefficients read

$$\begin{aligned}
c_{211}^{\text{MSRn}} &= (-10.3704i) L_V \\
c_{212}^{\text{MSRn}} &= (2.34213i) L_\nu^2 - (4.68426i) L_\nu L_V \\
c_{301}^{\text{MSRn}} &= (4.52707i) L_\nu \\
c_{302}^{\text{MSRn}} &= (-5.52388i) L_\nu^2 \\
c_{303}^{\text{MSRn}} &= (8.9869i) L_\nu^3 \\
c_{311}^{\text{MSRn}} &= (6.2963i) L_\nu - (5.76405i) L_\nu \left(\frac{R}{m_{\text{MSRn}} v} \right) \\
c_{312}^{\text{MSRn}} &= -(29.0134i) L_\nu^2 + (7.03322i) L_\nu^2 \left(\frac{R}{m_{\text{MSRn}} v} \right) \\
c_{321}^{\text{MSRn}} &= \left[-(49.9713i) L_\nu - (25.3076i) L_{Rm} L_\nu - (25.3076i) L_{\mu R} L_V \right] \\
& + \left[-(5.34446i) L_\nu - (4.33845i) L_V \right] \left(\frac{R}{m_{\text{MSRn}} v} \right) + (1.22317i) L_\nu \left(\frac{R}{m_{\text{MSRn}} v} \right)^2.
\end{aligned} \tag{D.4}$$

Bibliography

- [1] **Particle Data Group** Collaboration, C. Patrignani *et al.*, “Review of Particle Physics,” *Chin. Phys.* **C40** no. 10, (2016) 100001.
- [2] **Super-Kamiokande** Collaboration, Y. Fukuda *et al.*, “Evidence for oscillation of atmospheric neutrinos,” *Phys. Rev. Lett.* **81** (1998) 1562–1567, [arXiv:hep-ex/9807003 \[hep-ex\]](#).
- [3] H. Baer, T. Barklow, K. Fujii, Y. Gao, A. Hoang, S. Kanemura, J. List, H. E. Logan, A. Nomerotski, M. Perelstein, *et al.*, “The International Linear Collider Technical Design Report - Volume 2: Physics,” [arXiv:1306.6352 \[hep-ph\]](#).
- [4] L. Linssen, A. Miyamoto, M. Stanitzki, and H. Weerts, “Physics and Detectors at CLIC: CLIC Conceptual Design Report,” [arXiv:1202.5940 \[physics.ins-det\]](#).
- [5] K. Fujii *et al.*, “Physics Case for the International Linear Collider,” [arXiv:1506.05992 \[hep-ex\]](#).
- [6] **Gfitter Group** Collaboration, M. Baak, J. Cúth, J. Haller, A. Hoecker, R. Kogler, K. Mönig, M. Schott, and J. Stelzer, “The global electroweak fit at NNLO and prospects for the LHC and ILC,” *Eur. Phys. J.* **C74** (2014) 3046, [arXiv:1407.3792 \[hep-ph\]](#).
- [7] G. Degrandi, S. Di Vita, J. Elias-Miro, J. R. Espinosa, G. F. Giudice, G. Isidori, and A. Strumia, “Higgs mass and vacuum stability in the Standard Model at NNLO,” *JHEP* **08** (2012) 098, [arXiv:1205.6497 \[hep-ph\]](#).
- [8] M. Butenschoen, B. Dehnadi, A. H. Hoang, V. Mateu, M. Preisser, and I. W. Stewart, “Top Quark Mass Calibration for Monte Carlo Event Generators,” *Phys. Rev. Lett.* **117** no. 23, (2016) 232001, [arXiv:1608.01318 \[hep-ph\]](#).
- [9] F. Simon, “Impact of Theory Uncertainties on the Precision of the Top Quark Mass in a Threshold Scan at Future e^+e^- Colliders,” *PoS ICHEP2016* (2017) 872, [arXiv:1611.03399 \[hep-ex\]](#).
- [10] M. Vos *et al.*, “Top physics at high-energy lepton colliders,” [arXiv:1604.08122 \[hep-ex\]](#).
- [11] M. Stahlhofen and A. Hoang, “NNLL top-antitop production at threshold,” [arXiv:1111.4486 \[hep-ph\]](#). [PoSRADCOR2011,025(2011)].
- [12] M. Beneke, Y. Kiyo, P. Marquard, A. Penin, J. Piclum, and M. Steinhauser, “Next-to-Next-to-Next-to-Leading Order QCD Prediction for the Top Antitop S -Wave Pair Production Cross Section Near Threshold in e^+e^- Annihilation,” *Phys. Rev. Lett.* **115** no. 19, (2015) 192001, [arXiv:1506.06864 \[hep-ph\]](#).
- [13] F. Bach, B. C. Nejad, A. Hoang, W. Kilian, J. Reuter, M. Stahlhofen, T. Teubner, and C. Weiss, “Fully-differential Top-Pair Production at a Lepton Collider: From Threshold to Continuum,” [arXiv:1712.02220 \[hep-ph\]](#).

- [14] M. E. Peskin and D. V. Schroeder, *An Introduction to quantum field theory*. Addison-Wesley, Reading, USA, 1995.
<http://www.slac.stanford.edu/~mpeskin/QFT.html>.
- [15] M. D. Schwartz, *Quantum Field Theory and the Standard Model*. Cambridge University Press, 2014. <http://www.cambridge.org/us/academic/subjects/physics/theoretical-physics-and-mathematical-physics/quantum-field-theory-and-standard-model>.
- [16] D. J. Broadhurst, J. Fleischer, and O. V. Tarasov, “Two loop two point functions with masses: Asymptotic expansions and Taylor series, in any dimension,” *Z. Phys.* **C60** (1993) 287–302, [arXiv:hep-ph/9304303](#) [[hep-ph](#)].
- [17] A. O. G. Kallen and A. Sabry, “Fourth order vacuum polarization,” *Kong. Dan. Vid. Sel. Mat. Fys. Med.* **29** no. 17, (1955) 1–20. [[555\(1955\)](#)].
- [18] B. A. Kniehl, “Two Loop Corrections to the Vacuum Polarizations in Perturbative QCD,” *Nucl. Phys.* **B347** (1990) 86–104.
- [19] A. H. Hoang, V. Mateu, and S. Mohammad Zebarjad, “Heavy Quark Vacuum Polarization Function at $O(\alpha^2(s))$ $O(\alpha^3(s))$,” *Nucl. Phys.* **B813** (2009) 349–369, [arXiv:0807.4173](#) [[hep-ph](#)].
- [20] A. Maier and P. Marquard, “Life of Π ,” 2017. [arXiv:1710.03724](#) [[hep-ph](#)].
<http://inspirehep.net/record/1629587/files/arXiv:1710.03724.pdf>.
- [21] M. E. Luke, A. V. Manohar, and I. Z. Rothstein, “Renormalization group scaling in nonrelativistic QCD,” *Phys. Rev.* **D61** (2000) 074025, [arXiv:hep-ph/9910209](#) [[hep-ph](#)].
- [22] A. Pineda and J. Soto, “Effective field theory for ultrasoft momenta in NRQCD and NRQED,” *Nucl. Phys. Proc. Suppl.* **64** (1998) 428–432, [arXiv:hep-ph/9707481](#) [[hep-ph](#)].
- [23] M. Beneke and V. A. Smirnov, “Asymptotic expansion of Feynman integrals near threshold,” *Nucl. Phys.* **B522** (1998) 321–344, [arXiv:hep-ph/9711391](#) [[hep-ph](#)].
- [24] A. J. Buras, “Weak Hamiltonian, CP violation and rare decays,” in *Probing the standard model of particle interactions. Proceedings, Summer School in Theoretical Physics, NATO Advanced Study Institute, 68th session, Les Houches, France, July 28-September 5, 1997. Pt. 1, 2*, pp. 281–539. 1998. [arXiv:hep-ph/9806471](#) [[hep-ph](#)].
- [25] A. V. Manohar and M. B. Wise, “Heavy quark physics,” *Camb. Monogr. Part. Phys. Nucl. Phys. Cosmol.* **10** (2000) 1–191.
- [26] E. E. Salpeter and H. A. Bethe, “A Relativistic equation for bound state problems,” *Phys. Rev.* **84** (1951) 1232–1242.
- [27] J. S. Schwinger, “On the Green’s functions of quantized fields. 1.,” *Proc. Nat. Acad. Sci.* **37** (1951) 452–455.
- [28] W. E. Caswell and G. P. Lepage, “Effective Lagrangians for Bound State Problems in QED, QCD, and Other Field Theories,” *Phys. Lett.* **167B** (1986) 437–442.
- [29] G. T. Bodwin, E. Braaten, and G. P. Lepage, “Rigorous QCD analysis of inclusive annihilation and production of heavy quarkonium,” *Phys. Rev.* **D51** (1995) 1125–1171, [arXiv:hep-ph/9407339](#) [[hep-ph](#)]. [Erratum: *Phys. Rev.*D55,5853(1997)].
- [30] **Quarkonium Working Group** Collaboration, N. Brambilla *et al.*, “Heavy quarkonium physics,” [arXiv:hep-ph/0412158](#) [[hep-ph](#)].

- [31] N. Brambilla *et al.*, “Heavy quarkonium: progress, puzzles, and opportunities,” *Eur. Phys. J.* **C71** (2011) 1534, [arXiv:1010.5827 \[hep-ph\]](#).
- [32] M. Beneke and V. A. Smirnov, “Asymptotic expansion of Feynman integrals near threshold,” *Nucl. Phys.* **B522** (1998) 321–344, [arXiv:hep-ph/9711391 \[hep-ph\]](#).
- [33] P. Labelle, “Effective field theories for QED bound states: Extending nonrelativistic QED to study retardation effects,” *Phys. Rev.* **D58** (1998) 093013, [arXiv:hep-ph/9608491 \[hep-ph\]](#).
- [34] M. E. Luke and A. V. Manohar, “Bound states and power counting in effective field theories,” *Phys. Rev.* **D55** (1997) 4129–4140, [arXiv:hep-ph/9610534 \[hep-ph\]](#).
- [35] M. E. Luke and M. J. Savage, “Power counting in dimensionally regularized NRQCD,” *Phys. Rev.* **D57** (1998) 413–423, [arXiv:hep-ph/9707313 \[hep-ph\]](#).
- [36] B. Grinstein and I. Z. Rothstein, “Effective field theory and matching in nonrelativistic gauge theories,” *Phys. Rev.* **D57** (1998) 78–82, [arXiv:hep-ph/9703298 \[hep-ph\]](#).
- [37] A. V. Manohar and I. W. Stewart, “The QCD heavy quark potential to order v^{*2} : One loop matching conditions,” *Phys. Rev.* **D62** (2000) 074015, [arXiv:hep-ph/0003032 \[hep-ph\]](#).
- [38] A. V. Manohar and I. W. Stewart, “Renormalization group analysis of the QCD quark potential to order v^{*2} ,” *Phys. Rev.* **D62** (2000) 014033, [arXiv:hep-ph/9912226 \[hep-ph\]](#).
- [39] A. V. Manohar and I. W. Stewart, “Running of the heavy quark production current and $1/v$ potential in QCD,” *Phys. Rev.* **D63** (2001) 054004, [arXiv:hep-ph/0003107 \[hep-ph\]](#).
- [40] A. H. Hoang, A. V. Manohar, and I. W. Stewart, “The Running Coulomb potential and Lamb shift in QCD,” *Phys. Rev.* **D64** (2001) 014033, [arXiv:hep-ph/0102257 \[hep-ph\]](#).
- [41] A. H. Hoang, “Three loop anomalous dimension of the heavy quark pair production current in nonrelativistic QCD,” *Phys. Rev.* **D69** (2004) 034009, [arXiv:hep-ph/0307376 \[hep-ph\]](#).
- [42] A. H. Hoang and I. W. Stewart, “Ultrasoft renormalization in nonrelativistic QCD,” *Phys. Rev.* **D67** (2003) 114020, [arXiv:hep-ph/0209340 \[hep-ph\]](#).
- [43] A. H. Hoang and M. Stahlhofen, “Two-loop ultrasoft running of the $O(v^{*2})$ QCD quark potentials,” *Phys. Rev.* **D75** (2007) 054025, [arXiv:hep-ph/0611292 \[hep-ph\]](#).
- [44] M. Stahlhofen, *Ultrasoft renormalization of the potentials in v NRQCD*. PhD thesis, Munich, Tech. U., 2009. <http://nbn-resolving.de/urn/resolver.pl?urn:nbn:de:bvb:91-diss-20081230-680691-1-4>.
- [45] A. H. Hoang and M. Stahlhofen, “Ultrasoft NLL Running of the Nonrelativistic $O(v)$ QCD Quark Potential,” *JHEP* **06** (2011) 088, [arXiv:1102.0269 \[hep-ph\]](#).
- [46] A. H. Hoang, A. V. Manohar, I. W. Stewart, and T. Teubner, “A Renormalization group improved calculation of top quark production near threshold,” *Phys. Rev. Lett.* **86** (2001) 1951–1954, [arXiv:hep-ph/0011254 \[hep-ph\]](#).
- [47] A. H. Hoang, A. V. Manohar, I. W. Stewart, and T. Teubner, “The Threshold t anti- t cross-section at NNLL order,” *Phys. Rev.* **D65** (2002) 014014, [arXiv:hep-ph/0107144 \[hep-ph\]](#).
- [48] I. Z. Rothstein, “TASI lectures on effective field theories,” 2003. [arXiv:hep-ph/0308266 \[hep-ph\]](#).

- [49] A. H. Hoang, “Heavy quarkonium dynamics,” [arXiv:hep-ph/0204299](#) [hep-ph].
- [50] H. Georgi, “An Effective Field Theory for Heavy Quarks at Low-energies,” *Phys. Lett. B* **240** (1990) 447–450.
- [51] C. W. Bauer, S. Fleming, D. Pirjol, and I. W. Stewart, “An Effective field theory for collinear and soft gluons: Heavy to light decays,” *Phys. Rev. D* **63** (2001) 114020, [arXiv:hep-ph/0011336](#) [hep-ph].
- [52] I. W. Stewart, “Lectures on the Soft-Collinear Effective Theory,” 2013.
- [53] A. V. Manohar, “The HQET / NRQCD Lagrangian to order α / m^3 ,” *Phys. Rev. D* **56** (1997) 230–237, [arXiv:hep-ph/9701294](#) [hep-ph].
- [54] B. Grinstein, “A Modern introduction to quarkonium theory,” *Int. J. Mod. Phys. A* **15** (2000) 461–496, [arXiv:hep-ph/9811264](#) [hep-ph].
- [55] L. S. Brown and W. I. Weisberger, “Remarks on the Static Potential in Quantum Chromodynamics,” *Phys. Rev. D* **20** (1979) 3239.
- [56] A. Hoang, P. Ruiz-Femenia, and M. Stahlhofen, “Renormalization Group Improved Bottom Mass from Upsilon Sum Rules at NNLL Order,” *JHEP* **10** (2012) 188, [arXiv:1209.0450](#) [hep-ph].
- [57] A. H. Hoang and M. Stahlhofen, “The Top-Antitop Threshold at the ILC: NNLL QCD Uncertainties,” *JHEP* **05** (2014) 121, [arXiv:1309.6323](#) [hep-ph].
- [58] M. Peter, “The Static quark - anti-quark potential in QCD to three loops,” *Phys. Rev. Lett.* **78** (1997) 602–605, [arXiv:hep-ph/9610209](#) [hep-ph].
- [59] Y. Schroder, “The Static potential in QCD to two loops,” *Phys. Lett. B* **447** (1999) 321–326, [arXiv:hep-ph/9812205](#) [hep-ph].
- [60] E. H. Wichmann and C. Woo, “Integral Representation for the Nonrelativistic Coulomb Green’s Function,” *Journal of Mathematical Physics* **2** no. 2, (1961) 178–180. <https://doi.org/10.1063/1.1703696>.
- [61] J. Schwinger, “Coulomb Green’s Function,” *J. Math. Phys.* **5** (1964) 1606–1608.
- [62] L. Hostler, “Coulomb green’s functions and the furry approximation,” *Journal of Mathematical Physics* **5** no. 5, (1964) 591–611.
- [63] A. H. Hoang and T. Teubner, “Top quark pair production close to threshold: Top mass, width and momentum distribution,” *Phys. Rev. D* **60** (1999) 114027, [arXiv:hep-ph/9904468](#) [hep-ph].
- [64] V. S. Fadin and V. A. Khoze, “Threshold Behavior of Heavy Top Production in $e^+ e^-$ Collisions,” *JETP Lett.* **46** (1987) 525–529. [Pisma Zh. Eksp. Teor. Fiz.46,417(1987)].
- [65] M. B. Voloshin, “On Dynamics of Heavy Quarks in Nonperturbative QCD Vacuum,” *Nucl. Phys. B* **154** (1979) 365–380.
- [66] H. Leutwyler, “How to Use Heavy Quarks to Probe the QCD Vacuum,” *Phys. Lett.* **98B** (1981) 447–450.
- [67] V. S. Fadin and O. I. Yakovlev, “Nonperturbative correction to the cross-section of t anti- t quark pair production near threshold,” *Sov. J. Nucl. Phys.* **53** (1991) 688–691. [Yad. Fiz.53,1111(1991)].
- [68] M. Beneke, “Top quark production near threshold,” *Nucl. Phys. Proc. Suppl.* **86** (2000) 547–554, [arXiv:hep-ph/9910534](#) [hep-ph].

- [69] A. H. Hoang and C. J. Reisser, “Electroweak absorptive parts in NRQCD matching conditions,” *Phys. Rev.* **D71** (2005) 074022, [arXiv:hep-ph/0412258 \[hep-ph\]](#).
- [70] A. H. Hoang, C. J. Reisser, and P. Ruiz-Femenia, “Phase Space Matching and Finite Lifetime Effects for Top-Pair Production Close to Threshold,” *Phys. Rev.* **D82** (2010) 014005, [arXiv:1002.3223 \[hep-ph\]](#).
- [71] M. Beneke, B. Jantzen, and P. Ruiz-Femenia, “Electroweak non-resonant NLO corrections to $e^+e^- \rightarrow W^+W^-b\bar{b}$ in the $t\bar{t}$ resonance region,” *Nucl. Phys.* **B840** (2010) 186–213, [arXiv:1004.2188 \[hep-ph\]](#).
- [72] A. H. Hoang and C. J. Reisser, “On electroweak matching conditions for top pair production at threshold,” *Phys. Rev.* **D74** (2006) 034002, [arXiv:hep-ph/0604104 \[hep-ph\]](#).
- [73] M. Beneke, A. Maier, T. Rauh, and P. Ruiz-Femenia, “Non-resonant and electroweak NNLO correction to the e^+e^- top anti-top threshold,” [arXiv:1711.10429 \[hep-ph\]](#).
- [74] M. Beneke and V. M. Braun, “Heavy quark effective theory beyond perturbation theory: Renormalons, the pole mass and the residual mass term,” *Nucl. Phys.* **B426** (1994) 301–343, [arXiv:hep-ph/9402364 \[hep-ph\]](#).
- [75] I. I. Y. Bigi, M. A. Shifman, N. G. Uraltsev, and A. I. Vainshtein, “The Pole mass of the heavy quark. Perturbation theory and beyond,” *Phys. Rev.* **D50** (1994) 2234–2246, [arXiv:hep-ph/9402360 \[hep-ph\]](#).
- [76] A. H. Hoang, Z. Ligeti, and A. V. Manohar, “B decay and the Upsilon mass,” *Phys. Rev. Lett.* **82** (1999) 277–280, [arXiv:hep-ph/9809423 \[hep-ph\]](#).
- [77] A. H. Hoang, Z. Ligeti, and A. V. Manohar, “B decays in the upsilon expansion,” *Phys. Rev.* **D59** (1999) 074017, [arXiv:hep-ph/9811239 \[hep-ph\]](#).
- [78] M. Beneke, “A Quark mass definition adequate for threshold problems,” *Phys. Lett.* **B434** (1998) 115–125, [arXiv:hep-ph/9804241 \[hep-ph\]](#).
- [79] A. Czarnecki, K. Melnikov, and N. Uraltsev, “NonAbelian dipole radiation and the heavy quark expansion,” *Phys. Rev. Lett.* **80** (1998) 3189–3192, [arXiv:hep-ph/9708372 \[hep-ph\]](#).
- [80] M. Beneke, “Renormalons,” *Phys. Rept.* **317** (1999) 1–142, [arXiv:hep-ph/9807443 \[hep-ph\]](#).
- [81] R. Tarrach, “The Pole Mass in Perturbative QCD,” *Nucl. Phys.* **B183** (1981) 384–396.
- [82] N. Gray, D. J. Broadhurst, W. Grafe, and K. Schilcher, “Three Loop Relation of Quark (Modified) M_s and Pole Masses,” *Z. Phys.* **C48** (1990) 673–680.
- [83] K. G. Chetyrkin and M. Steinhauser, “Short distance mass of a heavy quark at order α_s^3 ,” *Phys. Rev. Lett.* **83** (1999) 4001–4004, [arXiv:hep-ph/9907509 \[hep-ph\]](#).
- [84] K. G. Chetyrkin and M. Steinhauser, “The Relation between the \overline{MS} -bar and the on-shell quark mass at order α_s^3 ,” *Nucl. Phys.* **B573** (2000) 617–651, [arXiv:hep-ph/9911434 \[hep-ph\]](#).
- [85] K. Melnikov and T. v. Ritbergen, “The Three loop relation between the \overline{MS} -bar and the pole quark masses,” *Phys. Lett.* **B482** (2000) 99–108, [arXiv:hep-ph/9912391 \[hep-ph\]](#).
- [86] P. Marquard, L. Mihaila, J. H. Piclum, and M. Steinhauser, “Relation between the pole and the minimally subtracted mass in dimensional regularization and dimensional reduction to three-loop order,” *Nucl. Phys.* **B773** (2007) 1–18, [arXiv:hep-ph/0702185 \[hep-ph\]](#).

- [87] P. Marquard, A. V. Smirnov, V. A. Smirnov, and M. Steinhauser, “Quark Mass Relations to Four-Loop Order in Perturbative QCD,” *Phys. Rev. Lett.* **114** no. 14, (2015) 142002, [arXiv:1502.01030 \[hep-ph\]](#).
- [88] P. Marquard, A. V. Smirnov, V. A. Smirnov, M. Steinhauser, and D. Wellmann, “ $\overline{\text{MS}}$ -on-shell quark mass relation up to four loops in QCD and a general $\text{SU}(N)$ gauge group,” *Phys. Rev.* **D94** no. 7, (2016) 074025, [arXiv:1606.06754 \[hep-ph\]](#).
- [89] A. H. Hoang, A. Jain, C. Lepenik, V. Mateu, M. Preisser, I. Scimemi, and I. W. Stewart, “The MSR Mass and the $\mathcal{O}(\Lambda_{\text{QCD}})$ Renormalon Sum Rule,” [arXiv:1704.01580 \[hep-ph\]](#).
- [90] A. H. Hoang, A. Jain, I. Scimemi, and I. W. Stewart, “Infrared Renormalization Group Flow for Heavy Quark Masses,” *Phys. Rev. Lett.* **101** (2008) 151602, [arXiv:0803.4214 \[hep-ph\]](#).
- [91] A. H. Hoang, A. Jain, I. Scimemi, and I. W. Stewart, “R-evolution: Improving perturbative QCD,” *Phys. Rev.* **D82** (2010) 011501, [arXiv:0908.3189 \[hep-ph\]](#).
- [92] A. H. Hoang, “The Top Mass: Interpretation and Theoretical Uncertainties,” in *Proceedings, 7th International Workshop on Top Quark Physics (TOP2014): Cannes, France, September 28-October 3, 2014*. 2014. [arXiv:1412.3649 \[hep-ph\]](#).
<http://inspirehep.net/record/1333866/files/arXiv:1412.3649.pdf>.
- [93] R. E. Cutkosky, “Singularities and discontinuities of Feynman amplitudes,” *J. Math. Phys.* **1** (1960) 429–433.
- [94] M. J. G. Veltman, “Diagrammatica: The Path to Feynman rules,” *Cambridge Lect. Notes Phys.* **4** (1994) 1–284.
- [95] V. A. Smirnov, “Applied asymptotic expansions in momenta and masses,” *Springer Tracts Mod. Phys.* **177** (2002) 1–262.
- [96] B. Jantzen, “Foundation and generalization of the expansion by regions,” *JHEP* **12** (2011) 076, [arXiv:1111.2589 \[hep-ph\]](#).
- [97] V. A. Smirnov, “Renormalization and asymptotic expansions,” *Prog. Phys.(Birkhauser)* **14** (1991) 1–380.
- [98] F. V. Tkachov, “A Theorem on Analytical Calculability of Four Loop Renormalization Group Functions,” *Phys. Lett.* **100B** (1981) 65–68.
- [99] K. G. Chetyrkin and F. V. Tkachov, “Integration by Parts: The Algorithm to Calculate beta Functions in 4 Loops,” *Nucl. Phys.* **B192** (1981) 159–204.
- [100] P. A. Baikov, K. G. Chetyrkin, and J. H. Kühn, “Five-Loop Running of the QCD coupling constant,” *Phys. Rev. Lett.* **118** no. 8, (2017) 082002, [arXiv:1606.08659 \[hep-ph\]](#).
- [101] K. G. Chetyrkin, J. H. Kuhn, and M. Steinhauser, “RunDec: A Mathematica package for running and decoupling of the strong coupling and quark masses,” *Comput. Phys. Commun.* **133** (2000) 43–65, [arXiv:hep-ph/0004189 \[hep-ph\]](#).
- [102] F. Herren and M. Steinhauser, “Version 3 of RunDec and CRunDec,” *Comput. Phys. Commun.* **224** (2018) 333–345, [arXiv:1703.03751 \[hep-ph\]](#).

Acknowledgements

First, I would like to express my gratitude to my supervisor André Hoang for his time, patience, and guidance. He gave me an exciting topic to work on, had an open door if I had questions and guided me through my first presentations at conferences.

I also want to thank all members of the particle physics group for the positive and stimulating atmosphere. Thank you Elke Aeikens, Manuel Fink, Michael Lanschützer, Daniel Lechner, Christopher Lepenik, Maximilian Löschner, Aditya Pathak, Moritz Preißer, Daniel Samitz, Carla Schuler, and Gabriel Sommer for many interesting and helpful discussions about physics and all non-physics conversations and many laughs during lunch breaks.

I am grateful to my parents for supporting me during my studies, to my father for encouraging me to always ask one more question, and to my sister Lena for advice on presentations and scientific writing.

Lastly, I want to thank my boyfriend Felix Lübke for all his love and support, and for cheering me up when work was progressing slowly.